Design and Fabrication of Neuromorphic Devices towards Emulating Artificial Intelligence

A Thesis
Submitted for the Degree of

Doctor of Philosophy

By

Bharath B

JNCASR

Chemistry and Physics of Materials Unit
Jawaharlal Nehru Centre for Advanced Scientific Research
(An Institution Deemed-to-be-University)
Bengaluru-560064 (India)

November 2020

Dedicated to Almighty
and
My Family

Declaration

I hereby declare that the thesis entitled **"Design and Fabrication of Neuromorphic Devices towards Emulating Artificial Intelligence**" is an authentic record of research work carried out by me at the Chemistry and Physics of Materials Unit, Jawaharlal Nehru Centre for Advanced Scientific Research, Bengaluru, India under the supervision of Prof. Giridhar U. Kulkarni and that it has not been submitted elsewhere for the award of any degree or diploma.

In keeping with the general practice in reporting scientific observations, due acknowledgment has been made whenever the work described is based on the findings of other investigators. Any omission that might have occurred due to oversight or error in judgment is regretted.

Bharath. B

Bharath B

Certificate

Certified that the work described in this thesis titled "**Design and Fabrication of Neuromorphic Devices towards Emulating Artificial Intelligence**" has been carried out by Bharath B at the Chemistry and Physics of Materials Unit, Jawaharlal Nehru Centre for Advanced Scientific Research, Bengaluru, India, under my supervision and that it has not been submitted elsewhere for the award of any degree or diploma.

Professor Giridhar U. Kulkarni
(Research Supervisor)

Acknowledgments

First and foremost, I would like to thank my research supervisor ***Professor Giridhar U. Kulkarni,*** for his constant guidance throughout this research journey. I am very grateful to him for introducing me to the research field, suggesting very interesting ideas, and thus encouraging and motivating me towards new explorations. His keen eye for the subtle aspects of approaching an experiment or analyzing the data has inspired me to achieve such confidence in designing and performing research. I always admire his working style; to thoughtfully decide a scientific problem and pursue and dissect it meaningfully. His passion for research always motivates me. The forum he created for research discussions is highly appreciable. I express my deep sense of gratitude and a profound feeling of admiration for him.

Prof. C. N. R. Rao, a constant source of inspiration and it is always a great opportunity to listen to encouraging words about research by the legend. I learned more about him through my research supervisor, who himself is a great disciple of Prof. Rao.

I thank past and present ***Presidents of JNCASR*** for their immense support in various activities. It is my pleasure to thank the past and present ***Chairmen of CPMU*** for allowing me to use department instrumentation facilities.

I thank all ***my collaborators***; Prof. C. N. R. Rao, Dr. M. B. Sreedhara, Dr. Murali G, Dr. K. D. M. Rao, Dr. K. N. Harish, Dr. Sunil W, Dr. Umesha M for their fruitful discussion and active collaboration.

I thank all the faculty members of CPMU, NCU and TSU for their cordiality, especially my teachers, Prof. A. Sundaresan, Prof. Umesh V. Waghmare, Prof. S. M. Shivaprasad, Prof. Kanishka Biswas, Prof. Sebastian C. Peter, Prof. Giridhar U. Kulkarni and Prof. Abha Misra (IISc) for their courses.

Timely and ready assistance and also friendly attitude from technical staff is greatly acknowledged. I thank Mr. Srinivas, Mr. Srinath, Mrs. Selvi (FESEM), Mr. Alla Srinivasarao, Mr. Sanjit, Dr. Basavaraja and Ms. Meenakshi for their invaluable technical assistance. Special thanks to Mr. Sunil, Mrs. Vanitha, Ms. Reetu and Ms. Lalitha for their assistance in various activities.

I am grateful to ***my past and present lab mates***; Dr. Abhay, Dr. Mallik, Dr. Gangaiah, Dr. Kiruthika, Dr. Umesha, Dr. Sunil, Dr. Ankush, Mr. Rajashekhar, Mr. Karthikeya, Ms. Guratinder, Ms. Chaitali, Mr. Indrajit, Mr. Suman, Dr. Shubra, Dr. Murali, Dr. Dipanwita, Dr. Ashutosh, Mr. Mukesh, Mr. Rahul, Mr. Bhupesh, Ms. Ramya, Ms. Amala, Dr. Shobin, Dr. Harish, Dr. Remya, Dr. Rithesh, Dr. Gurumurthy, Mr. Aman, Ms. Janani, Mr. Kaushik, Ms. Suchithra, Ms. Nikita, Dr. Shridhar, Mr. Sankalp and Mr. Rohit.

I sincerely thank Dr. Abhay A. Sagade, for fruitful scientific discussions and support.

A special note of thanks goes to, Ms. Divya C and Ms. Shanola, for proofreading the thesis.

I thank the staff of the academic and administrative section in JNCASR for their assistance. I would like to thank the library, computer lab, Dhanvantri and hostel staff for their cooperation and help.

I thank JNCASR and TPF for residential, financial assistance and DST for providing facilities.

I thank all my 2014 batch mates.

I thank all my friends in and out of JNCASR for their wonderful friendship and unconditional love and affection. Special thanks to Ms. Pavitra for the help, support and joyful moments.

I thank all my teachers, especially Dr. A. P. Radhakrishna, for motivating me to pursue research.

Besides research life, Prof. G. U. Kulkarni and his family’s personal care and affection are greatly acknowledged for providing me a home away from home. I thank Mrs. Indira Kulkarni, Teju and Poorna for their warmth and hospitality.

I would like to thank my parents, siblings for their continuous and consistent support and encouragement; otherwise I could not have come thus far.

I thank the Almighty for his blessings.

Preface

The thesis work pertains to the design and fabrication of neuromorphic devices towards mimicking human-like memory and behavioral patterns. It is organized into six chapters. **Chapter I** introduces the concept of neuromorphic devices and their various types. In its latter part, the scope of the thesis work is presented. **Chapter II** introduces characterization techniques used for the work.

Chapter III deals with the fabrication of an inorganic artificial synaptic network (ASN) via a simple self-forming technique and emulation of human-like behavioral patterns by applying carefully designed electrical pulse signals. This chapter contains three sections. Chapter IIIA describes the fabrication and characterization details. A continuous Ag film is dewetted by thermal treatment in ambient atmosphere to form disconnected islands having branches, nanogaps and nanoparticles, thus resembling the biological neural network. With voltage pulse signals, basic synaptic behaviors such as short-term plasticity (STP), long-term plasticity (LTP), and spike parameter-dependent plasticities are emulated. Chapter IIIB deals with the emulation of higher-order learning behaviors in the fabricated neuromorphic device by applying the custom-designed pulse configuration. Behaviors such as associative learning, interest-based learning, and behavior under supervision are demonstrated. Chapter IIIC portrays an interesting study of mimicking neural damage in the ASN device. The device is damaged by applying colossal electrical signals and physical scratches to mimic the real scenario, and under such damage, the device behavior is studied.

Chapter IV describes the fabrication of metal-organic based flexible neuromorphic devices. A simple solution-based technique is used to fabricate metal nanoparticles in the carbon matrix by thermolysis of Pd hexadecanthiolate. Resistive and neuromorphic device behavior is observed by fabricating the device at different temperatures. A flexible device is fabricated on a Kapton tape and excellent bending stability is demonstrated. More importantly, the device shows synaptic behaviors in the bent state.

Chapter V explains the fabrication of optoelectronic devices towards emulating memory and artificial visual system. This chapter contains three sections. Chapter VA covers the fabrication of the Au-Si device using an electroless deposition technique. I-V measurement shows the presence of trap states and is explored to mimic basic synaptic behaviors (STP, LTP) and also the famous Ebbinghaus forgetting curve. Chapter VB elucidates the fabrication of a Au-Si photodetector. The electroless deposition process is optimized to accomplish large area, high-performing photodetector. Chapter VC describes the emulation of a primitive artificial visual system using the fabricated Au-Si photodetector (representing the eye) and the Ag-ASN neuromorphic device (representing the brain). Optical pulse signals are converted to voltage signals by the photodetector and are processed by the ASN device.

In **Chapter VI**, a summary of the thesis work and an outlook are provided.

Table of contents

Acronyms

AFM	Atomic Force Microscopy
Ag	Silver
ANN	Artificial Neural Network
ASN	Artificial Synaptic Network
Au	Gold
CAFM	Conducting AFM
CMOS	Complementary Metal Oxide Semiconductor
ECM	Electro Chemical Metallization
EPSC	Excitatory Post Synaptic Current
FESEM	Field Emission Scanning Electron Microscope
HAADF	High-Angle Annular Dark Field
HRS	High Resistance State
HRTEM	High Resolution Transmission Electron Microscopy
IPSC	Inhibitory Post Synaptic Current
IR	Infrared
LED	Light Emitting Diode
LRS	Low Resistance State
LTM	Long-Term Memory
LTP	Long-Term Plasticity
NIR	Near Infrared
NVM	Non-Volatile Memory
PCM	Phase Change Memory
Pd	Palladium
SDDP	Spike-Duration Dependent Plasticity
SEM	Scanning Electron Microscopy
SFDP	Spike-Frequency Dependent Plasticity

Si	Silicon
SiO_2	Silicon dioxide
SM	Sensory Memory
SNDP	Spike-Number Dependent Plasticity
SPDP	Spike-Parameter Dependent Plasticity
STEM	Scanning Transmission Electron Microscopy
STM	Short-Term Memory
STP	Short-Term Plasticity
TCR	Temperature Coefficient of Resistance
TMD	Transition Metal Dichalcogenides
UV	Ultraviolet
VCM	Valence Change Memory
XPS	X-ray Photoelectron Spectroscopy
XRD	X-ray Diffraction

Chapter I

Introduction

I.A Artificial Intelligence

Artificial Intelligence (AI) aims to simulate human intelligence in machines so that they can think like humans, and perform human-like cognition [1]. Although the present-day supercomputers can perform excellent calculations, they are very slow and inefficient compared to the human brain! [2,3] For example, a supercomputer takes around 500 s to emulate 5 s of human brain activity by consuming ~ MWs of energy [4]. This is much due to the conventional von Neumann computer architecture, where the memory and processing units are physically separate and are connected by limited interconnects known as bus bars [5,6]. During processing, data shuttles between these units, which makes the process slow and inefficient. Besides, limited transistor density in a processor chip also influences the computational ability. Although the advancing lithography technique is endeavoring to miniaturize transistors to the lowest dimension possible [7] to create a high density on board, the computational performance is still under satisfying. As the transistor scaling down approaches the theoretical limit, their packing density in a chip may not hold the famous Moore's law any further [8].

While the human brain is believed to process information by parallel computing, this is possible due to the massive neurons (~ 10^{11}) in the human brain interconnected in a complex manner to form synapses [9]. These enormous interconnections (~ 10^{15} synaptic junctions) lead to excellent cognitive abilities (synaptic activities) such as thinking, learning from experience, abstract ideas, efficient memory management (sensory memory – SM, short-term memory/plasticity – STM/P, long term memory/plasticity – LTM/P), complex associative learning and others [10]. Astonishingly, these complex processes take only 20% of total body energy (~ 20 W) [11]. This is the reason that AI aims to mimic real intelligence or the human brain.

Inspired by this massive synapse density, efforts are increasing from industry to fabricate high-density transistor interconnections on the processor chip [12]. Such neuromorphic chips have been developed and some of them include IBM's *TrueNorth*, APT's *SpiNNaker*, Intel's *Loihi* [13–15]. Although their performance is better than conventional processors, they are not even close to the human brain efficiency. There are several other approaches such as software-based and hardware-based techniques proposed to efficiently accomplish AI in the recent past (Figure I.1).

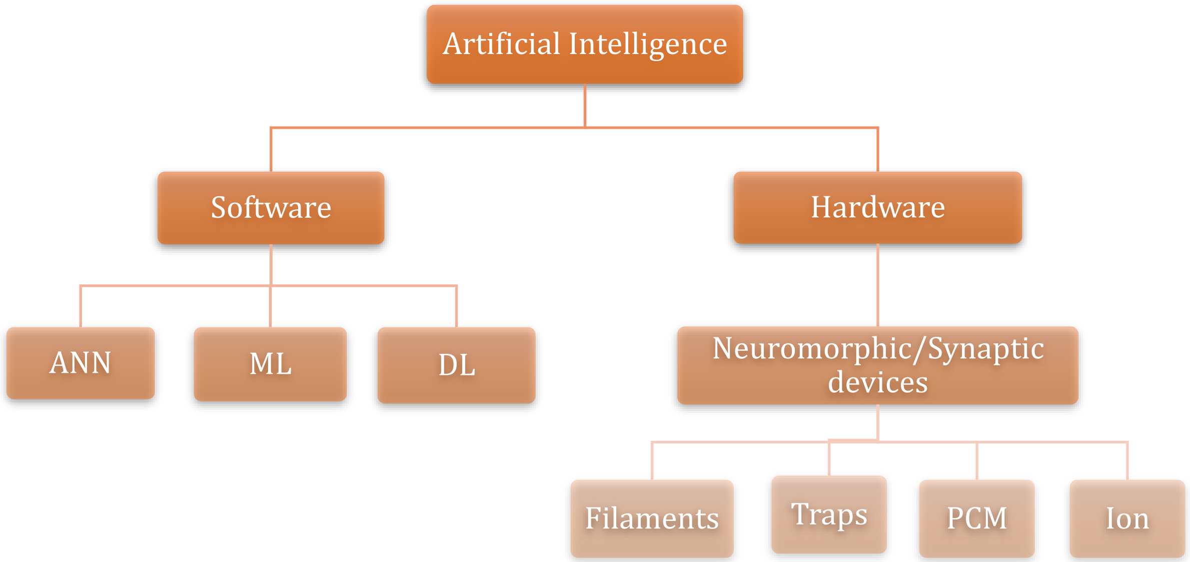

Figure I.1: Schematic illustration of AI platforms.

Software-based platform

Currently, software-based platforms are well established to perform AI [16]. Here, complex, intelligent algorithms are embedded in the conventional computing platform to perform specific tasks. These algorithms are able to learn from experience/training like humans. They have shown considerable success in performance and they do blend with our day to day activities. Some common examples are Alexa, Siri, Google Assistant, AlphaGo, AlphaZero, etc. [17–19] These are realized with the help of programming algorithms such as artificial neural network (ANN), machine learning (ML), deep learning (DL) etc. [15] Although these methods are successfully implemented, they are inefficient in terms of speed, space and energy consumption. For example, the gaming algorithm, AlphaGo has defeated a human player in the Go game by consuming ~ MWs of energy to play a single game with enormous space for a computer platform [20]. And, these algorithms require enormous training data sets to learn and perform efficiently.

Neuromorphic computing

Recently, NVMs/memristors combined with software platforms (ANNs) have been promising to show enhancement in the performance of brain-inspired computing known as neuromorphic computing [21–23]. Taking advantage of their tunable and history-dependent conductance states, several features such as pattern and image recognition, handwritten digit recognition, etc., have been demonstrated [24–27]. However, they again rely on software platforms, thus making it inefficient. Besides, they do not show temporal dynamics in the conductance state which is essential for emulating STM, LTM and other synaptic activities required for emulating efficient AI [28].

I.B Neuromorphic/synaptic devices

Neuromorphic or synaptic devices are the one which emulate the synaptic activities by mimicking the biological synapse without the aid of software platforms or CMOS supporting circuits. In the human brain, synapses are the junctions where two neurons meet (Figure I.2a,b) [29]. The presence of massive synaptic junctions is believed to give rise to superior cognitive abilities [30]. A synapse consists of pre- and post-neurons separated by a gap (~ 20 nm) called the synaptic cleft (Figure I.2b). Information is received from the external world through sensory systems present in the body and sent to the brain as an action potential (neuronal voltage spikes). This action potential travels through the neuron. When it reaches the synapse, neurotransmitters (Ca^{2+}, Na^{+}, K^{+} ions) present in the pre-synaptic neuron get released into the synaptic cleft and are collected by the receptors present in the post-synaptic neuron, thus passing the information in the neural network [30]. During this, the current in the synaptic junction changes (EPSC/IPSC), thereby changing the channel conductance, known as neuroplasticity (Figure I.2c) [31,32]. This neuroplasticity is believed to be responsible for memory formation [33]. Neuroplasticity or synaptic weight can be modulated based on the input spiking condition, leading to different types of memories such as SM, STM and LTM (Figure I.3a). As a common example, brain generally tends to forget an OTP (one-time password) due to low rehearsal (STM, typically lasting ~ tens of seconds), while can retain a mobile number for longer times (LTM, typically retained for a period of minutes to years) due to large rehearsal. Along with rehearsal (number of spikes), other

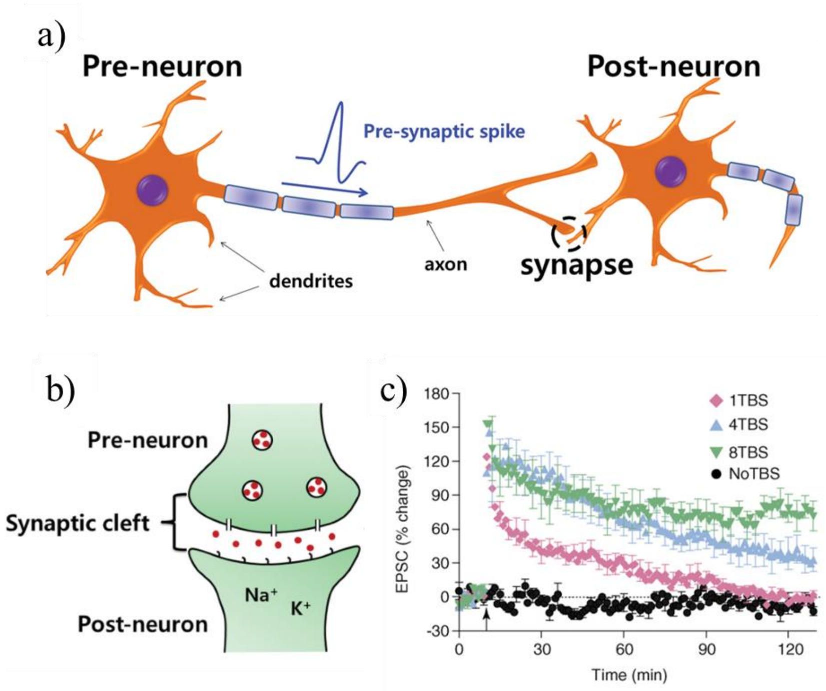

Figure I.2: a) Schematic showing the neuron interconnection. b) Two neurons meet at a junction called the synapse. Action potential stimulates the neurotransmitters to get released into the synaptic cleft. Figure adapted with permission from Reference 29; copyright 2016 John Wiley and Sons. c) Typical excitatory post-synaptic current (EPSC) of a rat neuron. Figure adapted with permission from Reference 30; copyright 2007 Elsevier.

spike parameters such as how frequent the information is revised (spike frequency), duration of a learning event (spike width/duration) and the temporal difference between the pre- and post-synaptic signals (spike timing, Hebbian learning) also modulate the synaptic plasticity (Figure I.3b,c) [34].

In neuromorphic devices, the device conductance/current is assigned to the synaptic behavior and the stimulating pulses (voltage/light) represent the learning signal (action potential). The conductance of the device can be tuned by various mechanisms such as conducting filament bridging, carrier trapping and detrapping, phase change in materials, ion migration [35], etc. Although memristors and neuromorphic/synaptic devices have different features [28], the terminology is interchangeably used in literature.

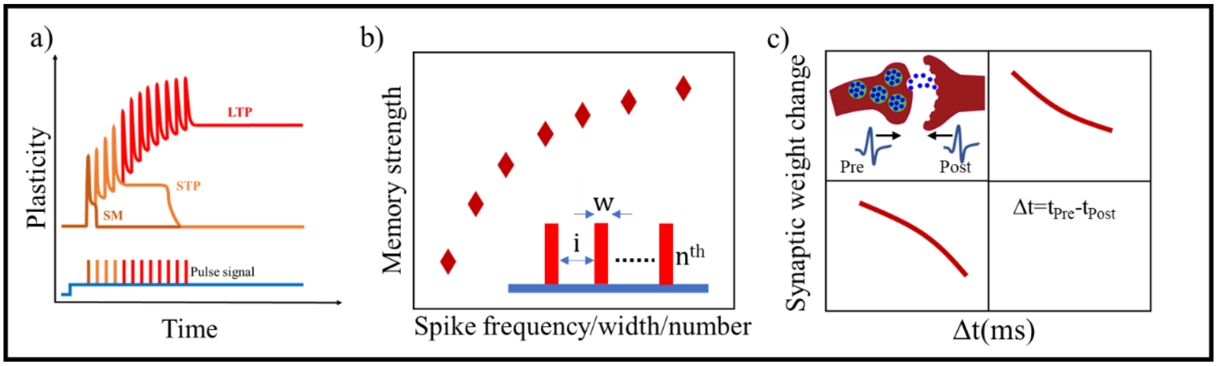

Figure I.3: Schematic showing the basic synaptic activities such as a) sensory memory (SM), short-term memory (STP), long-term memory (LTP) b) spike parameter dependent plasticity (SPDP) c) spike timing dependent plasticity (STDP).

Filamentary bridges

Electrochemical metallization memory (ECM): ECM devices rely on the electrochemical dissolution of an active electrode to form metal ions and their deposition on an inert electrode to form filaments [36,37]. A typical ECM device consists of metal-ion conductor-metal (MIM) architecture [38,39]. The basic switching mechanism involves anodic oxidization ($M \rightarrow M^+ + e$) of a reactive metal electrode (Ag, Cu, Ni, etc.) in response to an applied potential, M^+ migration in the presence of the electric field, and cathodic reduction ($M^+ + e \rightarrow M$) of the metal ions at the inert electrode (Pt, W, etc.) thus forming filaments [37,40]. Ag/Ag_2S cell is a frequently explored device, as shown in Figure I.4b [41]. With the application of electrical signals, Ag electrodes dissolve to form Ag^+ ions. These ions migrate through the Ag_2S electrolyte to the inert electrode in the presence of an electric field and thus get reduced to form filaments (Figure I.4a). The typical switching nature of the device is shown in Figure I.4c. By applying increased number of voltage pulse signals, STP to LTP transition is demonstrated (Figure I.4d,e).

Valence change memory (VCM): In a typical VCM device architecture, an insulator/dielectric is sandwiched between two metal electrodes (MIM) which need not be reactive [42,43]. The device typically has a low conducting state due to the insulating channel. When the electric field is applied, the interface barrier height is lowered due to the migration of oxygen vacancies, leading to the formation of conducting filaments that bridge the two electrodes thereby switching the device to a high conducting state. Often, precise stoichiometric control

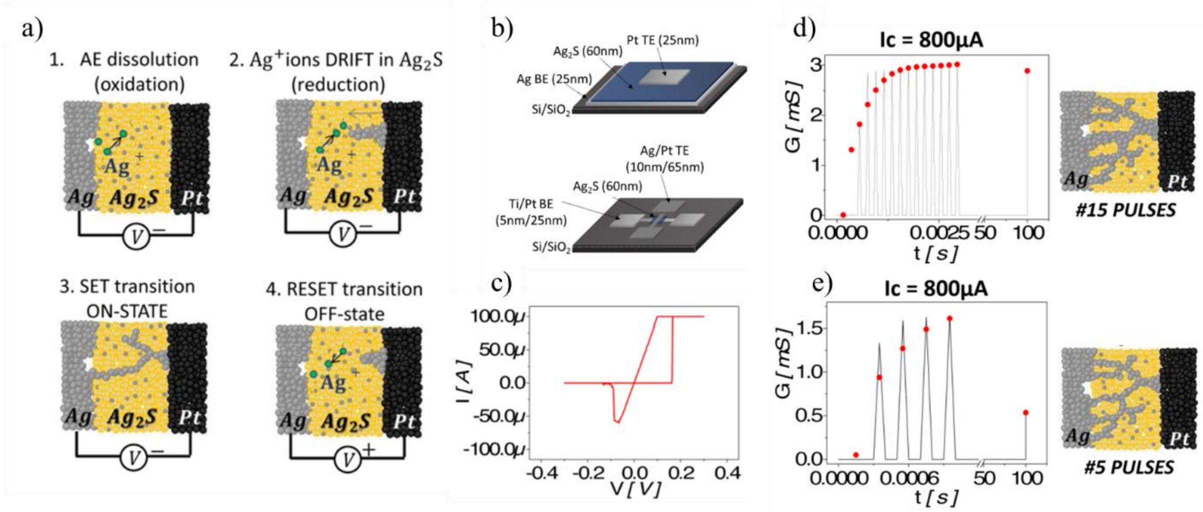

Figure I.4: a) Schematic ECM cell. When an electric field is applied, the Ag electrode dissolves and the ions drift towards the inert electrode and get reduced to form conduction filaments. b) schematic of the device. c) Typical I-V characteristics showing the switching behavior. d) LTP is emulated by applying 15 electrical pulses. e) STP is emulated with 5 electrical pulses. Figure adapted with permission from Reference 41; copyright 2015 American Chemical Society.

of the active material is important for such devices. A wide range of oxide materials have been explored towards the development of neuromorphic devices. Lu et al., reported emulation of STP and LTP in a Pd/WO_x/W device (Figure I.5a) [44]. Here, a Tungsten bottom electrode was first fabricated using e-beam lithography and then it was rapidly thermal annealed at 400 °C for the formation of WO_x, followed by coating a top Pd electrode. Synaptic activity was demonstrated with five electrical pulse signals of an amplitude of 1.3 V and a width of 1.3 ms applied at different spike intervals (Figure I.5b). For a longer pulse interval, the filaments relax back quickly showing STP, while for a shorter pulse interval, the stable filaments formed give rise to LTP (Figure I.5c,d).

In these types of devices, the dimensions of the filaments play a major role in deciding their stability, thereby leading to the emulation of STP and LTP [41]. Thinner filaments (diameter in ~ few nm) will have a lower volume energy than their surface energy, thus dissolving quickly, resulting in an STP behavior. Meanwhile, thicker filaments (diameter ~ few tens of nm) will have a higher volume energy than their surface energy, thus remaining stable for a long time leading to LTP behavior. The dimension of filaments can be controlled by controlling the number of pulses or current compliance. Increasing pulse number or current compliance increases the ion density in the channel thereby favoring the formation of thick filaments.

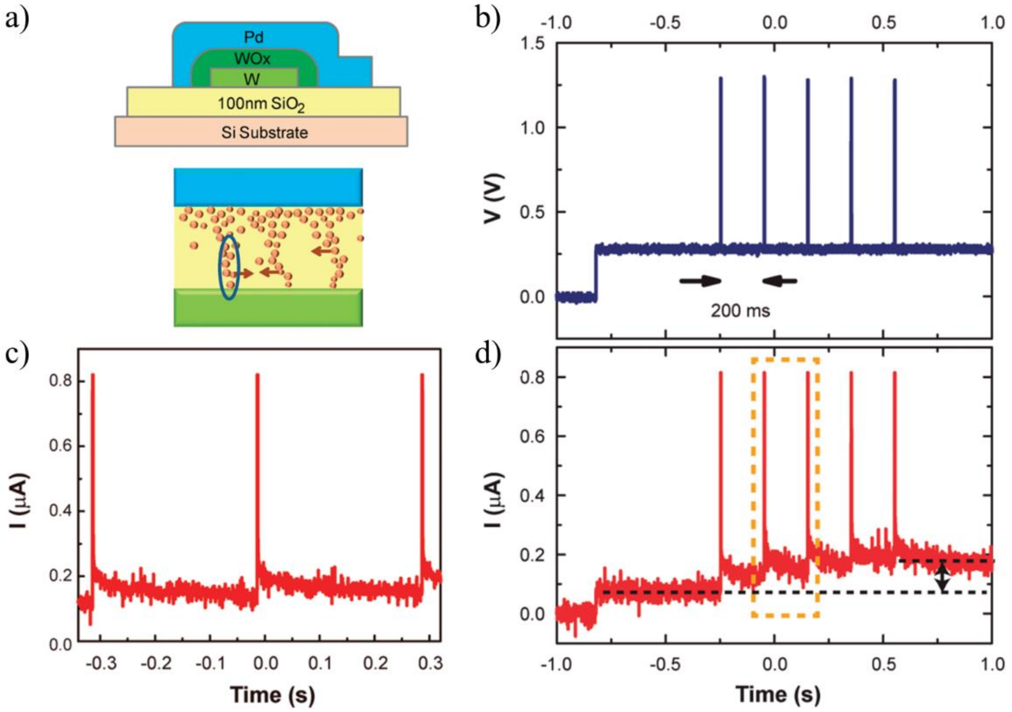

Figure I.5: a) Schematic of the device and oxygen vacancy filaments. b) Five electric pulse signals. c) STP is emulated when the spike interval was 299 ms. d) LTP is emulated for shorter spike interval of 199 ms. Figure adapted with permission from Reference 44; copyright 2011 American Chemical Society.

Phase change memory (PCM): Phase change materials are widely studied for memory applications due to their fast switching speed, high packing density and so on [21]. In a typical PCM device, a phase change material sandwiched in between two electrodes can be reversibly switched between a crystalline phase and an amorphous phase by Joule heating. The crystalline state shows a high conducting state while the amorphous state shows a low conducting state. Chalcogenide glass, GST ($Ge_2Sb_2Te_5$), is one of the most widely used materials for memory devices (Figure I.6) [4]. In general, a short electric pulse, Joule heats and quenches the material to create amorphous regions while a wide electric pulse is applied to crystallize the material by annealing. Cross-sectional TEM image shows the crystalline and amorphous regions formed in the GST material (Figure I.6b) and simulation of the generated temperature during the electrical pulse signal is depicted in Figure I.6c. The STDP beaviour is shown in Figure I.6d. Recently, STP and LTP behaviors were demonstrated in a lignin-based synaptic device (Figure I.6e-g) [45]. Joule heating results in the carbonization of lignin and can transform to an amorphous carbon matrix or to graphitic structures, which change the conductance state.

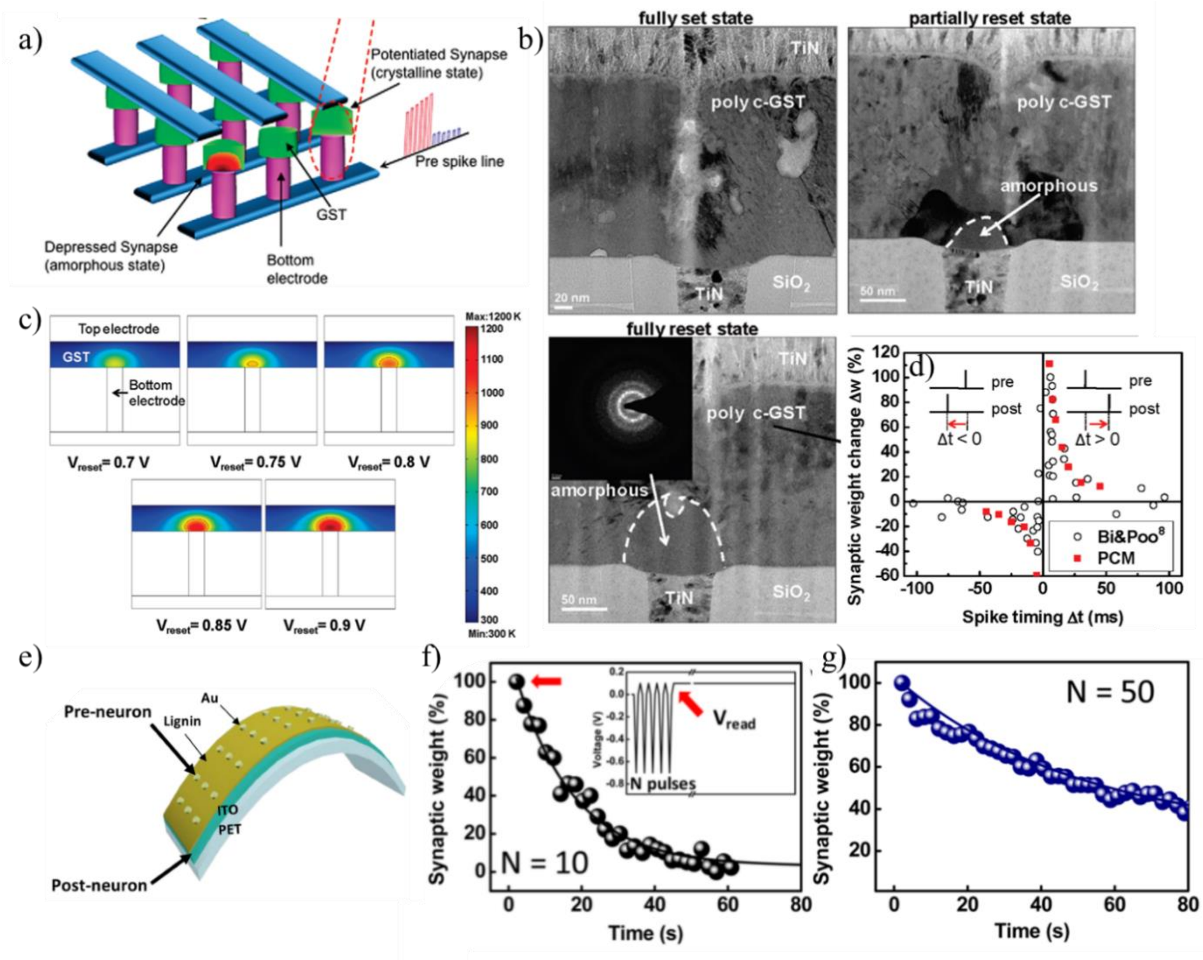

Figure I.6: a) Schematic of the PCM crossbar device array. b) Cross-sectional TEM images showing the crystalline and amorphous phase change in the material. c) Simulation showing the temperature generated during the electrical pulse signals. d) STDP. Figure adapted with permission from Reference 4; copyright 2012 American Chemical Society. e) Schematic of the lignin-based device. f) STP emulated with 10 pulses. Inset showing the pulse configuration. g) LTP emulated with 50 pulses. Figure adapted with permission from Reference 45; copyright 2017 American Chemical Society.

Trap assisted devices: It is highly possible to have defect states in materials or at their interfaces due to the presence of defects or dangling bonds formed during the fabrication process. These states can trap the carriers when the electric pulse is applied. After removing the pulse signal, the trapped charges slowly get released to the active channel giving rise to a decay nature to the device conductance/current, thus mimicking EPSC behavior. For intense pulse signals, the carriers get trapped in deep trap states leading to the permanent change of the device conductance emulating LTP. Several organic and inorganic materials and their interfaces have been explored in literature towards the fabrication of neuromorphic devices [3,35,46]. Figure I.7a shows a schematic representation of the shallow and deep trap states in an amorphous Si-based device [47]. When illuminated by light pulses, filling of shallow (illuminated by 635 nm wavelength) and deep (illuminated by 450 nm wavelength) trap states results in STP and LTP behavior (Figure I.7b,c). A commonly observed synaptic behavior, relearning, which requires less rehearsal, was also demonstrated in the device (Figure I.7d).

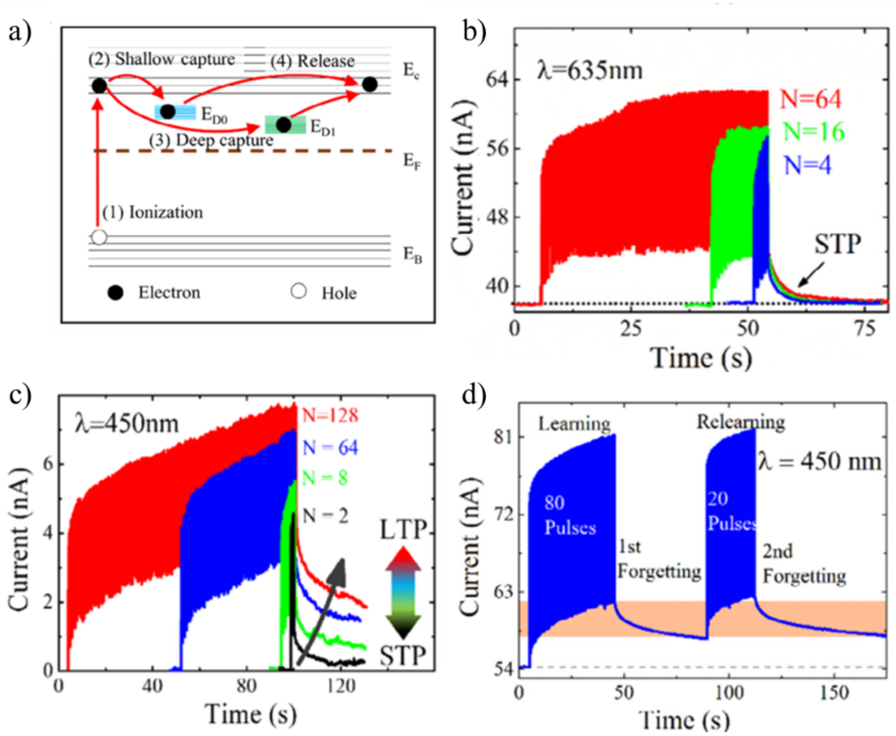

Figure I.7: a) Schematic of the trap states in amorphous Si-based device. b) Lower energy light illumination (635 nm) results in the capture of carriers in shallow trap states, thus emulating STP. c) Relatively higher energy light illumination (450 nm) results in the capture of carriers in both shallow and deep trap states, leading to STP and LTP formation. d) Relearning process with a lower number of rehearsal pulses. Figure adapted with permission from Reference 47; copyright 2020 John Wiley and Sons.

Ion migration: Ion migration is often observed in perovskite (ABX_3) based devices, where the halide (X) ions having low activation energy can migrate in response to the applied electric field [2]. In literature, a combination of halide ion migration and vacancy defects has been explored for artificial synaptic devices. In one example, organometal halide perovskite, $CH_3NH_3PbBr_3$ with buffer-capped conducting polymer were investigated to emulate synaptic activity (Figure I.8a) [29]. Since the activation energy of bromine ion (~ 0.2 eV) was lower than that of the lead ion (~ 0.8 eV), it migrates easily under an applied electric field and gets trapped in the vacancy defect (Figure I.8b) leading to the EPSC behavior (Figure I.8c).

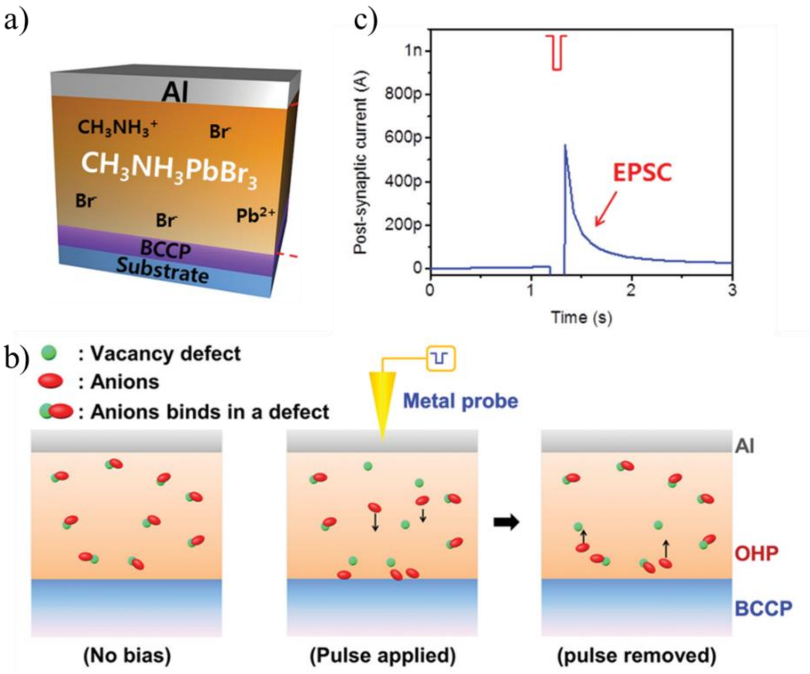

Figure I.8: a) Schematic of the device. b) Schematic showing the ion migration and trapping in the active region. c) EPSC response for the applied electric pulse. Figure adapted with permission from Reference 29; copyright 2016 John Wiley and Sons.

Emulating higher-order cognition

Apart from STP, LTP and SPDP, mimicking higher-order cognition is also important to accomplish next-generation neuromorphic artificial intelligence (Figure I.9a) [48]. Several reports in literature demonstrate emulation of complex cognitive function in devices often relying on CMOS supporting circuits [49–52]. Li et al., demonstrated sleep-wake cycle autoregulation in a Bi_2O_2Se/HfO_2 transistor relying on a complex CMOS based recurrent neural circuit model [53]. Associative learning is a complex activity performed by the brain, which helps the body to prepare for an expected or likely event.

In devices, this is demonstrated by mimicking the famous Pavlov's dog experiment [54]. An unconditioned signal (food) generates an unconditioned response (salivation). At the same

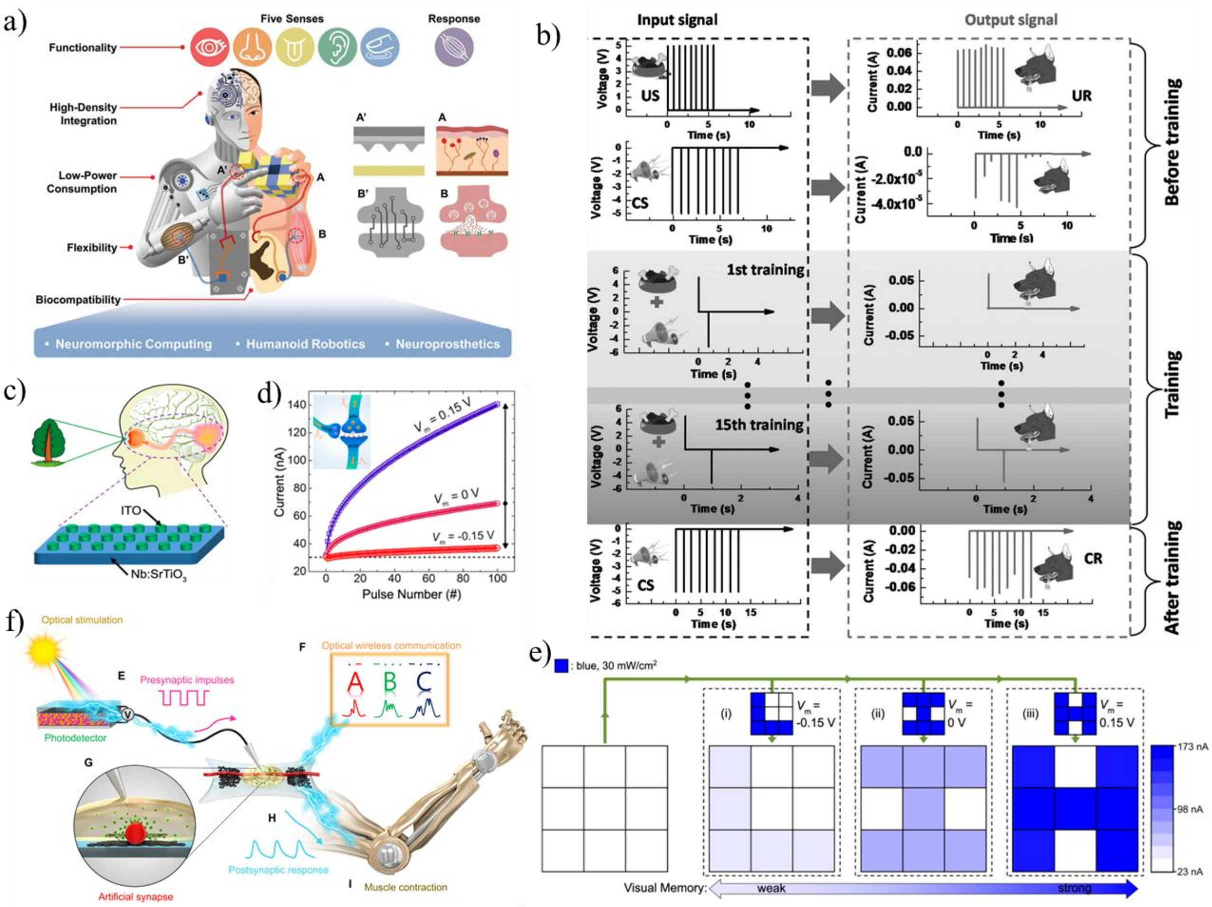

Figure I.9: a) Schematic showing the next-generation AI. Figure adapted with permission from Reference 48; copyright 2020 John Wiley and Sons. b) Classical conditioning mimicked in a neuromorphic device. Figure adapted with permission from Reference 58; copyright 2017 John Wiley and Sons. c) Schematic representation of an artificial visual system. d) Current modulation in an optoelectronic device with bias voltage. e) Interest-based memory formation. Figure adapted with permission from Reference 59; copyright 2019 American Chemical Society. f) Schematic of the device architecture for mimicking motor neuron function. Figure adapted with permission from Reference 60; copyright 2018 American Association for the Advancement of Science.

time, a conditioned signal (bell) does not generate any response. A training was then initiated by applying food and bell signals together so that, post-training, the bell signal alone generates the salivation response showing the association between the signals. In devices, food and bell are simulated by electrical pulse signals, and a conductance switch represents the salivation response. Hosaka et al., reported associative learning in a NiO$_x$

based device while relying on an external CMOS comparator circuit [50]. In the recent past, efforts have been found in literature to emulate human-like behaviors without the aid of supporting circuits [55–57]. Yang et al., demonstrated associative learning in a flexible Ag/Al_2O_3 device (Figure I.9b) [58]. A set voltage (+5 V) was applied as a food signal to which the device switches to a high conducting state (salivation) while a reset voltage (-5 V, as bell signal) keeps the device in a low conducting state (no response). During training, set and reset voltage is applied in succession such that, post-training, the device switches to a high conducting state for the reset voltage (association). In another example, Li et al., mimicked interest-based memory formation in an optoelectronic oxide-based Schottky junction synaptic device (Figure I.9c-e) [59]. In general, the photoresponse of a device can be modulated with the bias voltage. Thus, in the device, the bias voltage was increased to increase the device response, thereby the memory retention to mimic interest-based memory formation (Figure I.9d). It was shown that at a low bias voltage (low interest), the

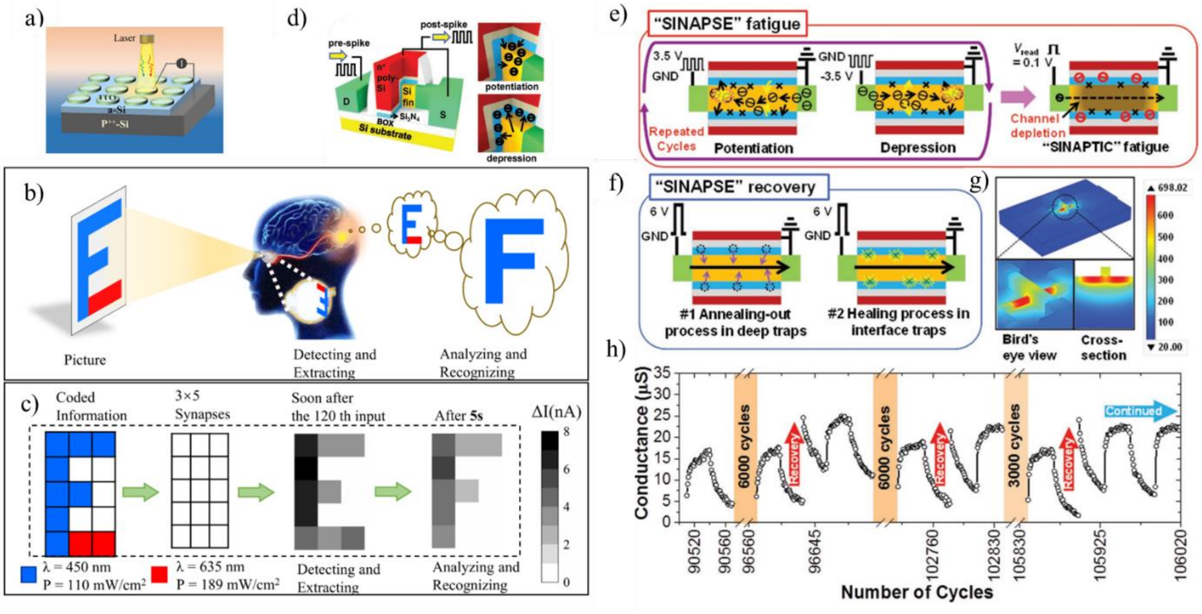

Figure I.10: a) Schematic of the optoelectronic device based on amorphous Si. b) Schematic of the artificial visual system and c) mimicking color-coded pattern recognition in the device. Figure adapted with permission from Reference 47; copyright 2020 John Wiley and Sons. d) Schematic of the poly-Si/SiO_2/Si_3N_4 FinFET. e) Carrier trapping in the device resulting in synaptic fatigue. f) Joule heating for releasing the trapped carriers. g) Simulation of temperature generation during Joule heating h) Fatigue and recovery of the device during electrical stimulation. Figure adapted with permission from Reference 61; copyright 2018 John Wiley and Sons.

memory retention of the device was poor while at a higher bias voltage (high interest), the memory retention was for a longer period (Figure I.9e). Lee et al. has reported an artificial neuromuscular system in an organic nanowire synaptic transistor (Figure I.9f) [60]. Synaptic activities under strain have also been demonstrated. On integrating a photodetector, the synaptic device was actuated for light signals, thus simulating motor response analogous to the biological muscle tension responses during contraction. A color recognizing artificial visual system was proposed by Li et al., in an amorphous Si-based photonic synapse (Figure I.10a) [47]. The device showed volatile and nonvolatile synaptic plasticity for different wavelengths of illumination. Thus, a pattern with color-coded information was illuminated and the device could identify the actual information (Figure I.10b,c). Due to excess learning activities, bio synapses undergo fatigue. Choi et al., demonstrated this synaptic fatigue and its recovery in a poly-Si/SiO_2/Si_3N_4 based FinFET device (Figure I.10d) [61]. After 10^5 cycles of electrical pulsing, the device conductance dropped, indicating fatigue. This was due to the carriers being captured in deep trap states (Figure I.10e). An electrical Joule heating was then performed to release these trapped carriers (Figure I.10f,g), thus recovering the device (Figure I.10h).

I.C Scope of the thesis

In this era of big data, computing platforms based on the conventional von Neumann computer architecture are failing to meet the computational demand. Neuromorphic devices show promising results in terms of mimicking efficient computational abilities of the human brain. An ideal neuromorphic device should be able to emulate higher-order brain cognition without the aid of software platforms or CMOS supporting circuits. It is clear from the preceding discussion that the present-day neuromorphic devices involve complex fabrication processes, intricate material designs, and emulate limited synaptic behaviors. Also, higher-order learning is mimicked in devices often relying on external CMOS supporting circuits. Also, it is essential to fabricate devices that mimic different human abilities such as visual system, flexible neurons and so on, for next-generation neuromorphic artificial intelligence. This thesis explores simple processes for fabrication of on-synapse intelligence, i.e. neuromorphic devices that emulate intelligence without the aid of external CMOS circuits or of software platforms.

References:

[1] S. Russel and P. Norvig, *Artificial Intelligence—a Modern Approach 3rd Edition* (Prentice Hall, 2012).

[2] J. Sun, Y. Fu, and Q. Wan, *Organic Synaptic Devices for Neuromorphic Systems*, J. Phys. D. Appl. Phys. **51**, 314004 (2018).

[3] W. Xu, S. Y. Min, H. Hwang, and T. W. Lee, *Organic Core-Sheath Nanowire Artificial Synapses with Femtojoule Energy Consumption*, Sci. Adv. **2**, e1501326 (2016).

[4] D. Kuzum, R. G. D. Jeyasingh, B. Lee, and H. S. P. Wong, *Nanoelectronic Programmable Synapses Based on Phase Change Materials for Brain-Inspired Computing*, Nano Lett. **12**, 2179 (2012).

[5] D. S. Jeong, K. M. Kim, S. Kim, B. J. Choi, and C. S. Hwang, *Memristors for Energy-Efficient New Computing Paradigms*, Adv. Electron. Mater. **2**, 1600090 (2016).

[6] W. H. Chen, W. S. Khwa, J. Y. Li, W. Y. Lin, H. T. Lin, Y. Liu, Y. Wang, H. Wu, H. Yang, and M. F. Chang, *Circuit Design for beyond von Neumann Applications Using Emerging Memory: From Nonvolatile Logics to Neuromorphic Computing*, Proc. - Int. Symp. Qual. Electron. Des. ISQED 23 (2017).

[7] A. Erdmann, H. Mesilhy, P. Evanschitzky, V. Philipsen, F. Timmermans, and M. Bauer, *Perspectives and Tradeoffs of Absorber Materials for High NA EUV Lithography*, J. Micro/Nanolithography, MEMS, MOEMS **19**, 041001 (2020).

[8] M. M. Waldrop, *The Chips Are down for Moore's Law*, Nature **530**, 144 (2016).

[9] T. H. Lee, H. G. Hwang, J. U. Woo, D. H. Kim, T. W. Kim, and S. Nahm, *Synaptic Plasticity and Metaplasticity of Biological Synapse Realized in a $KNbO_3$ Memristor for Application to Artificial Synapse*, ACS Appl. Mater. Interfaces **10**, 25673 (2018).

[10] L. L. Driscoll, *Cognitive Function*, in *Comprehensive Toxicology: Third Edition* (2018).

[11] Y. Yan, X. Wu, Q. Chen, X. Wang, E. Li, Y. Liu, H. Chen, and T. Guo, *An Intrinsically Healing Artificial Neuromorphic Device*, J. Mater. Chem. C **8**, 6869 (2020).

[12] D. H. Kang, J. H. Kim, S. Oh, H. Y. Park, S. R. Dugasani, B. S. Kang, C. Choi, R. Choi, S. Lee, S. H. Park, K. Heo, and J. H. Park, *A Neuromorphic Device Implemented on a Salmon-DNA Electrolyte and Its Application to Artificial Neural Networks*, Adv. Sci. **6**, 1901265 (2019).

[13] M. Davies, N. Srinivasa, T. H. Lin, G. Chinya, Y. Cao, S. H. Choday, G. Dimou, P. Joshi, N. Imam, S. Jain, Y. Liao, C. K. Lin, A. Lines, R. Liu, D. Mathaikutty, S. McCoy, A. Paul, J. Tse, G. Venkataramanan, Y. H. Weng, A. Wild, Y. Yang, and H. Wang, *Loihi: A Neuromorphic Manycore Processor with On-Chip Learning*, IEEE Micro **38**, 82 (2018).

[14] F. Akopyan, J. Sawada, A. Cassidy, R. Alvarez-Icaza, J. Arthur, P. Merolla, N. Imam, Y. Nakamura, P. Datta, G. J. Nam, B. Taba, M. Beakes, B. Brezzo, J. B. Kuang, R. Manohar, W. P. Risk, B. Jackson, and D. S. Modha, *TrueNorth: Design and Tool Flow of a 65 MW 1 Million Neuron Programmable Neurosynaptic Chip*, IEEE Trans. Comput. Des. Integr. Circuits Syst. **34**, 1537 (2015).

[15] C. D. Schuman, T. E. Potok, R. M. Patton, J. D. Birdwell, M. E. Dean, G. S. Rose, and J. S. Plank, *A Survey of Neuromorphic Computing and Neural Networks in Hardware*, ArXiv (2017).

[16] I. Arel, D. Rose, and T. Karnowski, *Deep Machine Learning-A New Frontier in Artificial Intelligence Research*, IEEE Comput. Intell. Mag. **5**, 13 (2010).

[17] D. Silver, A. Huang, C. J. Maddison, A. Guez, L. Sifre, G. Van Den Driessche, J. Schrittwieser, I. Antonoglou, V. Panneershelvam, M. Lanctot, S. Dieleman, D. Grewe, J. Nham, N. Kalchbrenner, I. Sutskever, T. Lillicrap, M. Leach, K. Kavukcuoglu, T. Graepel, and D. Hassabis, *Mastering the Game of Go with Deep Neural Networks and Tree Search*, Nature **529**, 484 (2016).

[18] D. Silver, T. Hubert, J. Schrittwieser, I. Antonoglou, M. Lai, A. Guez, M. Lanctot, L. Sifre, D. Kumaran, T. Graepel, T. Lillicrap, K. Simonyan, and D. Hassabis, *A General Reinforcement Learning Algorithm That Masters Chess, Shogi, and Go through Self-Play*, Science **362**, 1140 (2018).

[19] M. B. Hoy, *Alexa, Siri, Cortana, and More: An Introduction to Voice Assistants*, Med. Ref. Serv. Q. **37**, 81 (2018).

[20] *Http://Lup.Lub.Lu.Se/Student-Papers/Record/9021697*, (2020).

[21] Q. Wan, M. T. Sharbati, J. R. Erickson, Y. Du, and F. Xiong, *Emerging Artificial Synaptic Devices for Neuromorphic Computing*, Adv. Mater. Technol. **4**, 1900037 (2019).

[22] N. K. Upadhyay, H. Jiang, Z. Wang, S. Asapu, Q. Xia, and J. Joshua Yang, *Emerging Memory Devices for Neuromorphic Computing*, Adv. Mater. Technol. **4**, 1800589 (2019).

[23] S. H. Sung, D. H. Kim, T. J. Kim, I. S. Kang, and K. J. Lee, *Unconventional Inorganic-Based Memristive Devices for Advanced Intelligent Systems*, Adv. Mater. Technol. **4**, 1900080 (2019).

[24] P. Sheridan, W. Ma, and W. Lu, *Pattern Recognition with Memristor Networks*, Proc. - IEEE Int. Symp. Circuits Syst. 1078 (2014).

[25] S. N. Truong, *Single Crossbar Array of Memristors with Bipolar Inputs for Neuromorphic Image Recognition*, IEEE Access **8**, 69327 (2020).

[26] M. Chu, B. Kim, S. Park, H. Hwang, M. Jeon, B. H. Lee, and B. G. Lee, *Neuromorphic Hardware System for Visual Pattern Recognition with Memristor Array and CMOS Neuron*, IEEE Trans. Ind. Electron. **62**, 2410 (2015).

[27] I. Boybat, M. Le Gallo, S. R. Nandakumar, T. Moraitis, T. Parnell, T. Tuma, B. Rajendran, Y. Leblebici, A. Sebastian, and E. Eleftheriou, *Neuromorphic Computing with Multi-*

Memristive Synapses, Nat. Commun. **9**, 1 (2018).

[28] C. Lutz, T. Hasegawa, and T. Chikyow, *Ag_2S Atomic Switch-Based "tug of War" for Decision Making*, Nanoscale **8**, 14031 (2016).

[29] W. Xu, H. Cho, Y. H. Kim, Y. T. Kim, C. Wolf, C. G. Park, and T. W. Lee, *Organometal Halide Perovskite Artificial Synapses*, Adv. Mater. **28**, 5916 (2016).

[30] R. Yang, H. M. Huang, and X. Guo, *Memristive Synapses and Neurons for Bioinspired Computing*, Adv. Electron. Mater. **5**, 1900287 (2019).

[31] C. R. Raymond, *LTP Forms 1, 2 and 3: Different Mechanisms for the "long" in Long-Term Potentiation*, Trends Neurosci. **30**, 167 (2007).

[32] X. Pan, T. Jin, J. Gao, C. Han, Y. Shi, and W. Chen, *Stimuli-Enabled Artificial Synapses for Neuromorphic Perception: Progress and Perspectives*, Small **16**, 2001504 (2020).

[33] V. M. Ho, J. A. Lee, and K. C. Martin, *The Cell Biology of Synaptic Plasticity*, Science **334**, 623 (2011).

[34] S. Kim, C. Du, P. Sheridan, W. Ma, S. Choi, and W. D. Lu, *Experimental Demonstration of a Second-Order Memristor and Its Ability to Biorealistically Implement Synaptic Plasticity*, Nano Lett. **15**, 2203 (2015).

[35] S. M. Kwon, S. W. Cho, M. Kim, J. S. Heo, Y. H. Kim, and S. K. Park, *Environment-Adaptable Artificial Visual Perception Behaviors Using a Light-Adjustable Optoelectronic Neuromorphic Device Array*, Adv. Mater. **31**, 1906433 (2019).

[36] G. Milano, M. Luebben, Z. Ma, R. Dunin-Borkowski, L. Boarino, C. F. Pirri, R. Waser, C. Ricciardi, and I. Valov, *Self-Limited Single Nanowire Systems Combining All-in-One Memristive and Neuromorphic Functionalities*, Nat. Commun. **9**, 5151 (2018).

[37] T. Ohno, T. Hasegawa, T. Tsuruoka, K. Terabe, J. K. Gimzewski, and M. Aono, *Short-Term Plasticity and Long-Term Potentiation Mimicked in Single Inorganic Synapses*, Nat. Mater. **10**, 591 (2011).

[38] C. S. Dash and S. R. S. Prabaharan, *Nano Resistive Memory (Re-RAM) Devices and Their Applications*, Rev. Adv. Mater. Sci. **58**, 248 (2019).

[39] I. Valov, R. Waser, J. R. Jameson, and M. N. Kozicki, *Electrochemical Metallization Memories - Fundamentals, Applications, Prospects*, Nanotechnology **22**, 254003 (2011).

[40] T. Fu, X. Liu, H. Gao, J. E. Ward, X. Liu, B. Yin, Z. Wang, Y. Zhuo, D. J. F. Walker, J. Joshua Yang, J. Chen, D. R. Lovley, and J. Yao, *Bioinspired Bio-Voltage Memristors*, Nat. Commun. **11**, 1861 (2020).

[41] S. La Barbera, D. Vuillaume, and F. Alibart, *Filamentary Switching: Synaptic Plasticity through Device Volatility*, ACS Nano **9**, 941 (2015).

[42] G. Milano, S. Porro, I. Valov, and C. Ricciardi, *Recent Developments and Perspectives for Memristive Devices Based on Metal Oxide Nanowires*, Adv. Electron. Mater. **5**, 1800909 (2019).

[43] D. Acharyya, A. Hazra, and P. Bhattacharyya, *A Journey towards Reliability Improvement of TiO_2 Based Resistive Random Access Memory: A Review*, Microelectron. Reliab. **54**, 541 (2014).

[44] T. Chang, S. H. Jo, and W. Lu, *Short-Term Memory to Long-Term Memory Transition in a Nanoscale Memristor*, ACS Nano **5**, 7669 (2011).

[45] Y. Park and J. S. Lee, *Artificial Synapses with Short- and Long-Term Memory for Spiking Neural Networks Based on Renewable Materials*, ACS Nano **11**, 8962 (2017).

[46] J. Sun, S. Oh, Y. Choi, S. Seo, M. J. Oh, M. Lee, W. B. Lee, P. J. Yoo, J. H. Cho, and J. H. Park, *Optoelectronic Synapse Based on IGZO-Alkylated Graphene Oxide Hybrid Structure*, Adv. Funct. Mater. **28**, 1804397 (2018).

[47] D. Li, C. Li, N. Ilyas, X. Jiang, F. Liu, D. Gu, M. Xu, Y. Jiang, and W. Li, *Color-Recognizing Si-Based Photonic Synapse for Artificial Visual System*, Adv. Intell. Syst. **2**, 2000107 (2020).

[48] H. L. Park, Y. Lee, N. Kim, D. G. Seo, G. T. Go, and T. W. Lee, *Flexible Neuromorphic Electronics for Computing, Soft Robotics, and Neuroprosthetics*, Adv. Mater. **32**, 1903558 (2020).

[49] O. Bichler, W. Zhao, F. Alibart, S. Pleutin, S. Lenfant, D. Vuillaume, and C. Gamrat, *Pavlov's Dog Associative Learning Demonstrated on Synaptic-like Organic Transistors*, Neural Comput. **25**, 549 (2013).

[50] S. G. Hu, Y. Liu, Z. Liu, T. P. Chen, Q. Yu, L. J. Deng, Y. Yin, and S. Hosaka, *Synaptic Long-Term Potentiation Realized in Pavlov's Dog Model Based on a NiOx-Based Memristor*, J. Appl. Phys. **116**, 214502 (2014).

[51] X. Wan, D. Liang, F. Gao, X. Lian, and Y. Tong, *Hardware Implementation of Classical Conditioning with Iron-Oxide-Based Memristors*, Appl. Phys. Express **11**, 114601 (2018).

[52] M. Ziegler, R. Soni, T. Patelczyk, M. Ignatov, T. Bartsch, P. Meuffels, and H. Kohlstedt, *An Electronic Version of Pavlov's Dog*, Adv. Funct. Mater. **22**, 2744 (2012).

[53] Z. Zhang, T. Li, Y. Wu, Y. Jia, C. Tan, X. Xu, G. Wang, J. Lv, W. Zhang, Y. He, J. Pei, C. Ma, G. Li, H. Xu, L. Shi, H. Peng, and H. Li, *Truly Concomitant and Independently Expressed Short- and Long-Term Plasticity in a Bi2O2Se-Based Three-Terminal Memristor*, Adv. Mater. **31**, 1805769 (2019).

[54] I. P. Pavlov, *Conditioned Reflexes: An Investigation of the Physiological Activity of the Cerebral Cortex*, Ann. Neurosci. **17**, 136 (2010).

[55] L. Yin, W. Huang, R. Xiao, W. Peng, Y. Zhu, Y. Zhang, X. Pi, and D. Yang, *Optically Stimulated Synaptic Devices Based on the Hybrid Structure of Silicon Nanomembrane and Perovskite*, Nano Lett. **20**, 3378 (2020).

[56] R. A. John, N. Tiwari, C. Yaoyi, Ankit, N. Tiwari, M. Kulkarni, A. Nirmal, A. C. Nguyen, A. Basu, and N. Mathews, *Ultralow Power Dual-Gated Subthreshold Oxide Neuristors: An Enabler for Higher Order Neuronal Temporal Correlations*, ACS Nano **12**, 11263 (2018).

[57] X. Wang, Y. Yan, E. Li, Y. Liu, D. Lai, Z. Lin, Y. Liu, H. Chen, and T. Guo, *Stretchable Synaptic Transistors with Tunable Synaptic Behavior*, Nano Energy **75**, 104952 (2020).

[58] C. Wu, T. W. Kim, T. Guo, F. Li, D. U. Lee, and J. J. Yang, *Mimicking Classical Conditioning Based on a Single Flexible Memristor*, Adv. Mater. **29**, 1602890 (2017).

[59] S. Gao, G. Liu, H. Yang, C. Hu, Q. Chen, G. Gong, W. Xue, X. Yi, J. Shang, and R. W. Li, *An Oxide Schottky Junction Artificial Optoelectronic Synapse*, ACS Nano **13**, 2634 (2019).

[60] Y. Lee, J. Y. Oh, W. Xu, O. Kim, T. R. Kim, J. Kang, Y. Kim, D. Son, J. B. H. Tok, M. J. Park, Z. Bao, and T. W. Lee, *Stretchable Organic Optoelectronic Sensorimotor Synapse*, Sci. Adv. **4**, eaat7387 (2018).

[61] J. Hur, B. C. Jang, J. Park, D. Il Moon, H. Bae, J. Y. Park, G. H. Kim, S. B. Jeon, M. Seo, S. Kim, S. Y. Choi, and Y. K. Choi, *A Recoverable Synapse Device Using a Three-Dimensional Silicon Transistor*, Adv. Funct. Mater. **28**, 1804844 (2018).

Chapter II

Fabrication and Characterization Techniques

In this thesis, neuromorphic devices have been designed to emulate various human-like cognitive activities. To synthesize, characterize, and study them, a state-of-the-art laboratory environment with the necessary, appropriate tools is required. This chapter summarizes the establishment of the cleanroom facility and the details of the instruments used for characterization.

Cleanroom Fabrication Facility:

Various fabrication and characterization tools discussed below were set up in a class 1000 cleanroom facility. The operation conditions and fabrication recipes were optimized. This facility will continue to serve its purpose for various fabrication and device studies.

Cleanroom facility

Characterization techniques:

Scanning Electron Microscopy (SEM) and Energy Dispersive X-ray Spectroscopy (EDX)

SEM was performed using a Nova NanoSEM 600 and Inspect 50 equipment (FEI Co., The Netherlands). EDX mapping was performed using EDX Genesis V4.52 (USA) attached to the SEM column operating at 15 kV.

Transmission Electron Microscopy (TEM)

Transmission electron microscopy (TEM) measurements were carried out with a FEI TALOS F200S G2 instrument. Samples for TEM were prepared by transferring the materials on a holey carbon Cu grid.

X-ray Diffraction (XRD)

XRD measurements were performed using a Rigaku diffractometer.

X-ray Photoelectron Spectroscopy (XPS)

XPS was carried out with OMICRON spectrophotometer (1 x 10^{-10} Torr vacuum) with an X-ray source of Al Kα (1486.6 eV). Samples for XPS (solid substrates) were mounted on the stub using high vacuum compatible Ag paint and drying in a vacuum.

Optical Microscope

The optical microscope from Leica Microsystems (DM2700M), with objectives of 5-150x, was used to capture images in reflective and transmission modes.

UV-vis spectroscopy

Reflectance measurements were performed using a Perkin-Elmer Lambda 900 UV/vis/NIR spectrophotometer.

Atomic Force Microscopy (AFM) and Conducting AFM (CAFM)

Sample topography and thickness analysis were performed using the Bruker Innova AFM instrument. Contact and tapping modes were used for surface analysis. Electrical measurements were carried out using conducting mode, where a conducting tip was contacted on the sample surface with applied bias voltage. Both the height and deflection/amplitude information were recorded at a scan rate of 1 Hz, and stored in a 512 × 512 pixel format. Images were processed using offline softwares.

Keithley Semiconductor Characterization System

Electrical characterization of the device was performed using Keithley 4200, 2450, 2461 and 4225 PMU. Regular I-V and voltage list sweeps were used for generating linear and customized pulse signals.

Probestation

Vacuum Probestation (up to 10^{-7} Torr) with four micro-positioners was used along with Keithley for electrical measurements. Gold-coated tungsten tip (10 μm tip size) was used to make electrical contact with the device contact pads.

Linkam Temperature Stage

Temperature-dependent measurements were carried out using a Linkam temperature stage under a nitrogen atmosphere.

Optical Chopper

Light pulses for photoresponse measurement were generated using Thorlabs MC 1000A optical chopper.

Oscilloscope

Analog signals were measured using Tektronix DPO 4104 oscilloscope with a 1 GHz sampling frequency.

Maskless Photolithography

Image sensors and gap electrodes were fabricated using IMP SF 100 maskless optolithography instrument. The DMD micromirror chip allows patterned UV light (365 nm) according to the software mask, thus avoiding the requirement of a physical mask.

Chapter IIIA

An Artificial Synaptic Network: Fabrication, Characterization, and Emulating Synaptic Activity *

Summary

A novel structure resembling the biological neural network has been realized based on a simple self-forming process. The self-formed Ag artificial synaptic network with branched islands resembled neurons, synaptic junctions and neurotransmitters. Electromigration of metal between the nanogaps in response to the applied electric field was found responsible for the switching behavior and different neuroplasticity. This hierarchical structure facilitated various learning activities such as STP, LTP, potentiation, depression and spike parameter dependent plasticity. The self-assembly technique was highly reproducible. Remarkably, the fabricated device showed excellent stability over a year.

IIIA.1 Introduction

Human brain, comprising of nearly hundred billion neurons with several order higher number of synapses, accomplishes massive parallel processing and unmatched cognitive actions, which in essence is the subjective conscious intelligence experienced by every individual [1]. Inspired by this, efforts are on worldwide to develop artificial intelligence (AI) and in particular artificial neural networks (ANNs), to mimic intelligence with the help of complex algorithms incorporated on the currently available high-speed computational platforms [2]. However, solving intricate real-world problems, unstructured data classification, pattern recognition etc., which a biological brain routinely deals with in real time, have posed tremendous challenges even to the state-of-the-art computers [3]. The present day computing is based on von Neumann architecture with physically distinct process and memory units and their swift communication required for high end computing poses a clear challenge [4]. In other words, sequential processing available with the present configuration is expensive in terms of energy, space as well as speed [5,6], which a biological brain manages extremely efficiently. A biological synaptic junction, unlike the conventional computing units, appears to handle both processing and memory parallelly [7], an aspect

---

*Paper based on this study: Mater.Horiz., **7**, 2970 (2020).

closely linked to its ability to change with the circumstance, termed neuroplasticity [8]. While neuroplasticity in relation to memory and processing is still being investigated, efforts in the literature are on the increase to mimic different levels of neuroplasticity using artificial synaptic devices [9,10].

Short-term potentiation (STP) and long-term potentiation (LTP) are the basic synaptic functions essential for neuroplasticity. Like potentiation, the depression and spike parameter dependent plasticity (SPDP) are also an essential aspect of the neuroplasticity that contributes to the learning activity. Biologically, this is achieved by increasing/decreasing the influx of ions (Na^+, K^+, Ca^{2+}) at a neuron which bind around the synaptic vesicle thereby inducing the release of neurotransmitters responsible for the synaptic plasticity [9,11]. Higher the ion concentration in the synaptic cleft, higher is the synaptic strength modulation. Given these bio-findings, artificial synaptic devices employ conductance change of the active channel whose strength and retention (short-term or long-term) can be defined by the voltage pulse/spiking parameters. Wide range of materials and their interfaces have been explored to mimic this synaptic plasticity in devices. Both organic and inorganic materials have displayed impressive synaptic activities [4,9,12-16]. Oxides such as TiO_2, HfO_2, TaO and ZnO and their interfaces [15-21] facilitate electric field assisted conducting channels via drifting of ions/vacancy, thus serving a memristive behavior, are also capable of synaptic actions [22]. Similarly, electrochemical metallization (ECM) based synaptic devices such as Ag_2S based atomic switch and Ag/Ag_2S junctions have also been developed [23-25]. Recently, diffusion based memristors have also been realized and combining them with resistive memory devices have resulted in varied synaptic plasticity [26]. In addition, carrier trapping and detrapping interfaces responding to either optical or electrical stimulus have also been demonstrated to serve as potential synaptic junctions [27-29]. Recently, a self-assembly technique was also introduced as an additional fabrication step for improved device performance [30-32]. However, these vacancy and trap based devices provide a capacitive decay nature to the conductance which is rather best suited to represent the forgetting nature of memory [33] in contrast to dynamically stable memory obtained using metallic filaments. Although these devices were able to mimic the aforementioned basic synaptic actions, they involve intricate fabrication processes and are generally expensive. Moreover, efforts are concentrated on fabricating single synaptic junctions rather than mimicking hierarchical bio neural network which is the reason for accomplishing massive cognitive actions.

IIIA.2 Scope of the present investigation

A synaptic device forms an essential component of hardware-based neuromorphic artificial intelligence. These brain-inspired intelligent devices are more efficient in terms of speed, energy and space. Most present-day synaptic devices attempt to emulate only basic synaptic functions and involve intricate fabrication processes often demanding precise stoichiometric combination. Also, the device architecture is focused to fabricate single synaptic junction in lieu of exploring colossal network as in the brain. Fabrication of synaptic devices based on self-forming process is not explored much. This method, if applied, is benefited with easy processing, scalability and cost-effectiveness. Here a novel device architecture is proposed for synaptic device fabrication. A device architecture containing a dewetted island-structured Ag film on glass substrate was realized which could exhibit learning behaviors.

IIIA.3 Experimental details

Ag-ASN fabrication: Glass or SiO_2/Si substrate was sonicated in acetone, IPA and DI water for 5 min and dried under nitrogen. The substrate was then loaded to e-beam evaporator for Ag deposition. ~30 nm Ag was deposited at chamber vacuum of ~10^{-6} torr. Later the substrate was placed on a hot plate maintained at 300 °C for 30 s and then immediately cooled to room temperature by placing on a cold surface.

Device fabrication: Au gap electrodes were fabricated by shadow masking technique and maskless photolithography.

IIIA.4 Results and discussion

As the first step in device fabrication (see Schematic in Figure IIIA.1a), a ~ 30 nm thick Ag film was deposited on the substrate (glass or SiO_2(300 nm)/Si) using a e-beam evaporator, which was then subjected to heating at 300 °C in ambient air for 30 s. This caused dewetting of the uniform film to form nanostructured island-like morphology. The presence of residual stress in the deposited film and the surface free energy difference between the film and the substrate may drive this transformation [34]. The surface roughness of the dewetted film as obtained from AFM measurement was ~ 35 nm (Figure IIIA.1b) with the height profile displaying the variation in the island thickness. From the SEM image in Figure IIIA.1c, it is evident that the film is discontinuous with particle size ranging from 50 to 500 nm. These particles appear to have coalesced to form locally connected agglomerate networks with random branches extending over few µms, also seen in the magnified AFM image (Figure

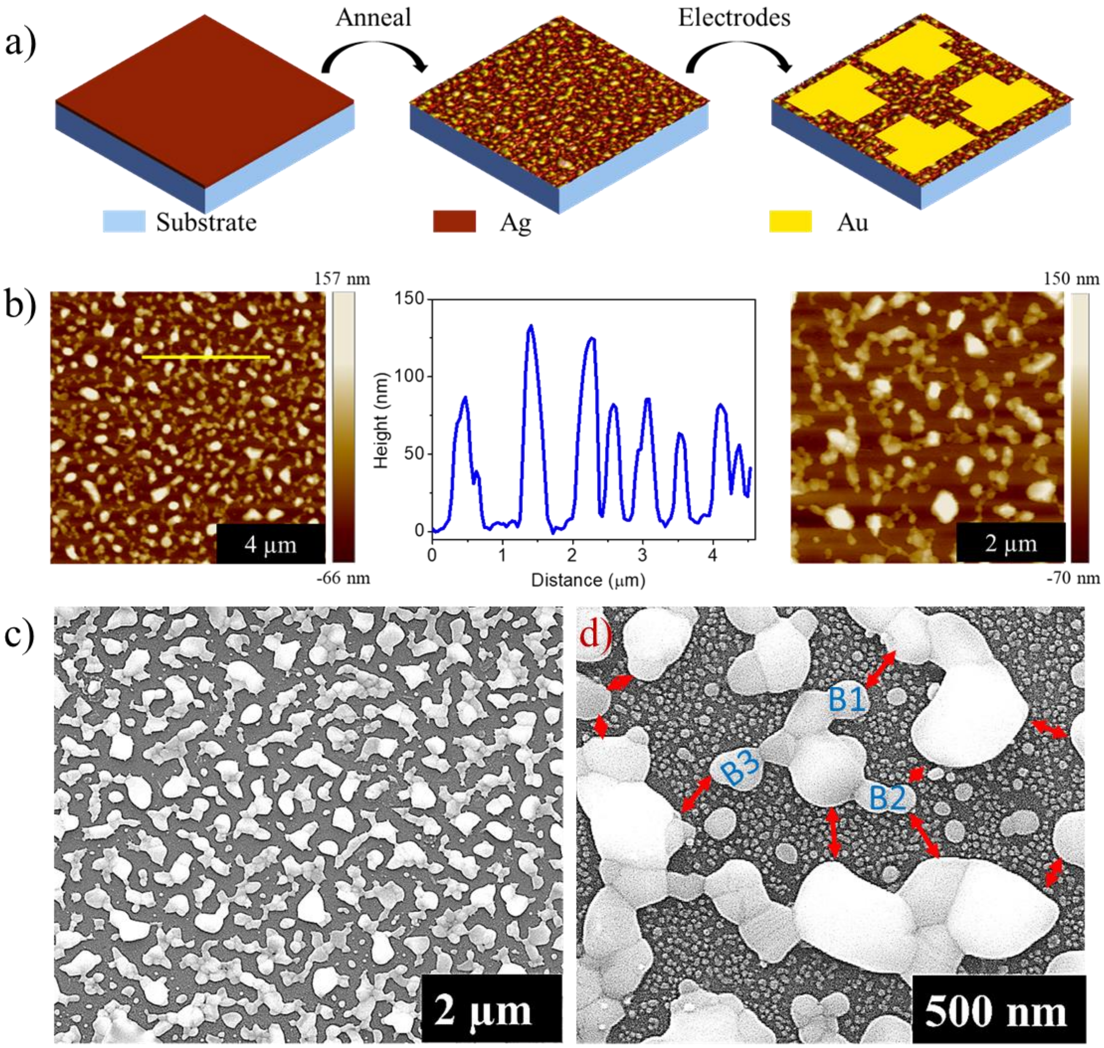

Figure IIIA. 1: a) Schematic of the device fabrication process. b) Low and high magnification contact mode AFM imaging of the annealed film. Height profile along the yellow line is shown. c) SEM image of the annealed film showing the discontinuous agglomerates. d) Magnified SEM view revealing the presence of smaller nanoparticles between the agglomerates (red arrows indicate the nanogaps). An agglomerate is shown with branches marked (B1, B2, B3).

IIIA.1b). Such local networks are seen separated from one another by nanogaps (see red marks in Figure IIIA.1d). From the microscopy analysis, it may be observed that the islands tend to branch out typically hosting around 5 branches. At a higher magnification, one may observe that the nanogaps are filled with smaller Ag nanoparticles whose average diameter is ~ 20 nm as estimated from the histogram in Figure IIIA.2. This bimodal size distribution serves favourably to form artificial synaptic network (Ag-ASN) which is the subject matter of interest.

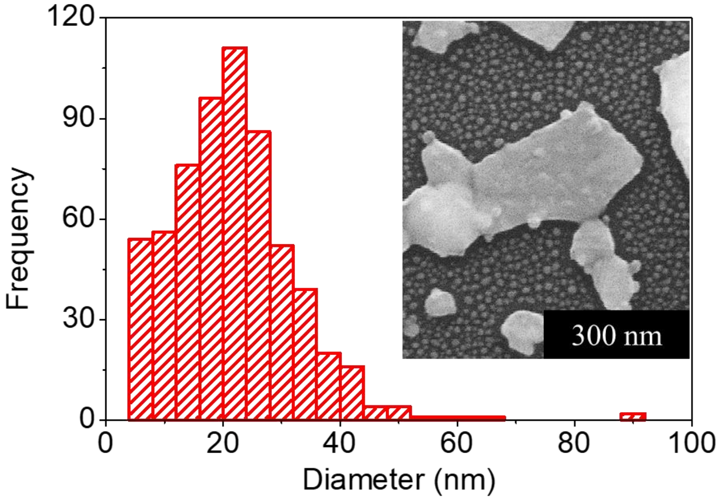

Figure IIIA.2: Size distribution of the small Ag particles (inset) present in between the agglomerates.

While causing dewetting of the Ag film, there is a possibility of surface oxidation. This was examined by subjecting the film to XRD, XPS and HAADF-STEM elemental mapping. HAADF image of the transferred Ag particles is shown in Figure IIIA.3a and the corresponding STEM elemental mapping, shown in Figure IIIA.3b, confirms the presence of Ag in major quantity with no detectable oxygen signal which is also seen in the line profile (Figure IIIA.3c). The lattice fringes in the HRTEM image shown in Figure IIIA.3d, are indexable to Ag(111). Further, XRD pattern shown in Figure IIIA.3e also confirms that there is no detectable oxidation of Ag metal. Since the above techniques are limited to bulk of the material, the film was subjected to XPS analysis to probe the surface in more detail. Core level XP spectra is shown in Figure IIIA.3f. It can be noted that there is a negative shift (0.4 eV) in the 3d peak position which can be attributed to the mild surface oxidation. From all these techniques, it was confirmed that there is no significant oxidation during the thermal treatment, which is in accordance with the literature [35].

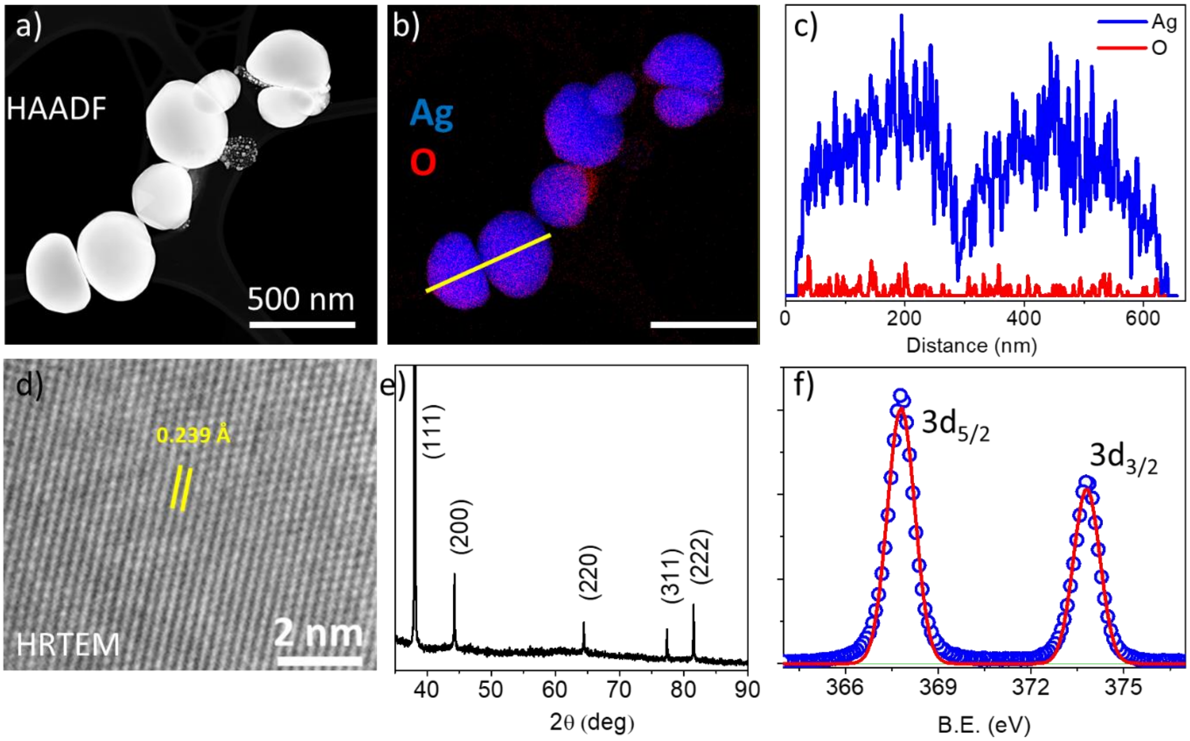

Figure IIIA.3: a) HAADF image of the Ag granules transferred on to the holey carbon grid b) elemental mapping c) elemental line profile along the yellow line in (b) revealing the Ag dominance with no detectable oxidation. d) HRTEM image of the Ag particle and the lattice fringes are indexable to Ag(111). e) XRD pattern of the annealed film on glass showing the dominant (111) peak with no detectable oxidation. f) Core level XP spectra in Ag 3d region.

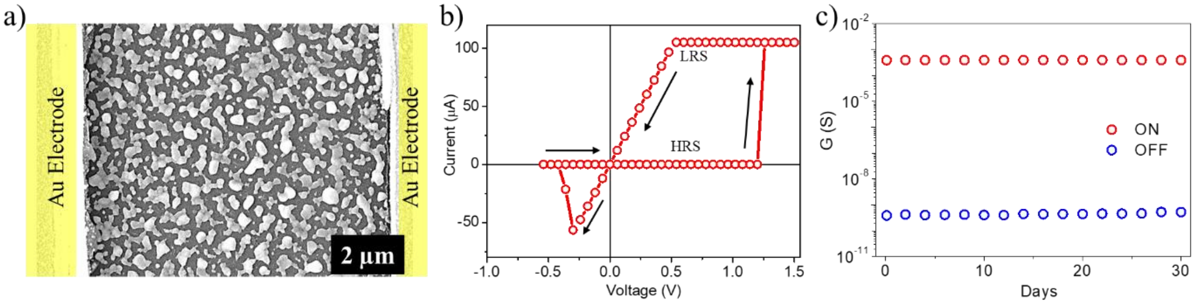

Figure IIIA.4: Electrical characteristics of the synaptic device. a) SEM image of the device. b) Typical I-V response of the synaptic device (current compliance = 100 μA). c) Conduction retention of the permanently switched device.

The device fabrication was completed by establishing Au electrodes separated by ~ 7 μm on the island Ag film (Ag-ASN) via e-beam evaporation (FigureIIIA.4a). FigureIIIA.4b shows the I-V characteristics of the device exhibiting typical switching behavior. Initially, the device was in the high resistance state (HRS, typically > 1 GΩ) which is understandable as Ag-ASN consists of discontinuous islands barely connected. With the bias voltage sweeping in positive polarity (0 - 1.5 V), the device switched to a low resistance state (LRS, ~ 5 kΩ) which is seen as saturation for the set current compliance of 100 μA. It continued to retain the state even on reversing the voltage down to ~ -0.3 V, when it resets itself into the high resistance state. When the device was permanently switched, an excellent conductance retention over 30 days was observed as shown in Figure IIIA.4c. The measured on/off ratio was as high as ~ 10^6. Since the Ag-ASN consists of disconnected sub-micrometer islands with nanoparticles spread in between, the conduction at low voltages is expected to be dominated by tunneling. At the threshold voltage and beyond, the electric field may be sufficient to drive the formation of conductive bridges across the nanogaps leading to the low resistance state of the device.

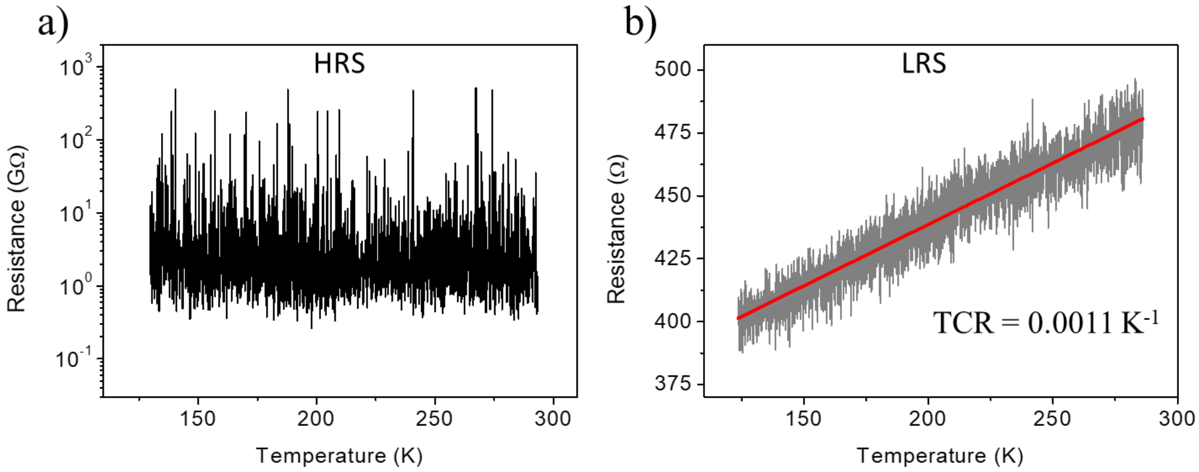

Figure IIIA.5: Temperature dependent electrical resistance of the device. a) Temperature independent resistance reflects the tunneling type conduction in high resistance state. b) Linear increase in low resistance state with temperature indicates the metallic nature of the conduction filaments. Bias voltage was 100 mV.

Temperature dependent resistance measurements in Figure IIIA.5a show that the HRS is independent of the temperature which confirms the tunneling based conduction. Its nature was carefully examined (see Figure IIIA.6) following the field enhanced thermionic emission (FE) and Fowler–Nordheim (FN) tunneling models [36].

$$I \propto AT^2 exp\left[-\frac{q\varphi}{kT} + q\left(\frac{q^3V}{4\pi\varepsilon}\right)^{1/2}\right] \qquad \text{(IIIA.1)}$$

$$I \propto V^2 \exp\left[\frac{-kd}{V}\right] \qquad \text{(IIIA.2)}$$

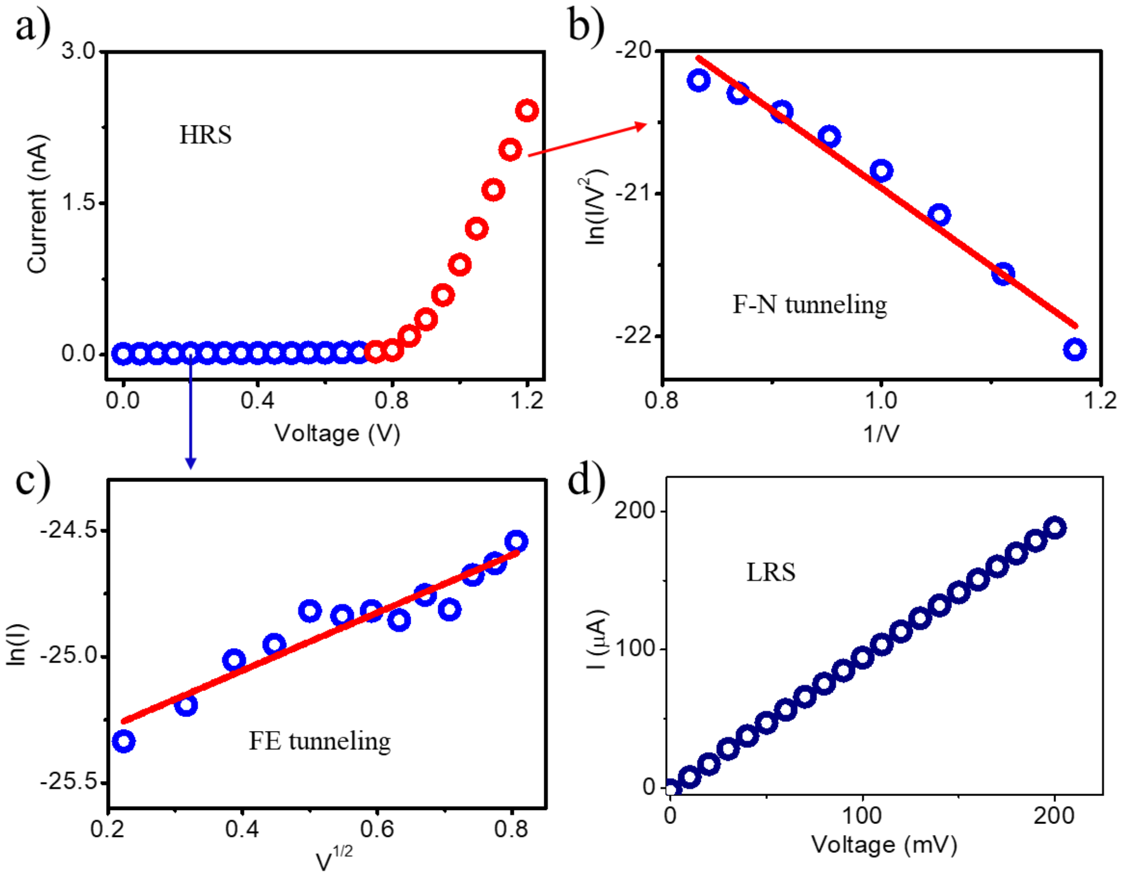

Figure IIIA.6: Conduction mechanism in HRS and LRS state. a) I-V characteristics in HSR state was analysed with b) F-N tunnelling and c) FE tunnelling. d) ohmic nature displayed in LRS state.

Where I is the current, V, voltage, A, Richardson's constant, T, absolute temperature, ε, dielectric permittivity, q, electronic charge, φ, barrier height and k, Boltzmann constant. A linear relation between ln(I) and $V^{1/2}$ is followed below ~ 0.7 V (see Figure IIIA.6c), indicating the domination of FE tunneling and at higher voltages, the linearity is seen in the variation of ln(I/V^2) with 1/V, supporting the F-N tunneling (Figure IIIA.6b). Beyond ~ 1.2

V, the electric field is high enough to cause electromigration of Ag atoms bridging the nanogaps thereby switching ON the device. The ohmic nature of the filaments was confirmed by the linear I-V (Figure IIIA.6d) as well as from the temperature dependence of the LRS (Figure IIIA.5b) with a coefficient (TCR) of ~ 0.0011 K^{-1}, less than that of the bulk (0.0038 K^{-1}), which is expected for disordered systems. The presence of conducting metallic filaments under the applied voltage was also observed in conducting AFM measurements (Figure IIIA.7).

Current compliance set during the device switching is known to influence the I-V characteristics. Here I-V sweep was performed with different compliance level ranging from 10 – 100 μA as shown in Figure IIIA.8. During 10 μA compliance, the device switched to high conducting state and while retracing back, conductance drops to original value before reaching 0 V (Figure IIIA.8a) suggesting weak stability of switched state. When the compliance was increased to 50 μA (Figure IIIA.8b) and then to 100 μA (Figure IIIA.8c), the stability of switched state became better which is observed as high conducting state during the mild reverse voltage sweep. This indicates that retention of conducting state can be tuned with current compliance which in turn can emulate STP and LTP. In order to emulate the STP

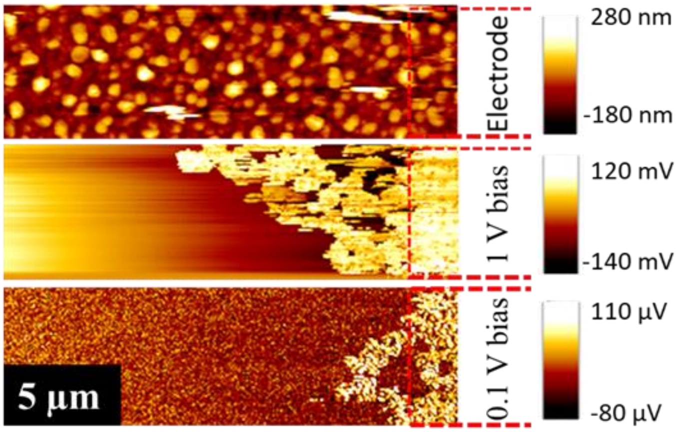

Figure IIIA.7: Conducting AFM measurement was performed to realize the conduction path created in the device during electrical bias. Top figure shows the contact mode topography image of the device. For CAFM, the electrode was connected to ground and the tip was biased. When the tip was biased at 1 V, conduction path appeared due to the electromigration of Ag to bridge the nanogap. Due to the short-term stability these filaments relax back and when scanned with 0.1 V tip bias, majority of the conduction paths were vanished except for those near the electrode.

and LTP memory in the present device, a pulse sequence was adopted along with a current compliance, as it is customarily done for such devices [24]. After examining the I-V sweep at different rates, a pulse sequence, 20 pulses of 2 V amplitude with 50 ms width as well as interval (Figure IIIA.9), was found optimal. The chosen pulse sequence was applied with a background reading voltage of 0.1 V as shown in Figure IIIA. 10 (lower panel) with the current compliance set to 100 µA. During the pulse sequence, the device switched to LRS (high conducting state) and the conductance state was retained beyond the pulse sequence for few seconds (0.1 - 20 s) before decaying back to HRS (low conducting state), thus emulating STP (Figure IIIA.10 and Figure IIIA.11a). Increasing compliance for applied 20 pulses varied the STP retention showing the possibility of STP to LTP transition and when the compliance was increased to 500 µA, the device retained high conductance even beyond 1500 s, thus emulating LTP.

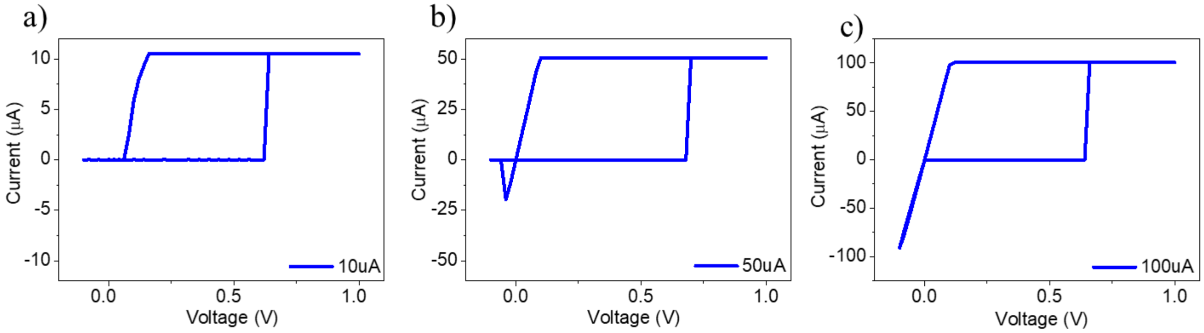

Figure IIIA.8: I-V characteristics under different current compliance of a) 10 µA b) 50 µA c) 100 µA.

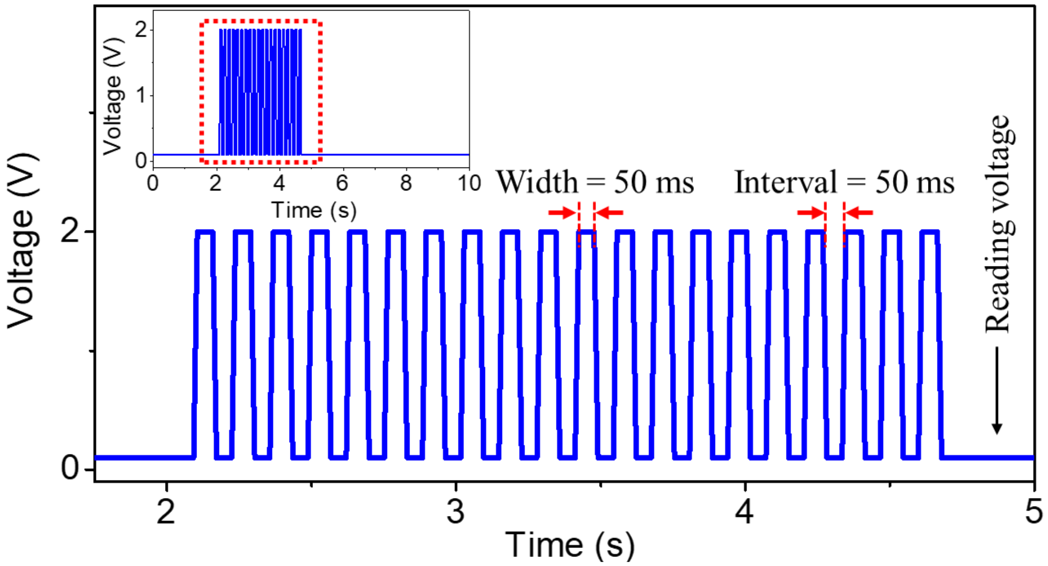

Figure IIIA.9: Pulse configuration. 20 pulses of 2 V amplitude and 50 ms width as well as interval with 0.1 V reading voltage.

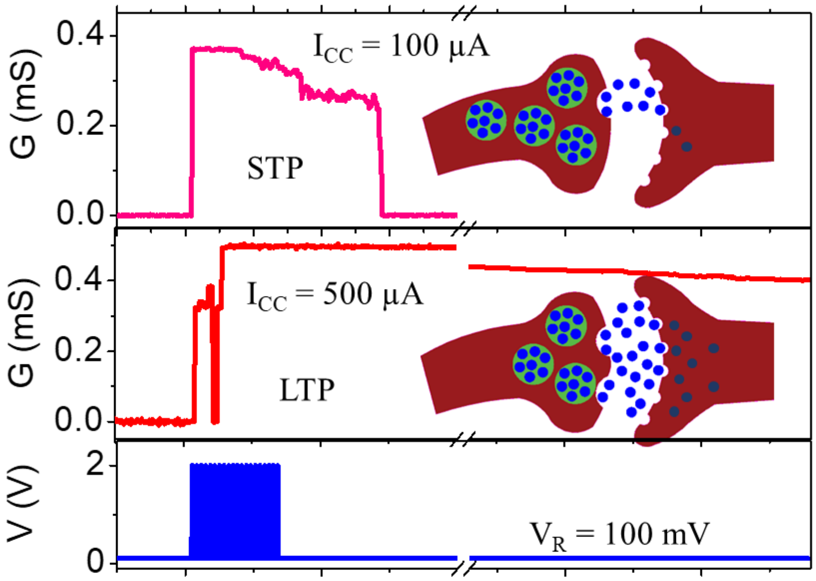

Figure IIIA.10: Synaptic behavior emulated with pulsed voltage signals. Bottom panel represents the voltage signal of 2 V amplitude. Short-term potentiation is emulated with 100 μA current compliance while long-term potentiation is emulated with 500 μA current compliance. Inset shows a schematic of a neuronal synapse.

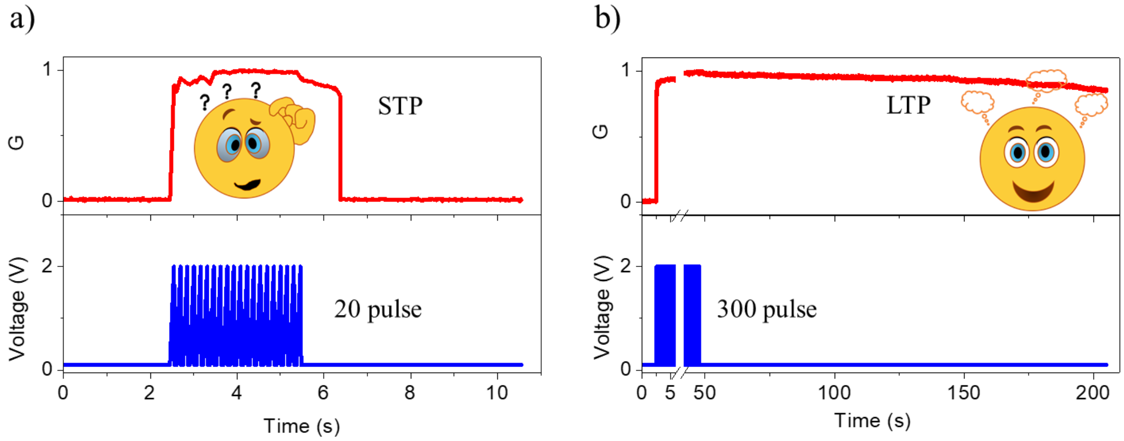

Figure IIIA.11: Rehearsal dependent STP to LTP transition. a) STP is emulated with 20 pulses while b) LTP is emulated with 300 pulses. Current compliance was set to 100 μA.

In addition, increasing the pulse number to 300 also resulted in prolonged stability of conductance above 200 s thus emulating LTP. Increasing the number of pulses is analogues to rehearsal of learning event as typically observed in biological system. Low current compliance results in the formation of thin, weak filaments which may be unstable and breakup easily leading to low conductance of the device, while a higher current compliance or large number of pulses produces thick stable filaments which can sustain for longer

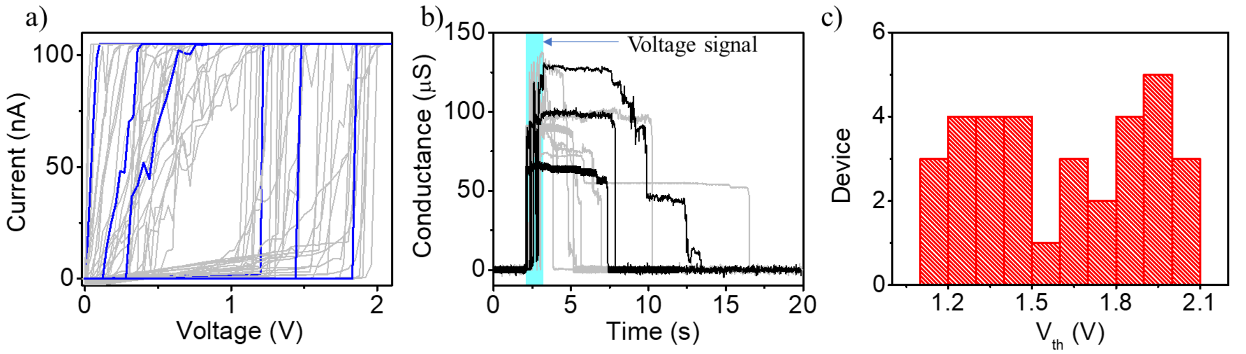

Figure IIIA.12: Device reproducibility. a) Resistive switching behaviour of over 30 devices is shown using the I-V characteristics. b) STP behaviour emulated in different devices using typical pulse signal (2 V ×20 pulse, 50 ms width and interval, 100 µA current compliance). c) Cumulative distribution of threshold switching voltage (V_{th}).

periods of time [24]. Thus, by controlling the current compliance or pulse number, STP and LTP can be readily realized in the designated Ag-ASN. Over 30 batches of samples were prepared for the fabrication of synaptic devices to validate the reproducibility. Figure IIIA.12 shows the I-V switching characteristics and STP behaviour of some of the devices. Notably, excellent device reproducibility was observed in terms of conductance switching and learning behavior.

Ambient stability of the device is also an important aspect in practical application. To investigate this, the device was stored in lab ambient condition for over a year and then

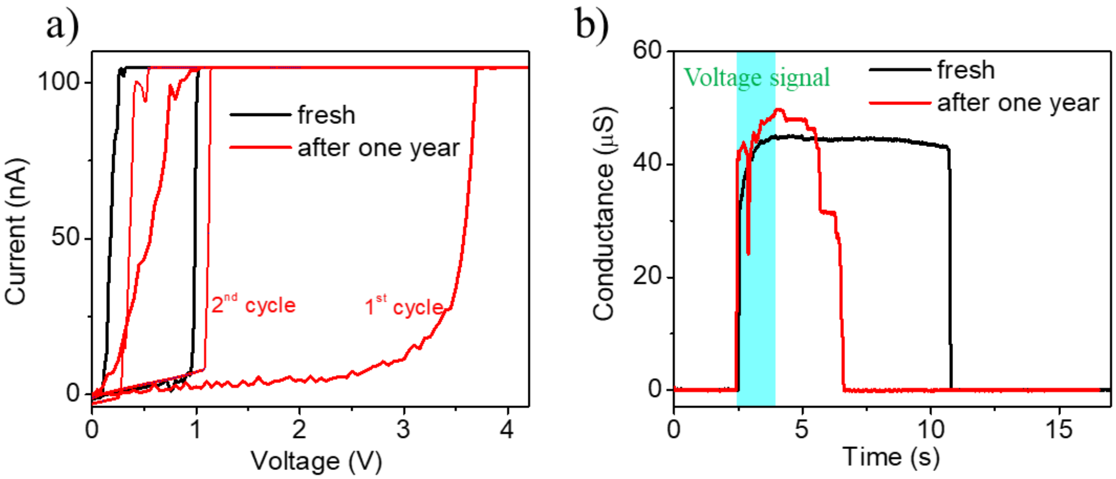

Figure IIIA.13: Device stability in ambient condition. a) I-V characteristics showing the switching nature of the device in fresh condition and stored in ambient for one year. b) STP behavior emulated in the aged device (2 V ×20 pulse, 50 ms width and interval, 100 µA current compliance).

subjected to electrical measurement. From Figure IIIA.13a, the device switching voltage was seen shifted to a higher value (1st cycle) possibly due to the mild surface oxidation. However, the device recovered to its pristine state during the subsequent I-V cycle (2nd cycle) which may be attributed to joule heating leading to decomposition of oxide formation [37]. In addition, STP nature was also emulated in the aged device thus showing good ambient stability (Figure IIIA.13b). Memory strength is also influenced by pulse/spike parameters such as width, frequency and number. The strength is seen to increase with each of these parameter (Figure IIIA.14). Further, important feature in learning is the potentiation and depression were also emulated using positive and negative stimulus as shown in Figure IIIA.15.

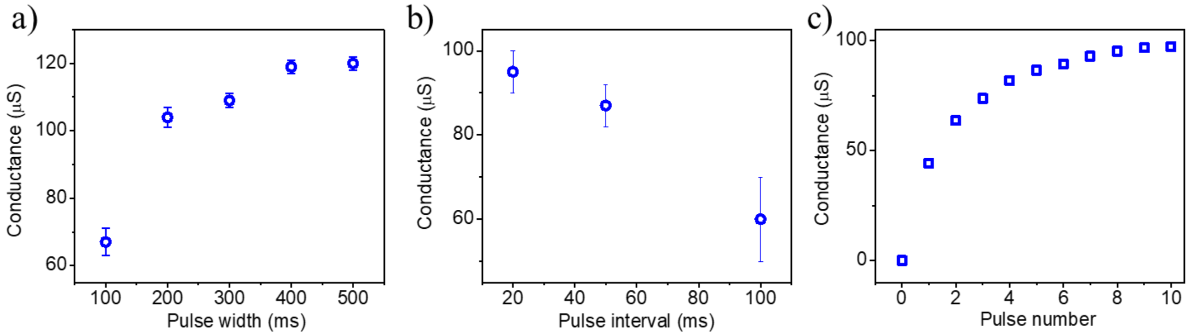

Figure IIIA.14: Conductance modulation with a) pulse width (single pulse with 2 V amplitude), b) pulse interval (20 x 2 V pulses with 50 ms width) and c) pulse number (2 V pulse with 50 ms width).

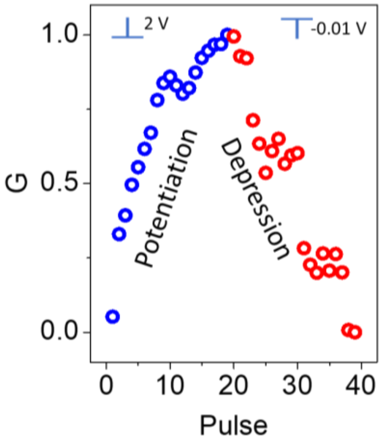

Figure IIIA.15: Potentiation and depression. 20 potentiation pulse and 20 depression pulse were applied to show the tunability of conductance. Pulse width was 50 ms.

Figure IIIA.16a shows an oversimplified schematic of the biological neural network. Neurons interact with each other in a complex network via junctions called synapse. Nanogap separation at this junction is known as synaptic cleft where the neurotransmitter gets released to form memory and cognition. Figure IIIA.16b,c shows the SEM image of the artificial synaptic network prepared by annealing Ag film. The resulting structure consists of a network of Ag agglomerates separated by nanogaps filled with isolated nanoparticles. This geometry resembles the biological neural network with agglomerates as neurons, nanogaps between the branched edges as synapses and nanoparticles as neurotransmitters. From the image analysis (Figure IIIA.17) the approximate neuron-like agglomerate density was found

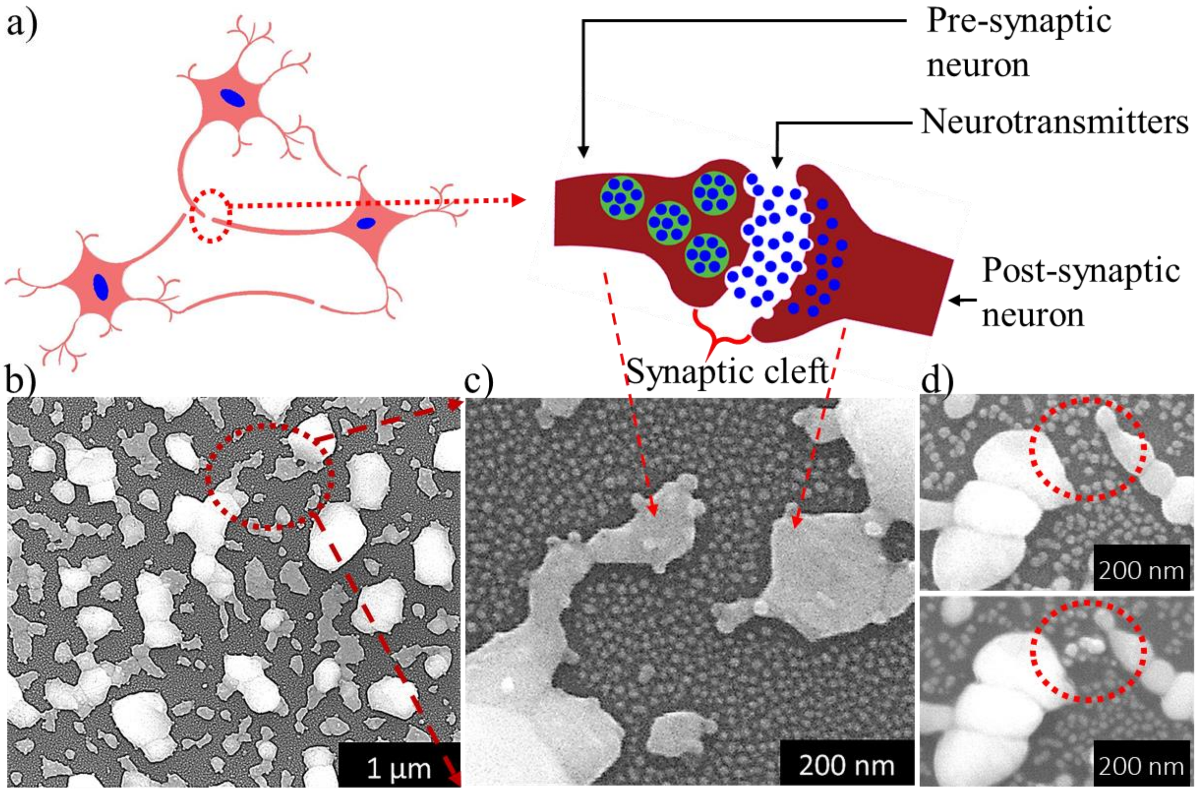

Figure IIIA.16: a) Schematic of the biological neural network. It is a collection of neurons and neurites having dendrites and axons. Neurons meet at the synaptic junction, the latter being the building block of memory and cognitive systems. Synapse is activated by releasing the neurotransmitter into the synaptic cleft in response to the input stimuli. Single synapse is shown in the right. b) SEM image of the artificial synaptic network resembling the biological counterpart. c) Magnified SEM image shows mimicking of biological synapse with small nanoparticles as neurotransmitters. d) Formation of conduction filament under applied field due to electromigration.

to be around 1.1 × 10^9 per square inches with several times higher synapse-like nanogaps thus making it highly suitable for high performance synaptic device. When the electric field is applied as a neural signal electromigration of Ag facilitates the filament formation in the nanogaps as shown in Figure IIIA. 16d, thus emulating the neurotransmitter-like dynamics at synapse.

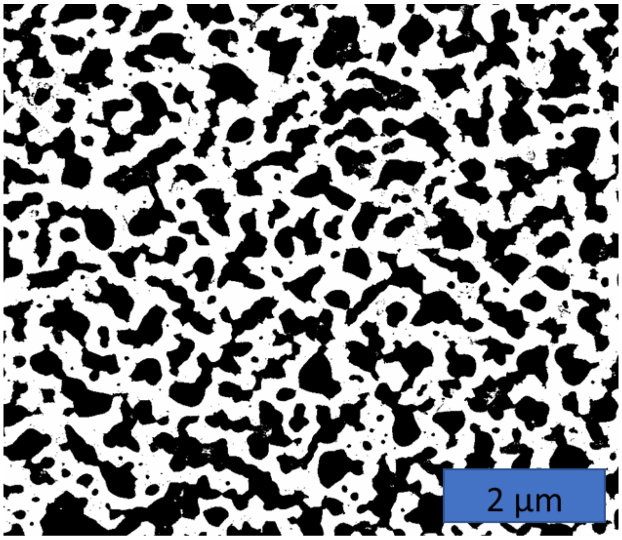

Figure IIIA.17: SEM image was analysed using ImageJ and average agglomerate density was found to be around 1.1 × 10^9 per square inch. Considering average 5 nanogap-like synapse per agglomerate, average synapse density will be 5.5 × 10^9 per square inch. Bio neural network has approximately 1.28 × 10^{13} synapses per cubic inch. Considering average size of a neuron, in-plane synapse density will be around ~10^9 per square inch.

IIIA.5 Conclusions

In conclusion, a novel structure that resemble bio neural network formed via simple fabrication process is proposed. The Ag islands with branched edges enabled controlled electromigration of metal atoms via voltage spiking and current control to form a variety of filamentous growths between the islands across the nanogaps as examined using microscopy techniques. The nanogaps filled with nanoparticles between the islands resemble the biological synapse. With voltage spikes representing the pre-synaptic signal, neuroplasticity such as STP, LTP, potentiation, depression, spike duration dependent plasticity (SDDP), spike rate dependent plasticity (SRDP) and spike number dependent plasticity (SNDP) were emulated. Several batches of devices were fabricated demonstrates the good reproducibility. Moreover, the device showed excellent ambient stability over a year.

References

[1] V. M. Ho, J. A. Lee, and K. C. Martin, *The Cell Biology of Synaptic Plasticity*, Science **334**, 623 (2011).

[2] A. Taherkhani, A. Belatreche, Y. Li, G. Cosma, L. P. Maguire, and T. M. McGinnity, *A Review of Learning in Biologically Plausible Spiking Neural Networks*, Neural Networks **122**, 253 (2020).

[3] S. H. Jo, T. Chang, I. Ebong, B. B. Bhadviya, P. Mazumder, and W. Lu, *Nanoscale Memristor Device as Synapse in Neuromorphic Systems*, Nano Lett. **10**, 1297 (2010).

[4] Q. Wan, M. T. Sharbati, J. R. Erickson, Y. Du, and F. Xiong, *Emerging Artificial Synaptic Devices for Neuromorphic Computing*, Adv. Mater. Technol. **4**, 1900037 (2019).

[5] M. Xiao, D. Shen, M. H. Futscher, B. Ehrler, K. P. Musselman, W. W. Duley, and Y. N. Zhou, *Threshold Switching in Single Metal-Oxide Nanobelt Devices Emulating an Artificial Nociceptor*, Adv. Electron. Mater. **6**, 1900595 (2020).

[6] P. Yao, H. Wu, B. Gao, S. B. Eryilmaz, X. Huang, W. Zhang, Q. Zhang, N. Deng, L. Shi, H. S. P. Wong, and H. Qian, *Face Classification Using Electronic Synapses*, Nat. Commun. **8**, 15199 (2017).

[7] S. B. Eryilmaz, D. Kuzum, R. Jeyasingh, S. B. Kim, M. BrightSky, C. Lam, and H. S. Philip Wong, *Brain-like Associative Learning Using a Nanoscale Non-Volatile Phase Change Synaptic Device Array*, Front. Neurosci. **8**, 205 (2014).

[8] L. F. Abbott and W. G. Regehr, *Synaptic Computation*, Nature **431**, 796 (2004).

[9] R. Yang, H. M. Huang, and X. Guo, *Memristive Synapses and Neurons for Bioinspired Computing*, Adv. Electron. Mater. **5**, 1900287 (2019).

[10] N. K. Upadhyay, H. Jiang, Z. Wang, S. Asapu, Q. Xia, and J. Joshua Yang, *Emerging Memory Devices for Neuromorphic Computing*, Adv. Mater. Technol. **4**, 1800589 (2019).

[11] J. Lisman, K. Cooper, M. Sehgal, and A. J. Silva, *Memory Formation Depends on Both Synapse-Specific Modifications of Synaptic Strength and Cell-Specific Increases in Excitability*, Nat. Neurosci. **21**, 309 (2018).

[12] J. Sun, Y. Fu, and Q. Wan, *Organic Synaptic Devices for Neuromorphic Systems*, J. Phys.

D. Appl. Phys. **51**, 314004 (2018).

[13] Y. Van De Burgt, A. Melianas, S. T. Keene, G. Malliaras, and A. Salleo, *Organic Electronics for Neuromorphic Computing*, Nat. Electron. **1**, 386 (2018).

[14] Y. Shi, X. Liang, B. Yuan, V. Chen, H. Li, F. Hui, Z. Yu, F. Yuan, E. Pop, H. S. P. Wong, and M. Lanza, *Electronic Synapses Made of Layered Two-Dimensional Materials*, Nat. Electron. **1**, 458 (2018).

[15] Z. Zhou, J. Zhao, A. P. Chen, Y. Pei, Z. Xiao, G. Wang, J. Chen, G. Fu, and X. Yan, *Designing Carbon Conductive Filament Memristor Devices for Memory and Electronic Synapse Applications*, Mater. Horiz. **7**, 1106 (2020).

[16] Y. Pei, Z. Zhou, A. P. Chen, J. CHEN, and X. Yan, *A Carbon Based Memristors Design for Associative Learning Activities and Neuromorphic Computing*, Nanoscale **12**, 13531 (2020).

[17] A. Wedig, M. Luebben, D. Y. Cho, M. Moors, K. Skaja, V. Rana, T. Hasegawa, K. K. Adepalli, B. Yildiz, R. Waser, and I. Valov, *Nanoscale Cation Motion in* TaO_x*,* HfO_x *and* TiO_x *Memristive Systems*, Nat. Nanotechnol. **11**, 67 (2016).

[18] J. Zhu, T. Zhang, Y. Yang, and R. Huang, *A Comprehensive Review on Emerging Artificial Neuromorphic Devices*, Appl. Phys. Rev. **7**, 011312 (2020).

[19] G. Milano, M. Luebben, Z. Ma, R. Dunin-Borkowski, L. Boarino, C. F. Pirri, R. Waser, C. Ricciardi, and I. Valov, *Self-Limited Single Nanowire Systems Combining All-in-One Memristive and Neuromorphic Functionalities*, Nat. Commun. **9**, 5151 (2018).

[20] J. Li, Y. Yang, M. Yin, X. Sun, L. Li, and R. Huang, *Electrochemical and Thermodynamic Processes of Metal Nanoclusters Enabled Biorealistic Synapses and Leaky-Integrate-and-Fire Neurons*, Mater. Horiz. **7**, 71 (2020).

[21] T. Y. Wang, J. L. Meng, Z. Y. He, L. Chen, H. Zhu, Q. Q. Sun, S. J. Ding, P. Zhou, and D. W. Zhang, *Room-Temperature Developed Flexible Biomemristor with Ultralow Switching Voltage for Array Learning*, Nanoscale **12**, 9116 (2020).

[22] S. H. Sung, D. H. Kim, T. J. Kim, I. S. Kang, and K. J. Lee, *Unconventional Inorganic-Based Memristive Devices for Advanced Intelligent Systems*, Adv. Mater. Technol. **4**, 1900080 (2019).

[23] T. Ohno, T. Hasegawa, T. Tsuruoka, K. Terabe, J. K. Gimzewski, and M. Aono, *Short-Term Plasticity and Long-Term Potentiation Mimicked in Single Inorganic Synapses*, Nat.

Mater. **10**, 591 (2011).

[24] S. La Barbera, D. Vuillaume, and F. Alibart, *Filamentary Switching: Synaptic Plasticity through Device Volatility*, ACS Nano **9**, 941 (2015).

[25] C. Lutz, T. Hasegawa, and T. Chikyow, *Ag2S Atomic Switch-Based "tug of War" for Decision Making*, Nanoscale **8**, 14031 (2016).

[26] Z. Wang, S. Joshi, S. E. Savel'ev, H. Jiang, R. Midya, P. Lin, M. Hu, N. Ge, J. P. Strachan, Z. Li, Q. Wu, M. Barnell, G. L. Li, H. L. Xin, R. S. Williams, Q. Xia, and J. J. Yang, *Memristors with Diffusive Dynamics as Synaptic Emulators for Neuromorphic Computing*, Nat. Mater. **16**, 101 (2017).

[27] E. Li, W. Lin, Y. Yan, H. Yang, X. Wang, Q. Chen, D. X. Lv, G. Chen, H. Chen, and T. Guo, *Synaptic Transistor Capable of Accelerated Learning Induced by Temperature-Facilitated Modulation of Synaptic Plasticity*, ACS Appl. Mater. Interfaces **11**, 46008 (2019).

[28] S. Gao, G. Liu, H. Yang, C. Hu, Q. Chen, G. Gong, W. Xue, X. Yi, J. Shang, and R. W. Li, *An Oxide Schottky Junction Artificial Optoelectronic Synapse*, ACS Nano **13**, 2634 (2019).

[29] M. Xiao, T. Yeow, V. H. Nguyen, D. Muñoz-Rojas, K. P. Musselman, W. W. Duley, and Y. N. Zhou, *Ultrathin TiOx Interface-Mediated ZnO-Nanowire Memristive Devices Emulating Synaptic Behaviors*, Adv. Electron. Mater. **5**, 1900142 (2019).

[30] S. Wang, C. Chen, Z. Yu, Y. He, X. Chen, Q. Wan, Y. Shi, D. W. Zhang, H. Zhou, X. Wang, and P. Zhou, *A MoS2/PTCDA Hybrid Heterojunction Synapse with Efficient Photoelectric Dual Modulation and Versatility*, Adv. Mater. **31**, 1806227 (2019).

[31] X. Yan, Y. Pei, H. Chen, J. Zhao, Z. Zhou, H. Wang, L. Zhang, J. Wang, X. Li, C. Qin, G. Wang, Z. Xiao, Q. Zhao, K. Wang, H. Li, D. Ren, Q. Liu, H. Zhou, J. Chen, and P. Zhou, *Self-Assembled Networked PbS Distribution Quantum Dots for Resistive Switching and Artificial Synapse Performance Boost of Memristors*, Adv. Mater. **31**, 1805284 (2019).

[32] J. Zhou, C. Wan, L. Zhu, Y. Shi, and Q. Wan, *Synaptic Behaviors Mimicked in Flexible Oxide-Based Transistors on Plastic Substrates*, IEEE Electron Device Lett. **34**, 1433 (2013).

[33] S. G. Hu, Y. Liu, T. P. Chen, Z. Liu, Q. Yu, L. J. Deng, Y. Yin, and S. Hosaka, *Emulating the Ebbinghaus Forgetting Curve of the Human Brain with a NiO-Based Memristor*, Appl. Phys. Lett. **103**, 133701 (2013).

[34] C. Wu, T. W. Kim, T. Guo, F. Li, D. U. Lee, and J. J. Yang, *Mimicking Classical Conditioning Based on a Single Flexible Memristor*, Adv. Mater. **29**, 1602890 (2017).

[35] R. A. John, F. Liu, N. A. Chien, M. R. Kulkarni, C. Zhu, Q. Fu, A. Basu, Z. Liu, and N. Mathews, *Synergistic Gating of Electro-Iono-Photoactive 2D Chalcogenide Neuristors: Coexistence of Hebbian and Homeostatic Synaptic Metaplasticity*, Adv. Mater. **30**, 1800220 (2018).

[36] S. G. Hu, Y. Liu, Z. Liu, T. P. Chen, Q. Yu, L. J. Deng, Y. Yin, and S. Hosaka, *Synaptic Long-Term Potentiation Realized in Pavlov's Dog Model Based on a NiOx-Based Memristor*, J. Appl. Phys. **116**, 214502 (2014).

[37] X. Y. Gao, S. Y. Wang, J. Li, Y. X. Zheng, R. J. Zhang, P. Zhou, Y. M. Yang, and L. Y. Chen, *Study of Structure and Optical Properties of Silver Oxide Films by Ellipsometry, XRD and XPS Methods*, Thin Solid Films **455**, 438 (2004).

Chapter IIIB

Higher-Order Learning in an Artificial Synaptic Network *

Summary

With the interesting device architecture, i.e. artificial synaptic network, resembling the bio counterpart, and carefully designed voltage pulse configuration, several higher order synaptic activities were emulated, importantly, without the aid of external CMOS or equivalent circuitry. Behaviors close to human psychology such as first and second order associative learning, supervision, impression of supervision and interest-based learning were realized. A prototype kit developed to emulate Pavlov's dog behavior clearly demonstrates the potential of the device towards neuromorphic artificial intelligence.

IIIB.1 Introduction

As discussed earlier, the brain-inspired synaptic devices are promising circuit elements for neuromorphic artificial intelligence. Although wide variety of materials have been explored to fabricate synaptic devices, their functions are often limited to STP, LTP and SPDP [1-3]. Mimicking higher level cognitive actions in device is highly challenging but at the same time is very essential requirement for accomplishing effective brain-inspired computing.

One of many components of intelligence is associative learning, often typified by Pavlov's dog. Here, a stimulus that generates an obvious response, is associated to a neutral stimulus through repeat learning cycles, such that post association, the neutral stimulus alone will be able to generate the anticipated response. There are limited reports on devices which clearly emulate such a complex learning behavior [4, 5]. Yang et al.,[4] demonstrated classical conditioning in Al_2O_3/PI based flexible device while compromising the reset ability of the device. Mathews et al.,[5] utilized multigated MoS_2 transistor with threshold current concept to mimic the same. In many cases, CMOS hardware integration was adopted to demonstrate the behavior [6-8]. Moreover, these devices are limited to first order association while human brain does exhibit higher order association capability. Recently, more human-like interest-based learning in an optoelectronic synapse and sleep-wake-cycle in an electronic synapse have also been realized using a variety of active materials and configurations [9,10].

---

*Part of this Chapter is from: Mater.Horiz., **7**, 2970 (2020).

Although, few reports deal with mimicking advanced behavioral patterns, the material system employed for the purpose are highly varied often accompanying supporting circuits or software-based platforms. A table presented here compares the behavioral performance of multi-terminal devices from the literature. For an effective brain inspired neuromorphic artificial intelligence or on-synapse artificial intelligence, the main challenge is to emulate all these cognitive actions in a given material system without the aid of external circuits, thus saving on energy and speed.

IIIB.2 Scope of the present investigation

In literature, several organic and inorganic materials have been explored to fabricate synaptic devices which emulate STP, LTP and SPDP. Although these devices were able to mimic the aforementioned basic synaptic actions, emulating neuromorphic artificial intelligence with these alone is nowhere near. For an effective brain-inspired artificial intelligence, it is crucial to emulate higher level cognitive functions. This chapter proposes an innovative approach to emulate higher order learning in the ASN device. Reading voltage is often used for measuring the state of the device during and after pulsing. In this study, reading voltage is also used as modulatory signal and optimized to emulate supervision as well as interest-based learning. While increasing reading voltage was exploited to emulate supervision behaviour, withdrawing reading voltage in step and gradual manner mimicked impression of supervision. Further, higher reading voltages were used to create interest-based learning. By carefully configuring pulse signals, first and second order classical conditioning were also demonstrated. Interestingly, all these synaptic actions were emulated in a single material system without the aid of any CMOS circuits. A plug-and-play kit emulating Pavlov’s dog behavior has been developed for ready demonstration of the capability of the synaptic device.

IIIB.3 Experimental details

Customized pulse signal configuration was achieved by exploiting the voltage list sweep mode in Keithley 2450. Gradual withdrawal of the voltage is performed by keeping the same withdrawal rate for all voltage levels.

IIIB.4 Results and discussion

To explore the higher order learning capability of the device, a few behavior patterns have been tried out, viz behavior under supervision, interest-based learning and associative learning. The first case may be taken to relate to a real scenario wherein a fickle-minded junior, being supervised by a senior, may perform well only under strong supervision.

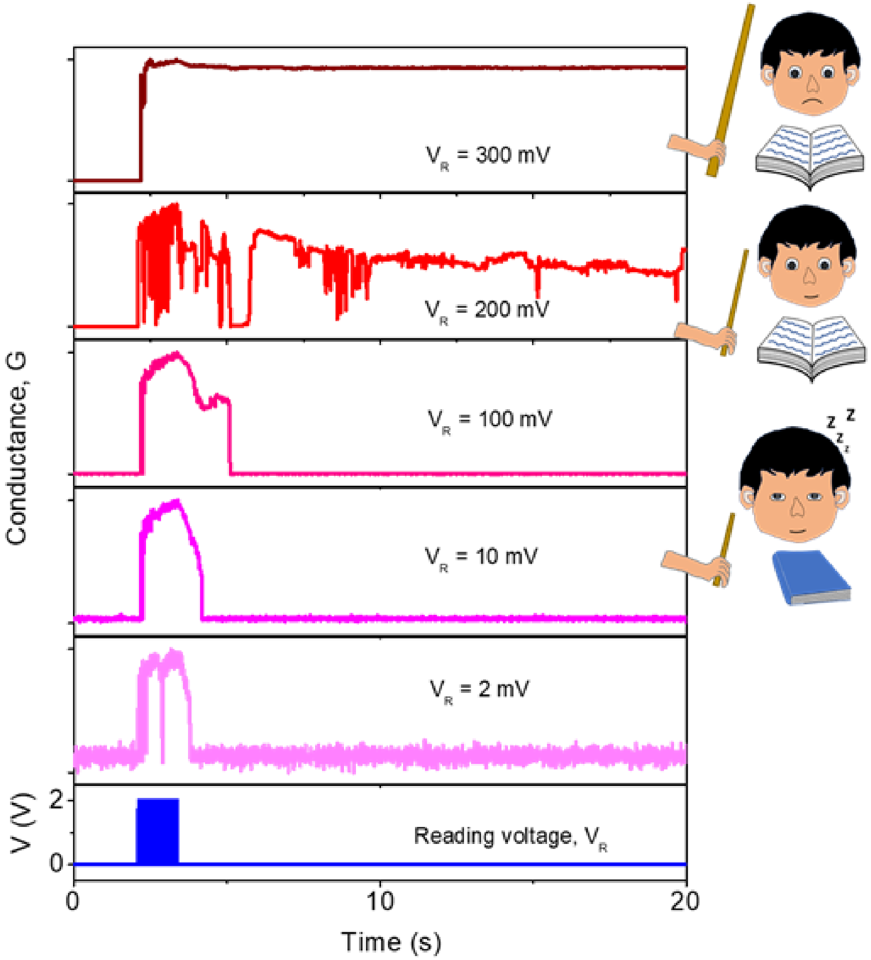

Figure IIIB.1: Behavior under supervision. Reading voltage was increased to represent different supervising strength. Improved conductance retention represents the increased attentiveness.

Working with the device, 2V pulse sequence was assigned as the task given, the conductive state to represent the junior's behavior (higher the conductance, better is the behavior) and the reading voltage applied (2 to 300 mV) to the strength of the supervision. Under mild supervision (2 mV), the (conductance state) retention was only for a fraction of a second (~ 0.2 s) and then it decayed to its initial value (see Figure IIIB.1). When the supervisory reading voltage was increased to 10 mV and then to 100 mV, the junior's retention increased but not beyond 2 s. When a moderate supervision of 200 mV was applied, the performance was somewhat better but there were several random attempts to escape to the original low conductance state. However, under strict supervision (300 mV), a consistent retention was seen all through. From the behavioral pattern summarized in Figure IIIB.2, one can see that under low supervision strength (2 to 100 mV), the device conductance was often limited to lower values, implying a tendency to be generally lazy, while under moderate level supervision (200 mV), an increased conductance (attentiveness) was observed with intermittent lazy intervals. A supervision with 300 mV produced a stable conductance state attributable to full attentiveness. Increase in reading voltage is expected to increase the Coulombic attraction, thereby increasing the filament stability and thus its retention.

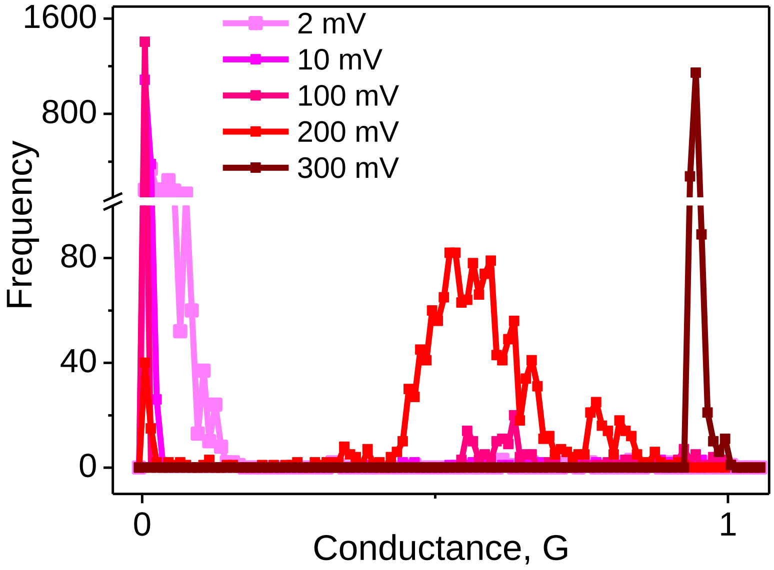

Figure IIIB.2: Distribution of conductance for different supervising voltages. Frequency here represents the instances (counts) of achieved conductance value (junior's behavior) attained by the device after pulse signal or during the supervision voltage. During low supervision voltages (2-100 mV), maximum (peak) count is appearing at low conductance value suggesting that the junior tends to be lazy while under strict supervision (300 mV), the count is maximum for high conductance value representing full attentiveness. However, during moderate supervision (200 mV), there are two peaks at both high and low conductance values suggesting intermittent attentiveness.

Further the study was advanced to examine the effect of withdrawal of supervision to a lower level for a short duration before resetting back to the original level. In real scenario, there are occasions where the supervision is withdrawn either abruptly attending to an emerging requirement or gradually so as to leave behind just an impression of supervision. In the first case of abrupt removal of supervision, the junior may relax back to the original behavior after a little while, but with the gradual 'unnoticed' removal of supervision, the junior meticulously continues to remain in the attained state, just under the impression of senior's

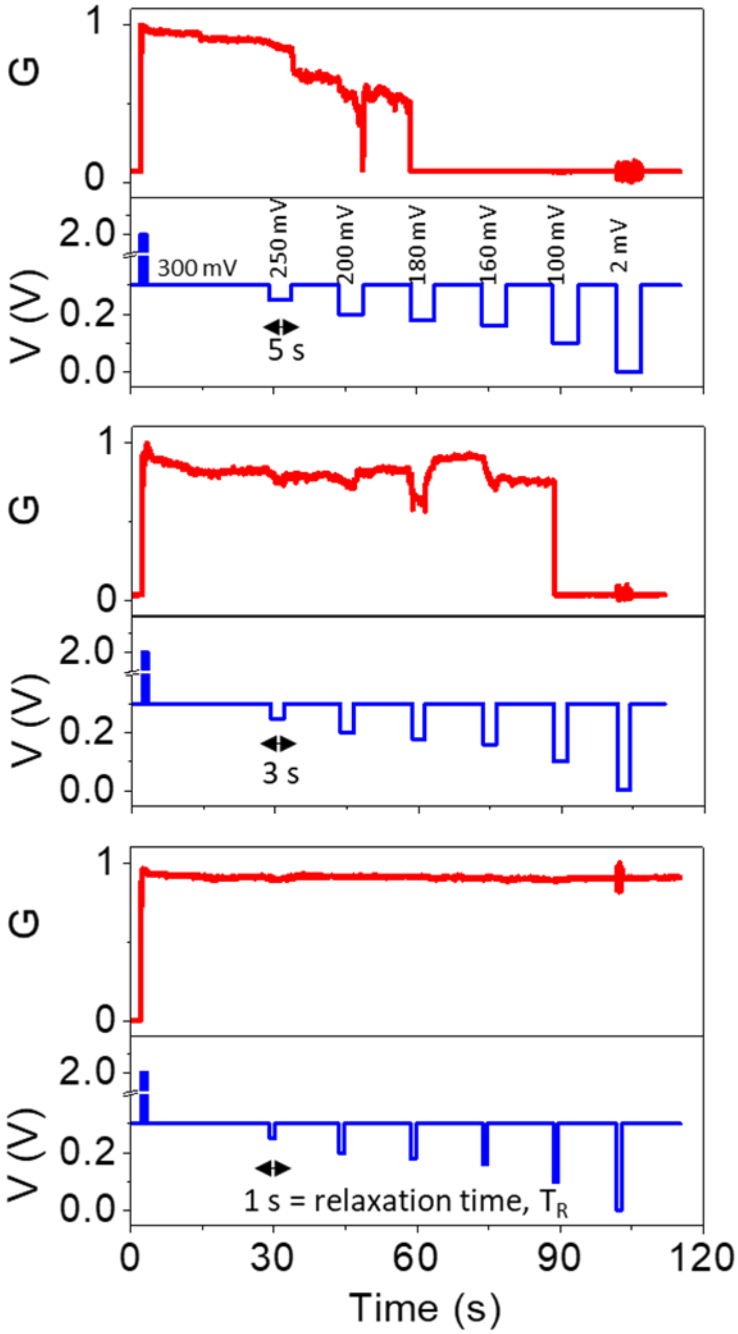

Figure IIIB.3: Withdrawing the supervision to different levels for 1 s, 3 s, 5 s relaxation time.

presence. A common example of the latter case is of a child that often thinks that the mother is always nearby even when she slowly slips away to attend to some work. To mimic both scenarios, the device was first subjected to strict supervision (300 mV) and it was then withdrawn momentarily (T_R) to lower levels (250 to 2 mV) as shown in Figure IIIB.3. When the supervision was withdrawn for 1 s T_R, the conductance (behavior) was unperturbed even during and after the lowest supervision strength of 2 mV. Similar behavior was observed for 2 s T_R. But when T_R was prolonged to 3 s or beyond, the conductance showed minor instability at each withdrawal and finally dropped to initial state even under moderate supervision strength (i.e. in case of T_R of 5 s, the conductance drop was at 180 mV). As shown in the histogram in Figure IIIB.4, these refer to cases when the supervision was withdrawn suddenly by a step change in the voltage value. A gradual change of supervision is emulated by gradually withdrawing the voltage at a defined rate. We choose highest T_R (5 s) for this case. When the supervision was withdrawn gradually at a rate of 60 mV/s, the device conductance dropped to the initial state on reaching the lowest supervision strength of 2 mV (see inset, Figure IIIB.5). Remarkably, the supervision withdrawal was ‘unnoticed’ when withdrawal was performed at a slow rate of 10 mV/s as shown in Figure IIIB.5. This rate-dependent retention of conductance is mainly attributed to the device architecture. In the Ag-ASN device, filaments are formed between the metal islands in response to the applied electric field. This system is expected to be associated with parasitic capacitance. During the step-change/higher withdrawal rate in the electric field, the polarity reversal of the electric

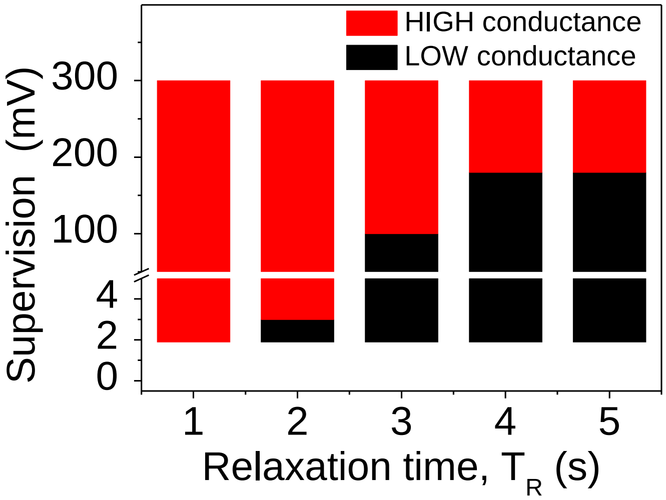

Figure IIIB.4: Histogram representing the stability of the conduction state for different withdrawing voltages.

field due to the capacitance effect may act as a reset voltage and thus disrupt the filament. Whereas at a very low withdrawal rate (10 mV/s), smoother decay is expected as the filaments remain undisturbed.

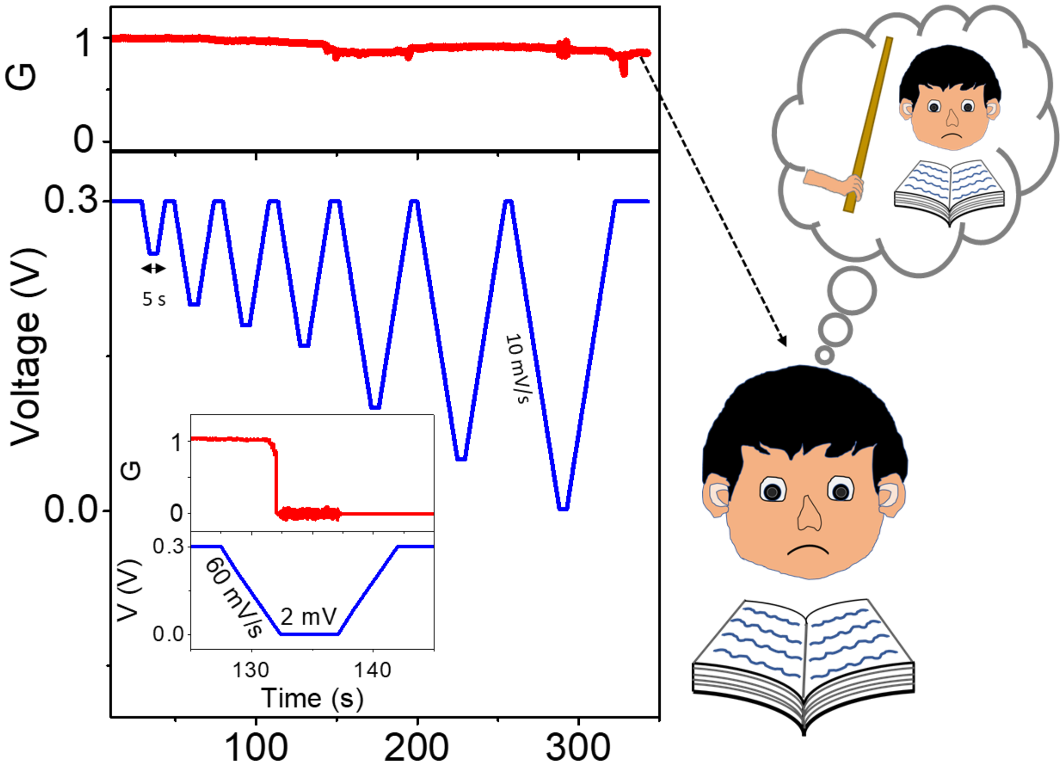

Figure IIIB.5: Impression of supervision. Stable conduction state for slow rate (10 mV/s) of withdrawal (inset: 60 mV/s withdrawal rate). Pulse sequence is omitted for clarity.

While the above examples pertain to unmotivated states, an interest-based activity does not warrant supervision at any level! Thus, interest-based learning or memory is an important process in biological systems. The retention of such memory depends on the interest expressed during the learning process. A deep interest should lead to a stronger memory thereby leading to its long retention that can be recollected over a period of time while a poor interest with short retention would make the memory decay immediately. To emulate this behavior in the device, we define two reading voltages; the reading voltage applied in the background during and after the pulse sequence to represent the strength of the interest expressed and the one after a 10 s gap to represent the recollection ability. The former was varied in the range, 300 – 500 mV, to represent varying interest strengths, while the second mild reading voltage of 100 mV represented the recollection process (Figure IIIB.6a). Figure

IIIB.6b shows the response of the device for 300 mV which stands for a lower degree of interest. It is evident that the device which switched to a high conducting state during the pulse sequence (indicating the memory formation), dropped itself to the non-conducting state after a 10 s gap when recollection using 100 mV was attempted. When the interest strength was set to 400 mV (moderate interest), the device continued to recollect the memory up to ~ 160 s as shown in Figure IIIB.6c. Finally, with high interest strength (500 mV), the memory recollection was excellent and it was up to ~ 2800 s (Figure IIIB.6d). Thus,

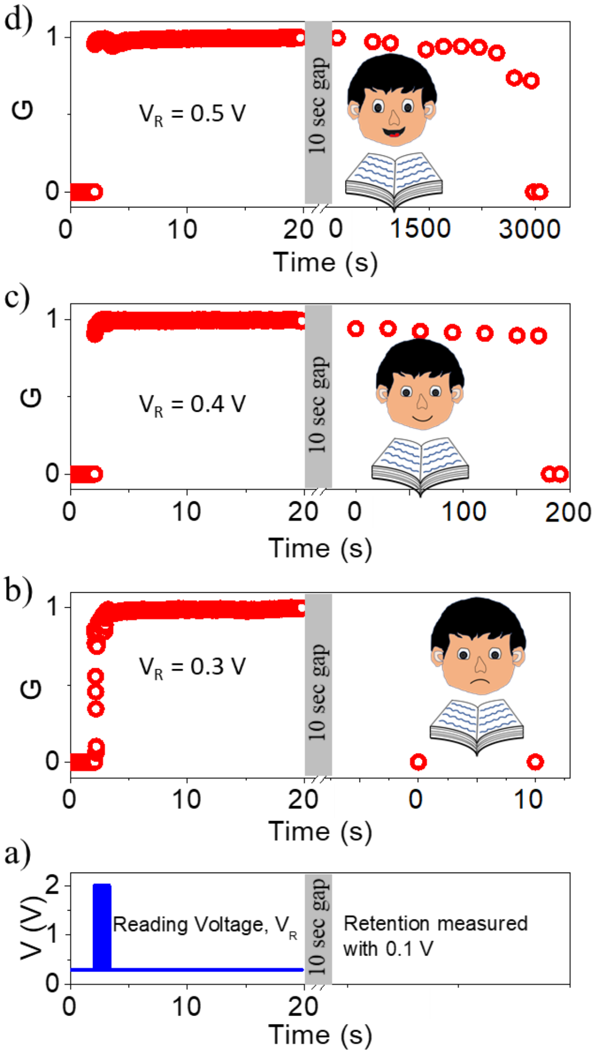

Figure IIIB.6: Emulation of interest-based learning/memory. a) Bottom panel represents the applied pulse sequence. Different reading voltages indicate the interest levels. b) 0.3 V represents the low interest c) 0.4 V represents the moderate interest d) 0.5 V represents the high interest. After the pulse signal, a time gap of 10 s is given and the memory retention is measured with a mild reading voltage of 0.1 V.

interest modulation is achieved by varying the reading voltage in the pulse sequence. Here, the voltage pulse facilitates the filament formation while the reading voltage stabilizes it. A higher reading voltage leads to stabler filaments and thereby, longer retention.

One of the complex learning processes observed in the brain is associative learning. Pavlov's dog [11] is a famous example of associative learning and the same experiment is commonly performed to emulate this classical conditioning in electronic synapse. On feeding, the dog responds by salivating while an unconnected event such as the ring of a bell does not produce any response. A training process is then initiated by feeding the dog while ringing the bell. The dog salivates on noticing the food but begins to associate the bell ring with food. In a

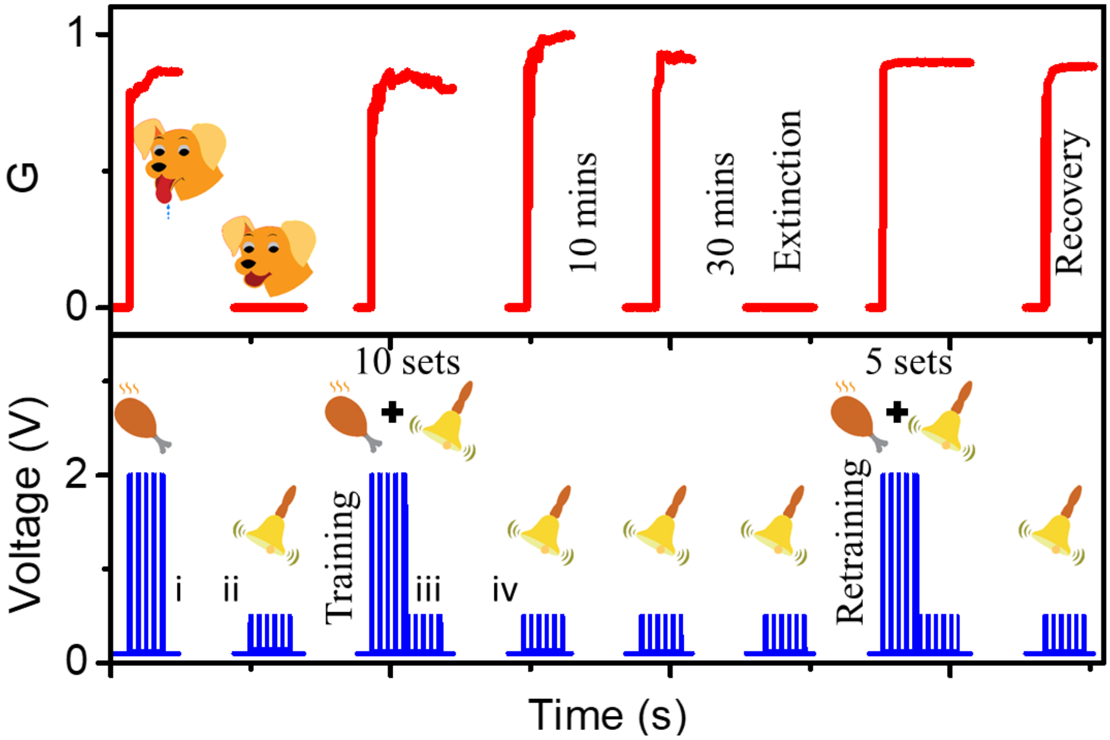

Figure IIIB.7: Pavlov's dog experiment. Food (20 pulses of 2 V with 50 ms width as well as interval) and bell (20 pulses of 0.5 V with 50 ms width as well as interval) signals were fed to the device and response was noted using 100 mV reading voltage. Device respond to the food signal but not to the bell signal. During training, food and bell (10 sets) signals were fed simultaneously. Now the device associates bell with food and starts responding for the bell signal alone and has a retention up to 30 mins where the extinction occurs. Now rehearsal is performed with lower number of training sets (5 sets) and the behavior is recovered. Current compliance is set to 100 μA.

following instance of bell ringing without providing food, the dog begins to salivate purely because of the association created during training. To emulate this behavior in the synaptic device, 20 x 2 V pulses was assigned to food and 20 x 0.5 V to the bell as shown in Figure IIIB.7. From the figure, we see that the food signal put the device into a high conducting state (salivation) while the bell signal did not induce any response since the assigned voltage is below the switching threshold. A training sequence towards associative learning was then imparted by applying the food and bell pulse sequences in immediate succession (training) for 10 sets. The device which switched to high conducting state (salivating) responding to the first set continued to remain salivating even after the 10th set, which is rather expected. However, when the bell pulse sequence alone was applied, amazingly, the device responded

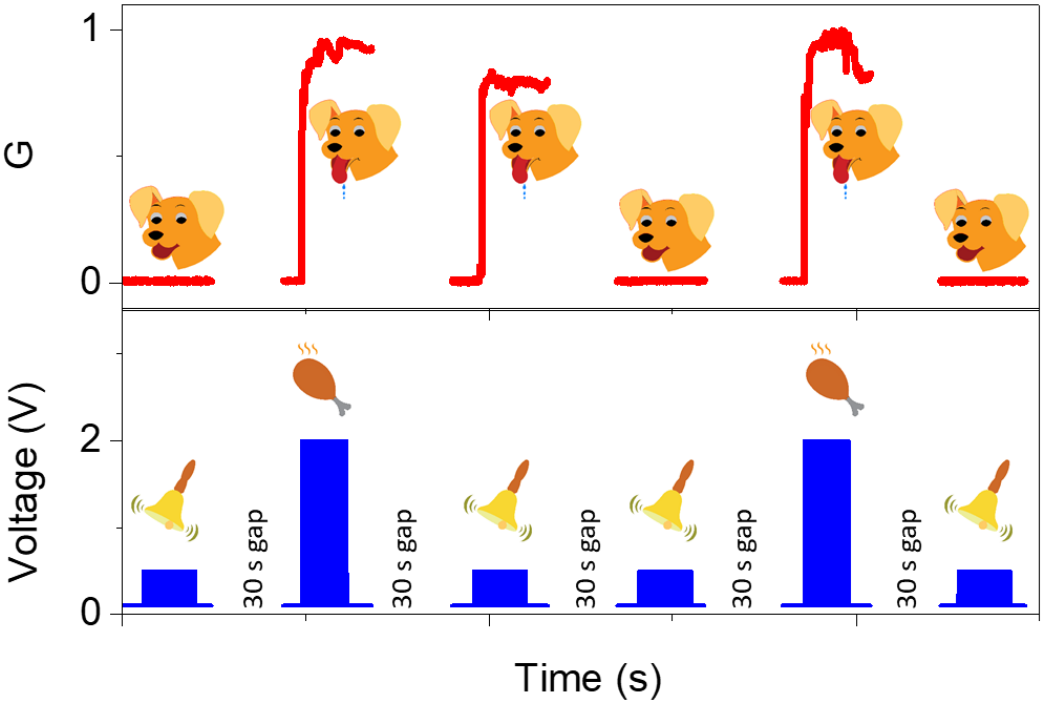

Figure IIIB.8: Dissociation of the classical conditioning. Here, after the extinction, the device did not respond to the bell signal. The food signal was then applied without the bell signal and the device responded. Because of the previous association, the device could respond to the immediate bell signal but not to the latter signals as this behavior decayed. However, the device continued to respond to the food signal without the bell signal. As there was no association between the food and bell signals, interestingly, the device did not respond to the following bell signal (illustrating complete dissociation).

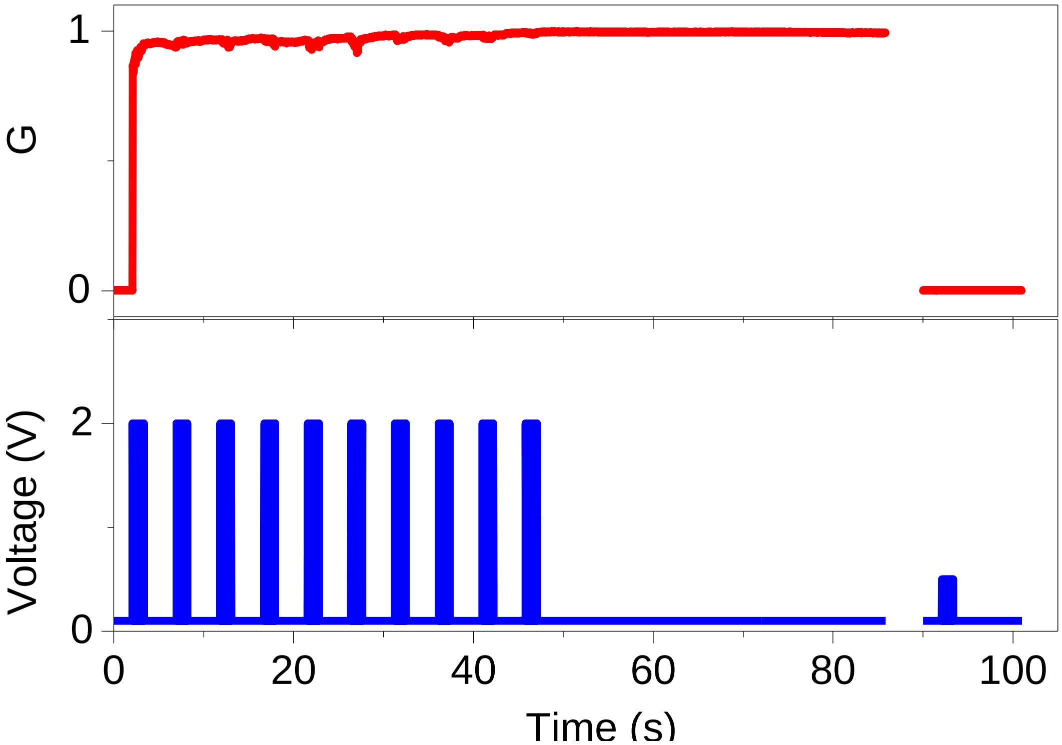

Figure IIIB.9: Only food pulse is applied for 10 cycles without bell pulse. The device showed response for the food. Now a bell pulse is applied to check whether the device will respond due to previous large number of food cycle. But it can be seen that the device did not respond to the bell pulse. This clearly shows that food must be accompanied with bell pulse to create association.

implying its associative learning ability, which in the present case, relates to bell with the food. This association was strong enough to retain up to ~ 30 mins after which an extinction was observed with the device no longer responding to the bell. Here, since the bell signal alone was applied to observe the retention of association, the absence of reward system leads to dissociation of the bell signal from the food signal, which is commonly observed in psychological behavior. The dissociation behavior is clearly shown in Figure IIIB.8. Here one may note that after extinction when the food (reward) signal was applied followed by the bell signal, device responded showing the optimistic thinking nature in expecting the reward. Also, repeating the same signal sequence did not result in salivation which is rather expected due to the previous disappointment. To recover the association, the device was subjected to a retraining process and interestingly, a lower number of food-bell training sets (5) was found enough this time. This is consistent with the general fact that relearning after forgetting is easier than virgin learning. In the device, the presence of residual filament traces leading to preferential path [12] may facilitate easier relearning. This way, the residual filament traces represent the residual calcium ions present in the post-synapses in a bio-neural system. The device readily responded to the bell signal showing a recovery. Many other signalling conditions were tried out to ensure the true associative learning ability of the device. It is crucial to confirm that application of large food signal alone does not create the anticipated associative response. In order to investigate this, 10 set of food signal alone was applied to the device followed by bell signal as shown in Figure IIIB.9. It is clear from the figure that the food signal alone is not able to generate the anticipated association typically obtained with the food-bell sequence. In addition, a large time-gap between the food and the bell signals during the training is also not expected to build the association since it acts as two isolated events. Figure IIIB.10 shows that when the food and bell signals were separated by 60 s, no association was created.

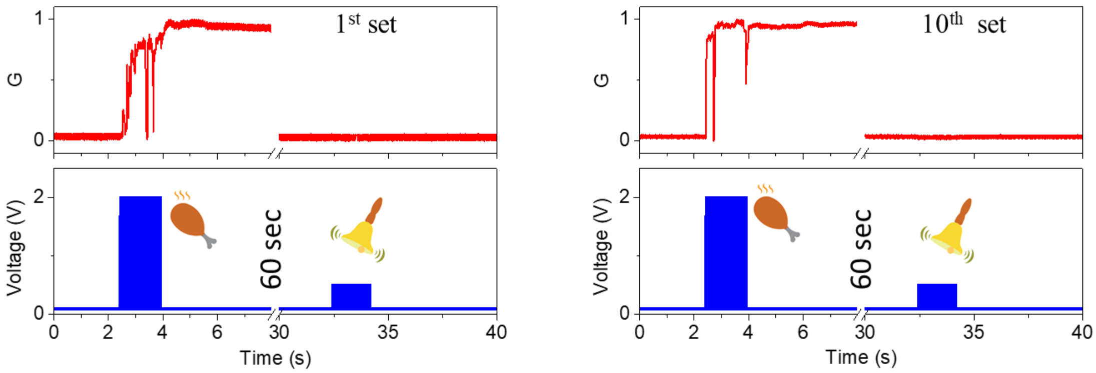

Figure IIIB.10: Large gap between food and bell signals will not be able to create the association. Here the food and bell signals were applied with a large gap of 60 sec. Even after 10 sets of such pulse sequence, the device shows no response to the bell signal displaying no association.

While the association response is at the verge of extinction, a higher intensity of neutral stimulus may cause the anticipated association response, often encountered in real scenario. Referring to the Pavlov's dog example, when the bell signal is about to go extinct, applying a louder bell is expected to invoke the response for that moment. To investigate this, 0.7 V pulse amplitude is selected as louder bell which by itself was not able produce any response. Figure IIIB.11 shows the typical association between food and bell for 10 set of training sequence. Typical dissociation was seen for successive bell signals and when it was about to

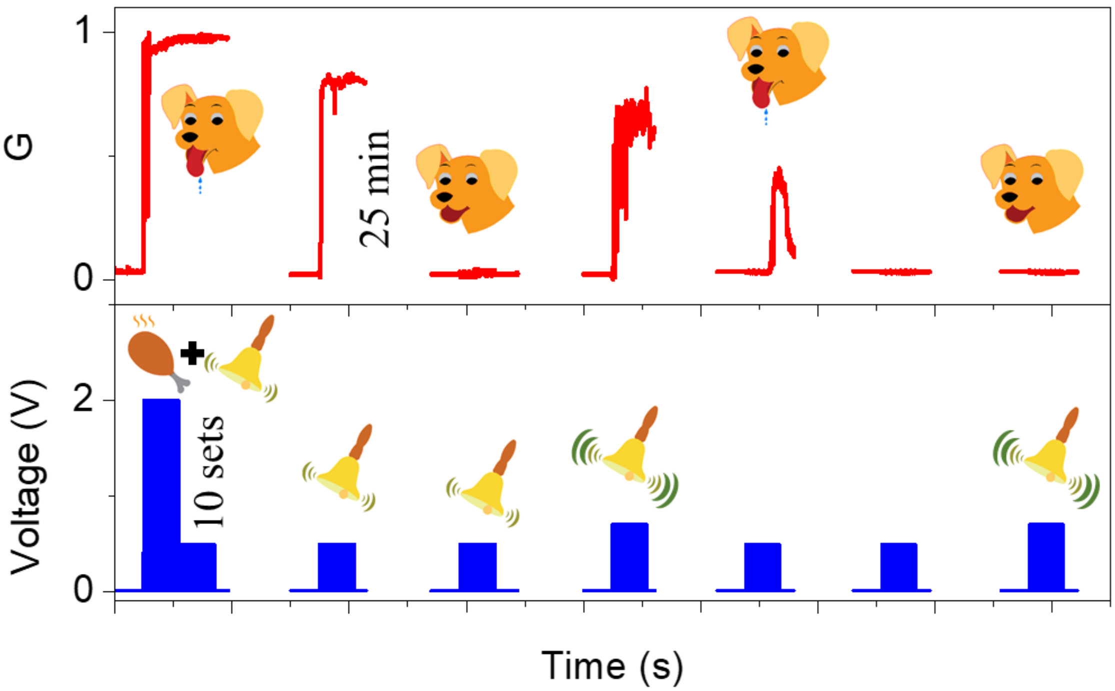

Figure IIIB.11: Response for louder bell. While extinction of association, a louder bell invokes the association. The set current compliance was 100 μA.

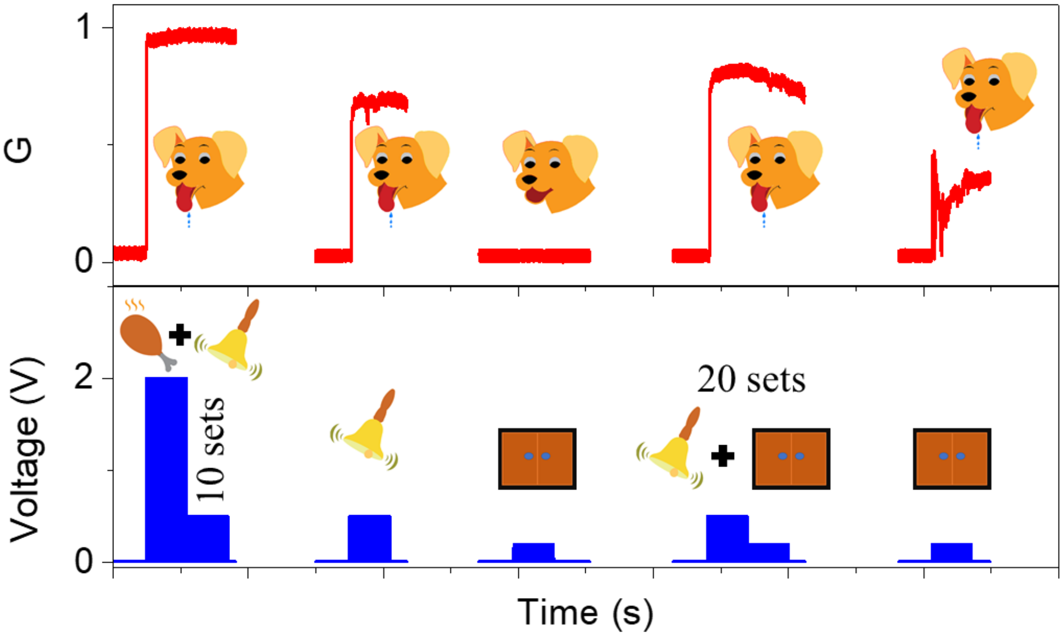

Figure IIIB.12: Second order association. Food (2 V) and bell (0.5 V) signals are associated in a typical manner and then the association of bell signal with the sound of the cabinet door (0.2 V) was established successfully.

extinct, louder bell signal was applied. Interestingly, the device responded to the louder bell as well as normal bell. However, due to the lack of reward system, extinction was seen for the following louder bell which is rather expected.

The human brain generally seen to exhibit higher cognitive ability. One of them is the higher order associative learning. For example, a person's name, his/her physical appearance and voice are generally highly associated; referring to one leads to invoking other traits. While the above measurement was pertaining to first order associative learning, the device can also be subjected to second order associative learning activity. This time three signals were chosen to represent different input stimuli. Extending the previous measurement, in Figure IIIB.12, 2 V and 0.5 V represent food and bell, while 0.2 V was chosen to represent the sound associated with the opening of the cabinet door where the bell is kept, as a real-world example. A reading voltage of 10 mV was chosen in order to avoid its influence on the latter signal. Food and bell were associated in usual manner as discussed previously. Post successful association, the bell signal was associated to cabinet door sound signal using a training sequence. Excitingly, the device responded to cabinet door signal showing a concrete second order association. In order to validate the true second order association, 10 set of bell (0.5 V) pulse alone was applied followed by inspection with the cabinet door (0.2

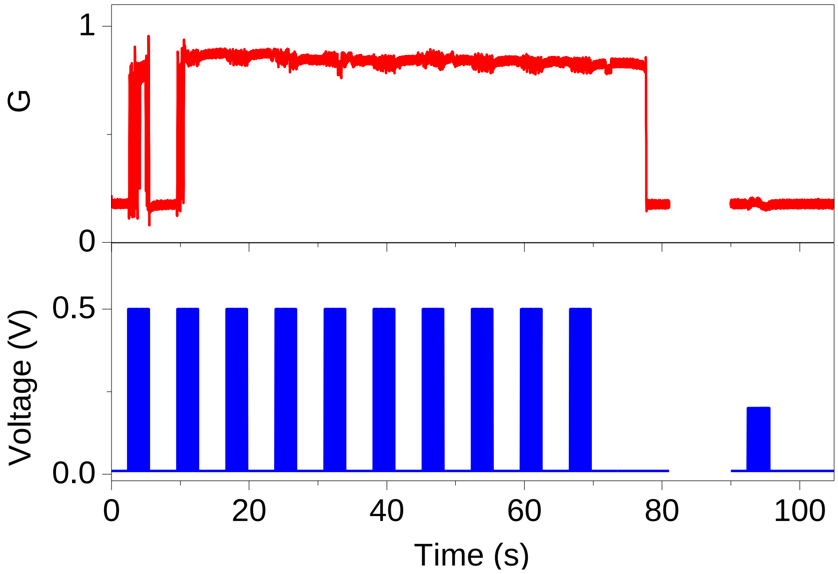

Figure IIIB.13: In order to authenticate the true association, large bell pulse was applied after successful first order association. When probed with cabinet door signal, no response was observed due to the absence of training.

V) signal. Figure IIIB.13 shows that the device did not show second order association only for bell signal thus ensuring the true association.

The stability of the filaments is governed by the pulse configuration and reading voltage there by leading to the different synaptic activities as discussed. In short term dynamics, stability of the weak filaments is influenced by the reading voltage. As the electric field becomes stronger, the filaments tend to be more stable as discussed in the supervision behavior. Also, sudden withdrawal of this electric field perturbs the stability while a slow rate withdrawal has negligible effect. In addition, higher reading voltages above 300 mV during the pulse sequence helps to form thick filaments which will be stable for long time and retains even in the absence of the reading voltage thus lead to interest-based learning. Since the ASN has diverse nanogaps, during food pulse filaments are formed between

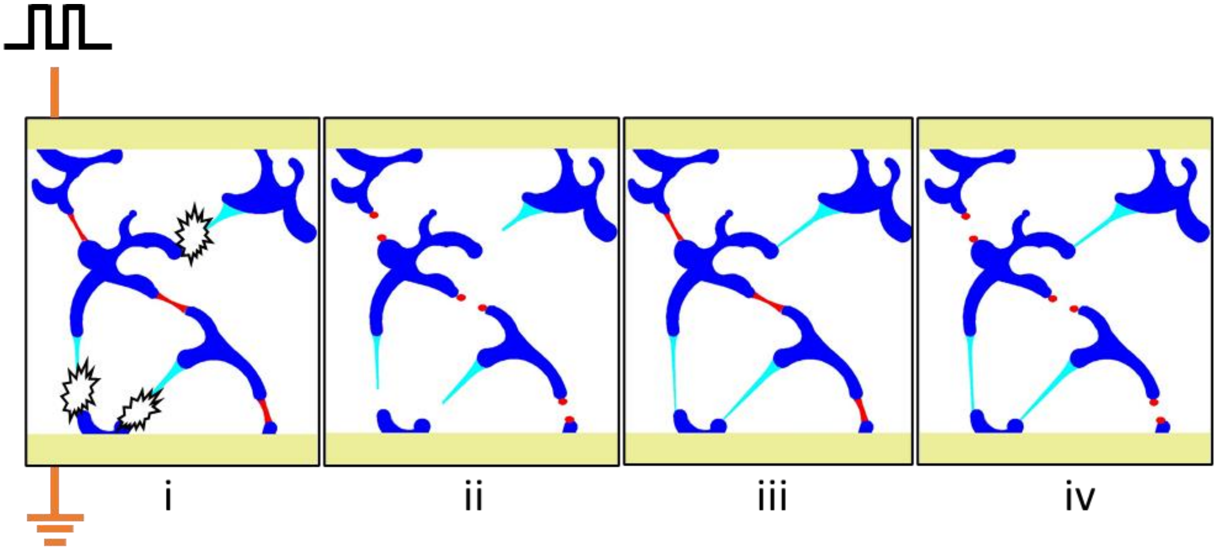

Figure IIIB.14: Schematic showing the hypothesized mechanism of associative learning in device.

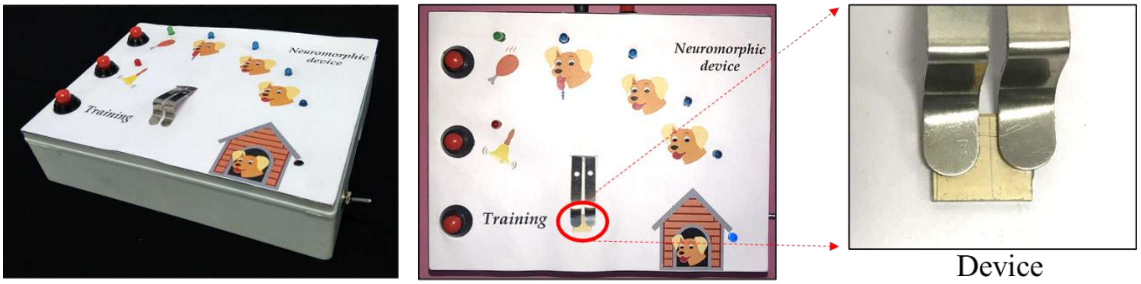

Figure IIIB.15: Digital photograph of the interactive prototype kit and the device.

Table IIIB.1: Synaptic performance comparison of multi-terminal devices from the literature. Advanced behavioral patterns can be emulated either using hardware-based configuration or using software based neural networks. Here, only hardware based behavioral studies are considered for comparison.

Material	Supporting circuit	Signal	STP	LTP	P/D	Supervision	Impression of supervision	Interest/ mood based learning	Associative learning		Ref
									First order	Second order	
ITO/Nb:SrTiO$_3$/ITO	-	O	✓	✓	-	-	-	✓	-	-	9
ITO/Al$_2$O$_3$/PI/Ag	-	E	-	-	-	-	-	-	✓	-	4
Pt/FeO$_x$/SiO$_2$/Pt	✓	E	-	-	-	-	-	-	✓	-	7
Ni/NiOx/Ni/Au	✓	E	-	✓	-	-	-	-	✓	-	6
Pt/Ge$_{0.3}$Se$_{0.7}$/SiO$_2$/ Cu	✓	E	-	-	-	-	-	-	✓	-	13
Au NPs/ pentacene	✓	E	-	-	-	-	-	-	✓	-	14
Pt/Ag/SiO$_x$:Ag/Ag/ Pt + Pt/Ta$_2$O$_5$/TaO$_x$/ Pt	✓	E	-	-	-	-	-		✓	-	15
ITO/ Chitosan /ITO	-	E	-	-	✓	-	-	-	✓	-	16
ITO/PEDOT:PSS/ CuSCN/ CsPbBr$_3$PNs/Au	-	O + E	✓	✓	✓	-	-	-	-	-	17
Mo/CdS/ ZTO/Mo	-	O	✓	✓	-	-	-	-	✓	-	18
Au/PMMA/MAPbI$_3$/Si NM/SiO$_2$/ Si	-	O	✓	✓	-	-	-	✓	-	-	19
ITO/PCBM/ MAPbI$_3$:SiNCs/ Spiro-OMeTAD/Au	-	O	✓	-	-	-	-	-	-	-	20
poly-Si/SiO$_2$/Si$_3$N$_4$/ SiO$_2$/Si	-	E	✓	✓	✓	-	-	-	-	-	21
Au/La$_{1.875}$Sr$_{0.125}$NiO$_4$/ Au	-	O	✓	✓	-	-	-	-	-	-	22
Au/IGZO/alkylated GO/ion gel/ Au	-	O + E	✓	✓	✓	-	-	-	-	-	23
Au/WS$_2$/ PZT/Au	-	O + E	✓	✓	✓	-	-	-	-	-	24
Pt/TiN/ Pr$_{0.7}$Ca$_{0.3}$MnO$_3$/Pt	✓	E	-	-	✓	-	-	-	✓	-	25
Au/Ag-ASN/Au	**-**	**E**	✓	✓	✓	✓	✓	✓	✓	✓	**This work**

O = Optical, E = Electrical, P = Potentiation, D = Depression reasonably smaller nanogaps which has a set current compliance (100 μA) handling capacity (red color bridge in case i, Figure IIIB.14). Whereas conical filaments try to bridge relatively large nanogaps but will get ruptured due to low ampacity owing to their thin dimension (cyan color bridge in case ii, Figure IIIB.14). But during training, the presence of bell pulse stabilizes the thinner filaments (case iii) and thus, post association, the device will respond to the bell pulse alone (case iv). Using the device, a prototype Pavlov's dog interactive kit has been fabricated (Figure IIIB.15) and its performance is demonstrated in the movie. In the prototype, the three switches correspond to the food, bell and training signals. The food switch imparts 20 pulses of a 2 V signal (indicated by green LED), the bell switch imparts 20 pulses of a 0.5 V signal (indicated by red LED) and the training switch imparts one set of both, food and bell signals. The conductance state of the device is indicated by the blue LEDs. In the present context, it indicates the dog's position; either at its home (a glowing blue LED in the bottom right of the prototype box) or running towards food and salivating (transition in blue LEDs towards green LED). When the food switch is pressed, the dog response is indicated by transition in blue LEDs which is not seen for the bell switch. Two sets of training signals are provided and then the response for bell is inspected. Since the training was insufficient, the dog showed no response of salivation. An additional 5 sets of training are imparted, and then the dog responds to the bell switch, indicating the association depicted by the transition in the blue LEDs. Repeated inspection with the bell switch without the food switch showed an extinction as expected.

IIIB.5 Conclusions

By exploiting the bio neural network like structure and massive artificial synaptic junctions in ASN higher cognitive actions were emulated. By varying the reading voltage (10 to 300 mV) to the two-terminal device, supervision behavior was imitated. With carefully designed pulse configuration, impression of supervision was also mimicked by gradually (10 mV/s) withdrawing supervision voltage. Contrary to the unmotivated learning, interest-based learning was accomplished using higher reading voltages (300 to 500 mV). First and second order associative learning was emulated by configuring three voltage signals. Interestingly, all of these synaptic actions were emulated in a single material system without the aid of any CMOS circuits and multi-terminal electrodes. A prototype kit developed to emulate Pavlov's dog behavior clearly demonstrated the potential of the device towards neuromorphic artificial intelligence.

References

[1] D. Kuzum, R. G. D. Jeyasingh, B. Lee, and H. S. P. Wong, *Nanoelectronic Programmable Synapses Based on Phase Change Materials for Brain-Inspired Computing*, Nano Lett. **12**, 2179 (2012).

[2] Y. Park and J. S. Lee, *Artificial Synapses with Short- and Long-Term Memory for Spiking Neural Networks Based on Renewable Materials*, ACS Nano **11**, 8962 (2017).

[3] W. Xu, H. Cho, Y. H. Kim, Y. T. Kim, C. Wolf, C. G. Park, and T. W. Lee, *Organometal Halide Perovskite Artificial Synapses*, Adv. Mater. **28**, 5916 (2016).

[4] C. Wu, T. W. Kim, T. Guo, F. Li, D. U. Lee, and J. J. Yang, *Mimicking Classical Conditioning Based on a Single Flexible Memristor*, Adv. Mater. **29**, 1602890 (2017).

[5] R. A. John, F. Liu, N. A. Chien, M. R. Kulkarni, C. Zhu, Q. Fu, A. Basu, Z. Liu, and N. Mathews, *Synergistic Gating of Electro-Iono-Photoactive 2D Chalcogenide Neuristors: Coexistence of Hebbian and Homeostatic Synaptic Metaplasticity*, Adv. Mater. **30**, 1800220 (2018).

[6] S. G. Hu, Y. Liu, Z. Liu, T. P. Chen, Q. Yu, L. J. Deng, Y. Yin, and S. Hosaka, *Synaptic Long-Term Potentiation Realized in Pavlov's Dog Model Based on a NiOx-Based Memristor*, J. Appl. Phys. **116**, 214502 (2014).

[7] X. Wan, D. Liang, F. Gao, X. Lian, and Y. Tong, *Hardware Implementation of Classical Conditioning with Iron-Oxide-Based Memristors*, Appl. Phys. Express **11**, 114601 (2018).

[8] Y. Van De Burgt, E. Lubberman, E. J. Fuller, S. T. Keene, G. C. Faria, S. Agarwal, M. J. Marinella, A. Alec Talin, and A. Salleo, *A Non-Volatile Organic Electrochemical Device as a Low-Voltage Artificial Synapse for Neuromorphic Computing*, Nat. Mater. **16**, 414 (2017).

[9] S. Gao, G. Liu, H. Yang, C. Hu, Q. Chen, G. Gong, W. Xue, X. Yi, J. Shang, and R. W. Li, *An Oxide Schottky Junction Artificial Optoelectronic Synapse*, ACS Nano **13**, 2634 (2019).

[10] Z. Zhang, T. Li, Y. Wu, Y. Jia, C. Tan, X. Xu, G. Wang, J. Lv, W. Zhang, Y. He, J. Pei, C. Ma, G.

Li, H. Xu, L. Shi, H. Peng, and H. Li, *Truly Concomitant and Independently Expressed Short- and Long-Term Plasticity in a Bi2O2Se-Based Three-Terminal Memristor*, Adv. Mater. **31**, 1805769 (2019).

[11] I. P. Pavlov, *Conditioned Reflexes: An Investigation of the Physiological Activity of the Cerebral Cortex*, Ann. Neurosci. **17**, 136 (2010).

[12] S. La Barbera, D. Vuillaume, and F. Alibart, *Filamentary Switching: Synaptic Plasticity through Device Volatility*, ACS Nano **9**, 941 (2015).

[13] M. Ziegler, R. Soni, T. Patelczyk, M. Ignatov, T. Bartsch, P. Meuffels, and H. Kohlstedt, *An Electronic Version of Pavlov's Dog*, Adv. Funct. Mater. **22**, 2744 (2012).

[14] O. Bichler, W. Zhao, F. Alibart, S. Pleutin, S. Lenfant, D. Vuillaume, and C. Gamrat, *Pavlov's Dog Associative Learning Demonstrated on Synaptic-like Organic Transistors*, Neural Computation **25,** 549 (2013).

[15] Z. Wang, M. Rao, J. W. Han, J. Zhang, P. Lin, Y. Li, C. Li, W. Song, S. Asapu, R. Midya, Y. Zhuo, H. Jiang, J. H. Yoon, N. K. Upadhyay, S. Joshi, M. Hu, J. P. Strachan, M. Barnell, Q. Wu, H. Wu, Q. Qiu, R. S. Williams, Q. Xia, and J. J. Yang, *Capacitive Neural Network with Neuro-Transistors*, Nat. Commun. **9**, 8409 (2018).

[16] F. Yu, L. Q. Zhu, H. Xiao, W. T. Gao, and Y. B. Guo, *Restickable Oxide Neuromorphic Transistors with Spike-Timing-Dependent Plasticity and Pavlovian Associative Learning Activities*, Adv. Funct. Mater. **28**, 1804025 (2018).

[17] F. Ma, Y. Zhu, Z. Xu, Y. Liu, X. Zheng, S. Ju, Q. Li, Z. Ni, H. Hu, Y. Chai, C. Wu, T. W. Kim, and F. Li, *Optoelectronic Perovskite Synapses for Neuromorphic Computing*, Adv. Funct. Mater. **30**, 1908901 (2020).

[18] S. W. Cho, S. M. Kwon, M. Lee, J. W. Jo, J. S. Heo, Y. H. Kim, H. K. Cho, and S. K. Park, *Multi-Spectral Gate-Triggered Heterogeneous Photonic Neuro-Transistors for Power-Efficient Brain-Inspired Neuromorphic Computing*, Nano Energy **66**, 104097 (2019).

[19] L. Yin, W. Huang, R. Xiao, W. Peng, Y. Zhu, Y. Zhang, X. Pi, and D. Yang, *Optically Stimulated Synaptic Devices Based on the Hybrid Structure of Silicon Nanomembrane*

and Perovskite, Nano Lett. **20**, 3378–3387 (2020).

[20] W. Huang, P. Hang, Y. Wang, K. Wang, S. Han, Z. Chen, W. Peng, Y. Zhu, M. Xu, Y. Zhang, Y. Fang, X. Yu, D. Yang, and X. Pi, *Zero-Power Optoelectronic Synaptic Devices*, Nano Energy **73**, 104790 (2020).

[21] J. Hur, B. C. Jang, J. Park, D. Il Moon, H. Bae, J. Y. Park, G. H. Kim, S. B. Jeon, M. Seo, S. Kim, S. Y. Choi, and Y. K. Choi, *A Recoverable Synapse Device Using a Three-Dimensional Silicon Transistor*, Adv. Funct. Mater. **28**, 1804844 (2018).

[22] L. Zhao, Z. Fan, S. Cheng, L. Hong, Y. Li, G. Tian, D. Chen, Z. Hou, M. Qin, M. Zeng, X. Lu, G. Zhou, X. Gao, and J. M. Liu, *An Artificial Optoelectronic Synapse Based on a Photoelectric Memcapacitor*, Adv. Electron. Mater. **6**, 1900858 (2020).

[23] J. Sun, S. Oh, Y. Choi, S. Seo, M. J. Oh, M. Lee, W. B. Lee, P. J. Yoo, J. H. Cho, and J. H. Park, *Optoelectronic Synapse Based on IGZO-Alkylated Graphene Oxide Hybrid Structure*, Adv. Funct. Mater. **28**, 1804397 (2018).

[24] Z. D. Luo, X. Xia, M. M. Yang, N. R. Wilson, A. Gruverman, and M. Alexe, *Artificial Optoelectronic Synapses Based on Ferroelectric Field-Effect Enabled 2D Transition Metal Dichalcogenide Memristive Transistors*, ACS Nano **14**, 746 (2020).

[25] K. Moon, S. Park, J. Jang, D. Lee, J. Woo, E. Cha, S. Lee, J. Park, J. Song, Y. Koo, and H. Hwang, *Hardware Implementation of Associative Memory Characteristics with Analogue-Type Resistive-Switching Device*, Nanotechnology **25**, 495204 (2014).

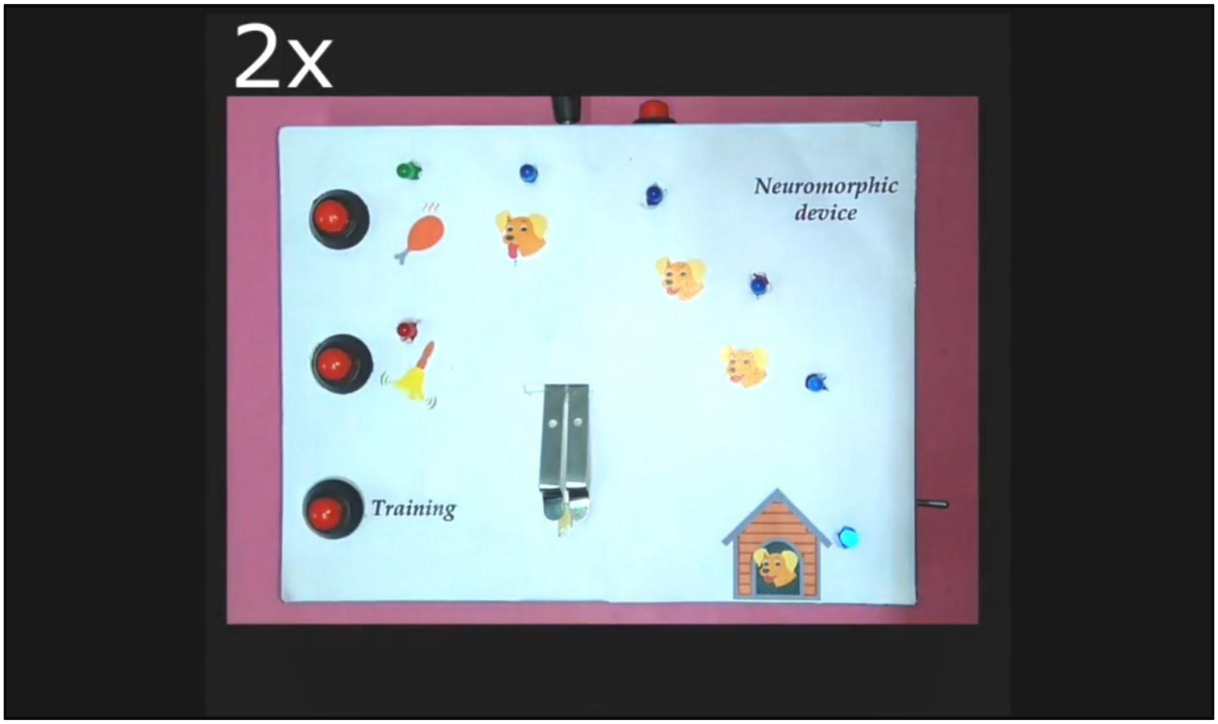

A movie showing the performance of the Pavlov's dog interactive kit.

Chapter IIIC

Emulating Neural Damage in an Artificial Synaptic Network *

Summary

An important phenomenon in biological systems known as synaptic fatigue and recovery, occurring due to colossal learning events, has been successfully demonstrated in the ASN device. Also, with the device switched to LTP, the effect of an accident or of a stroke-induced physical damage was emulated by mildly scratching the active region using a nanomanipulator. The damaged device showed neuroplasticity behavior analogous to a biosystem such as damage dependent memory formation and short-term memory loss. Interestingly, a common phenomenon called “tip of the tongue experience” is also mimicked in the device.

IIIC.1 Introduction

The human brain is an excellent computing system known to mankind till date. Owing to its massive cognitive abilities performed with great efficiency, researchers have been fascinated to try and mimic those behaviors in electronic devices and accomplish an excellence in their performance [1–3]. Although the brain performs complex cognition, it is prone to damage by fatigue, accidents or stroke-induced physical injury and others [4–6]. Excessive learning activity is a major cause of synaptic fatigue, where the synapse gets depleted of neurotransmitters due to the high frequency signal spikes, leading to its failure [7–9]. On the contrary, a physical injury ruptures the neuronal interconnections or the synaptic network which is essential for the memory/learning activity. After experiencing such damage, the memory/learning activity fails significantly depending on the extent of damage. In a synaptic fatigue, the synapse stops responding to the neuronal action potential, thus showing no response. Also, if the physical damage is minor, new neural connections can form during the successive medication therapy, thus evoking learning/memory activity. But in case of severe damage, new neural connections may not be feasible even after intense medication leading to the short-term memory loss condition [7,10,11]. It is highly challenging to emulate these important features in neuromorphic devices.

---

*Part of this Chapter is from: Mater.Horiz., **7**, 2970 (2020).

Limited studies exist in emulating synaptic fatigue and recovery in neuromorphic devices. Choi et al., for the first time, showed the possibility of recovering the device after a fatigue in a trap assisted silicon FinFET architecture [12]. A series of voltage spikes were intentionally imparted to the device. After 10^5 cycles, due to the capture of electrons in deep trap levels, the device showed 30% degradation in the conductance indicating the fatigue. Joule heating was then performed to release the trapped electrons thereby recovering the device. Although there was degradation in the conductance, complete fatigue and then recovery was not observed. Relating to physical damage, Guo et al., reported intrinsic healing ability of a PEDOT:PSS/hydrogel based neuromorphic device [13]. After the active channel was cut with a blade, the device was healed by water treatment via PSS swelling and dynamic hydrogen bonding. After healing the active channel, the device behavior was restored fully. In another report, Mathews et al., reported an ion gel based device showing complete healing ability owing to intermolecular interactions and reduced glass transition temperature [14]. These examples more closely resemble the healing feature of biological tissues rather than recovery of synaptic network damage.

IIIC.2 Scope of the present investigation

Along with mimicking synaptic behaviors, it is also important to emulate the bio system's damage and recovery features in neuromorphic devices to produce promising next-generation artificial neuromorphic systems. But at the same time, it is highly challenging to mimic these features in electronic devices, one of the factors being the device architecture. Even in the existing limited examples, these features are not fully emulated. And moreover, the device consists of complex architecture and involves an intricate fabrication process. Furthermore, in a real scenario, memory/learning activity is impaired after injury, which is not explored in the literature. Thus, in the present work, taking advantage of the close resemblance of the ASN structure to a bio-neural network, several damage-dependent memory features were explored. Large number of voltage signal spikes were intentionally applied to the device to emulate synaptic fatigue and are then recovered by voltage sweep. Apart from mimicking synaptic fatigue, the recovery of the device also features the robustness of the device. In addition, scratches were introduced in the active channels to mimic a physical injury and emulate memory impairment.

IIIC.3 Experimental details

Scratch damage was performed on a two-terminal ASN device using a nanomanipulator integrated with FESEM. The tip size of the nanomanipulator ranges from 150 nm to a few microns. For scratch damage, a tip size of ~1 μm was chosen. Keithley 4200 SCS was used to apply the electrical pulse signal.

IIIC.4 Results and discussion

Synaptic fatigue is an interesting feature observed in biological systems. Due to colossal learning, the biological synapse gets depleted of neurotransmitters causing fatigue. Fortunately, biological systems diagnose this condition and initiate retrieval of neurotransmitters back into the neurons thereby recovering the synapses [15,16]. A similar behavior was emulated in the ASN device. After experiencing a large number of learning events (> 10^4 cycles), the device underwent fatigue and did not respond to the usual 2 V pulse sequence (Figure IIIC.1a). This might have occurred due to the depletion of metal in the preferential filament path owing to large switching cycles. To recover the switching behavior, a high voltage I-V sweep was performed with 100 nA current compliance as

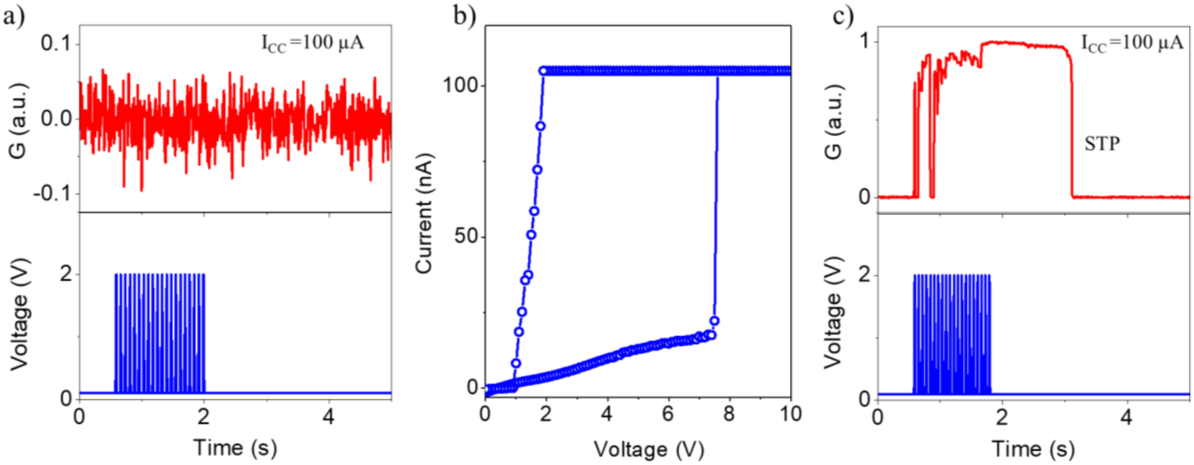

Figure IIIC.1: Observation of synaptic fatigue and recovery. a) Due to the colossal learning cycle (> 10^4), the device did not respond, undergoing fatigue similar to the biological synapse. b) To reactivate, the device was subjected to voltage sweep at a higher voltage range where it recovers the switching behavior. c) Further, under the application of usual voltage pulses, the device starts responding, thus displaying the synaptic recovery. (20 pulses of 2 V, 50 ms width as well as interval, 100 mV reading voltage, 100 μA current compliance).

damage protection as shown in Figure IIIC.1b. The device then switched to a high conducting state at ~ 7.5 V. This may be attributed to the electromigration of metal either in previous filament path or in a new susceptible path, indicating structural plasticity. The device was again subjected to a 2 V pulse sequence in STP configuration and an efficient switching was observed showing the synaptic recovery (Figure IIIC.1c).

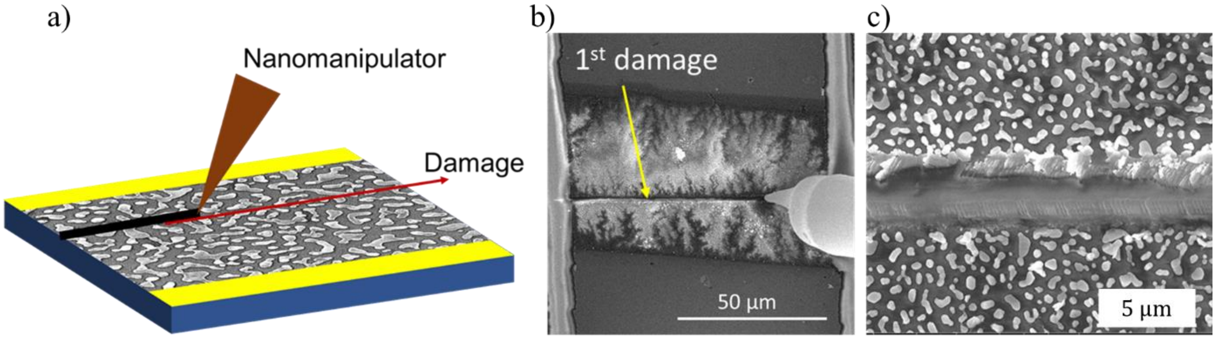

Figure IIIC.2: a) Schematic illustration of the scratching process using a nanomanipulator. b) SEM image of the nanomanipulator scratching process. c) Magnified view of the scratch damage.

Further, to emulate the effect of physical injury in the device, a scratch was introduced in the active region using a nanomanipulator. Figure IIIC.2a shows the schematic illustration of the damage process and the corresponding SEM images are shown in Figure III.2b,c. Before the damage, I-V sweep was performed to confirm the device's switching nature, as shown in

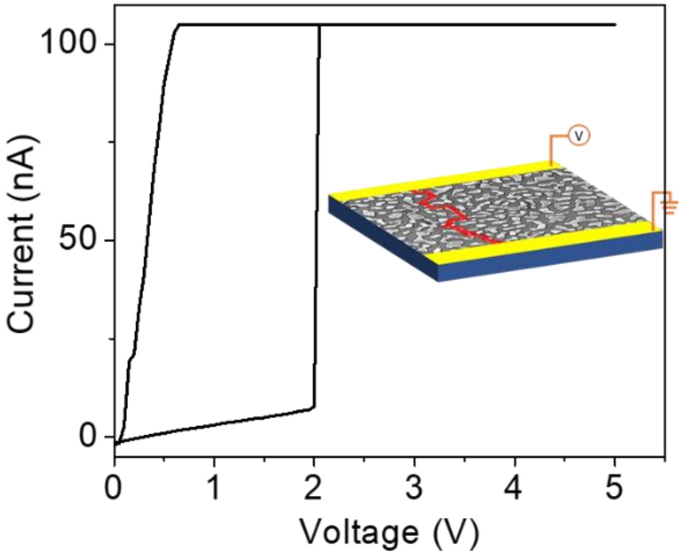

Figure IIIC.3: I-V characteristics of the device before performing the damage. Inset showing the schematic illustration of the filament path.

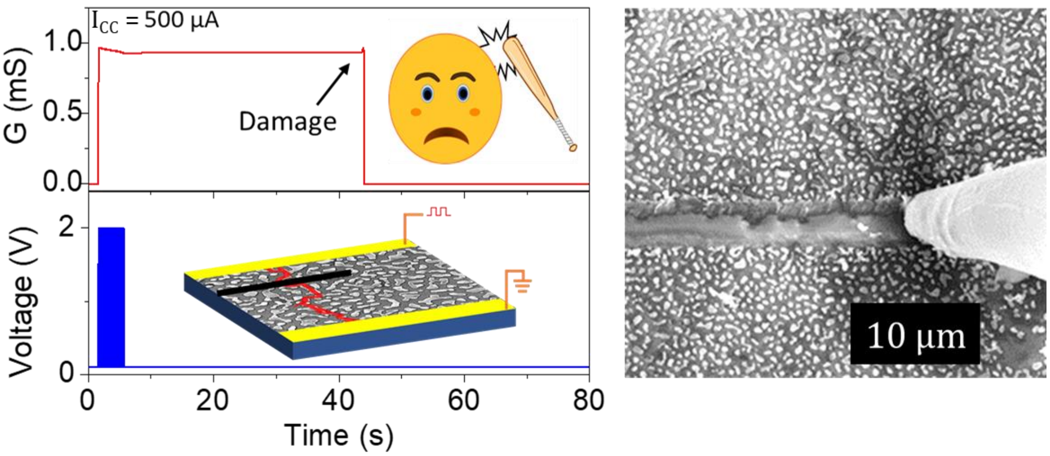

Figure IIIC.4: Device was switched to LTP state, and a first scratch was introduced using the nanomanipulator. Inset shows the schematic representation of filament rupture. SEM image shows the scratch by nanomanipulator. (20 pulses of 2 V, 50 ms width as well as interval, 100 mV reading voltage, 500 μA current compliance).

Figure IIIC.3. Later the device was subjected to LTP pulse configuration to form stable conducting filaments. Once achieved, the active region was scratched using the nanomanipulator until the device conductance dropped to its initial value (Figure IIIC.4), which is an indication of the rupture of the active filament path. This is analogous to memory failure during physical injury to the brain, whose recovery depends on the extent of damage. To recover the device switching behavior, I-V sweep was performed, as shown in Figure IIIC.5a. Interestingly, the device switched at a higher threshold voltage during the I-V sweep, thus indicating new filament path formation. Once the switching voltage was optimized by successive I-V cycles, usual pulse signals were applied to emulate STP and LTP. In Figure IIIC.5b, although slight perturbed STP was observed in the beginning, it recovered during successive cycles (Figure IIIC.5c). Similarly, LTP was emulated with 500 μA current compliance showed minor fluctuation in conductance (Figure IIIC.5d). This perturbance in emulating synaptic action shows the effect of damage similar to that observed in its bio counterpart. Another scratch was introduced to observe the effect of intense damage, (Figure IIIC.6a) while the device was switched back to LTP state. From Figure IIIC.6b, the rupture of filament path is indicated by a drop in the conducting state as discussed earlier. Again, I-V sweep was performed to check the possibility of a new filament connection, as shown in Figure IIIC.7a. Interestingly, the device once again showed switching behavior indicating a

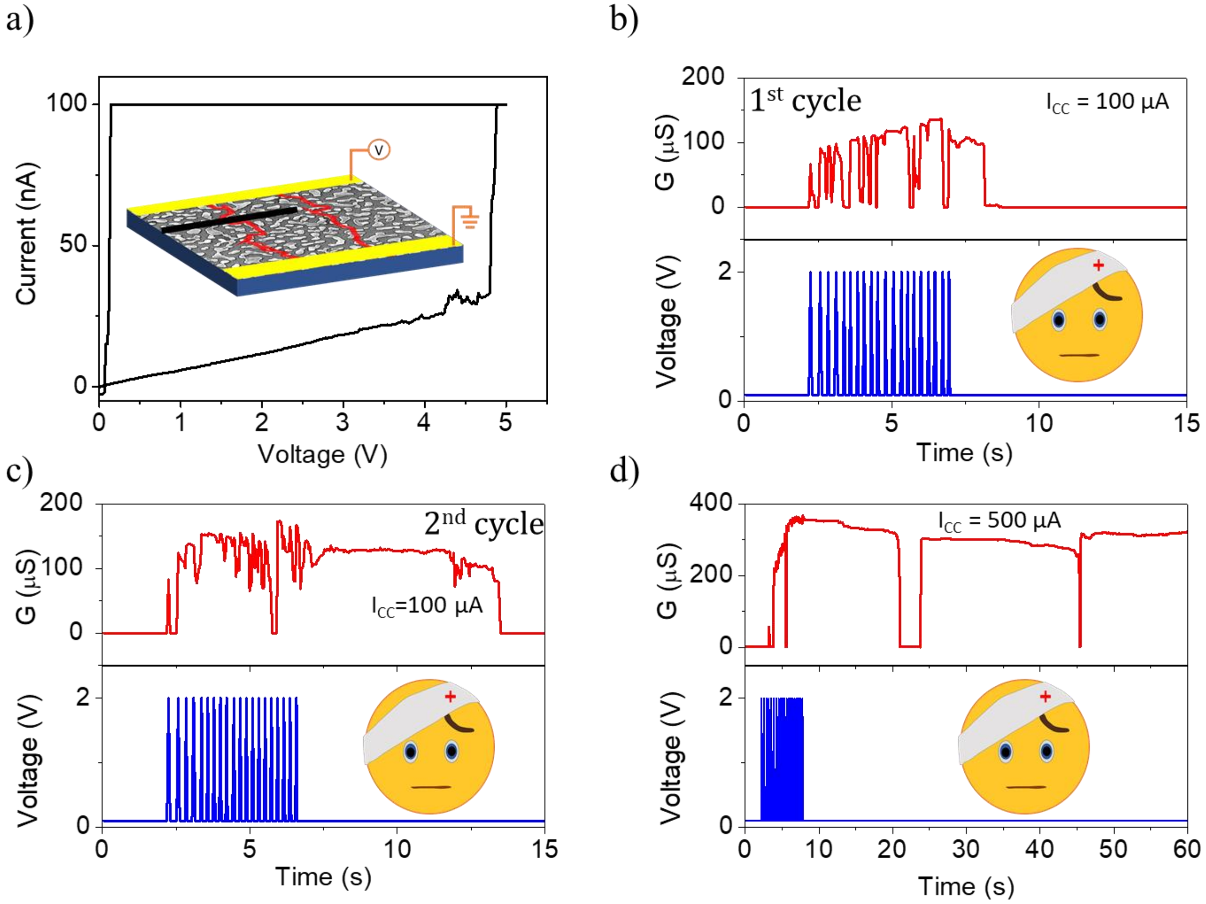

Figure IIIC.5: a) I-V characteristics of the device after 1st damage. Inset showing the schematic illustration of new filament path formation. b) STP behavior in the first cycle. c) Improved STP behavior in the 2nd cycle. d) Minor fluctuations in LTP behavior after damage. (20 pulses of 2 V, 50 ms width as well as interval, 100 mV reading voltage).

new structural connection. Emulation of STP in Figure IIIC.7b showed that during the first few cycles, highly perturbed conductance was observed, which got improved in the successive cycles. Whereas in emulating LTP using typical pulse configuration, the device could not retain the conductance state for longer (above 60 s) time (Figure IIIC.8a-c). Even increasing the current compliance to a higher value (5 mA) did not result in the LTP showing its permanent damage (Figure IIIC.8d). This is very similar to the condition of short-term memory loss in the brain after intense damage.

Another interesting phenomenon observed in day to day activity is the temporary memory loss and its recollection commonly known as the 'tip of the tongue experience' [17,18]. Most of the time, information that slipped from memory can be reminisced by the continuous effort of recollection often intercepted by a relaxing sleep. Here a similar behavior is observed in the ASN device. First, the device was switched in STP condition, as shown in Figure IIIC.9a. After a few seconds (~10 s), the conductance dropped to the original value resembling memory loss. Now the reading voltage was continually applied as an effort of

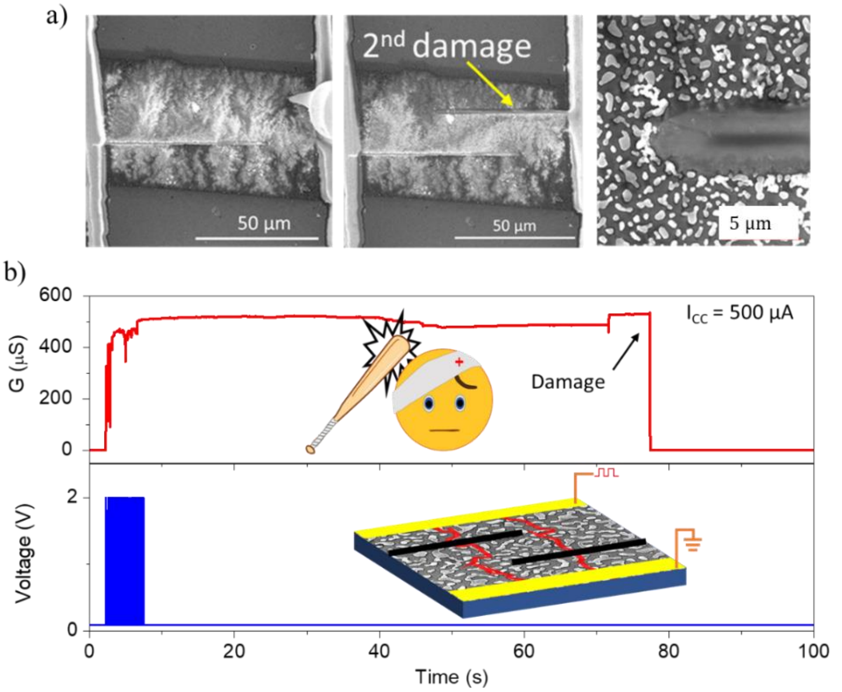

Figure IIIC.6: a) SEM image showing the 2nd scratch damage generated using the nanomanipulator. b) Device was switched to LTP state and the 2nd scratch was introduced using the nanomanipulator. Bottom inset shows the schematic illustration of a filament rupture. (20 pulses of 2 V, 50 ms width as well as interval, 100 mV reading voltage, 500 μA current compliance).

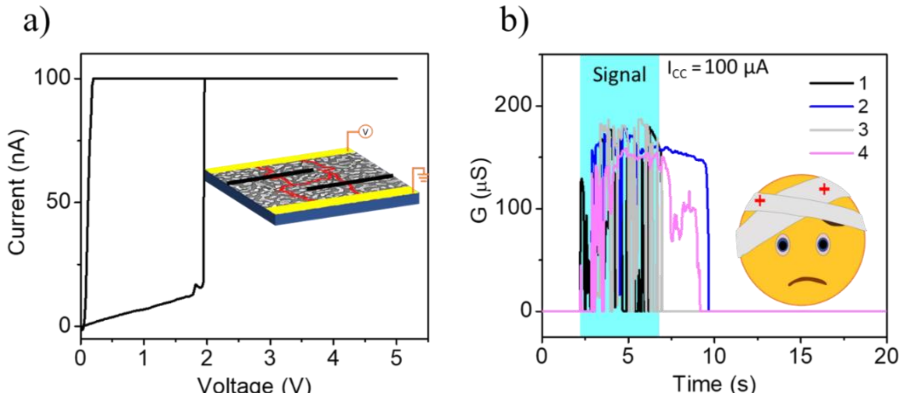

Figure IIIC.7: a) I-V characteristics of the device after 2nd scratch damage. Inset showing the schematic illustration of the possible new filament path formation. b) STP behavior of the device after 2nd damage. (20 pulses of 2 V, 50 ms width as well as interval, 100 mV reading voltage, 100 μA current compliance).

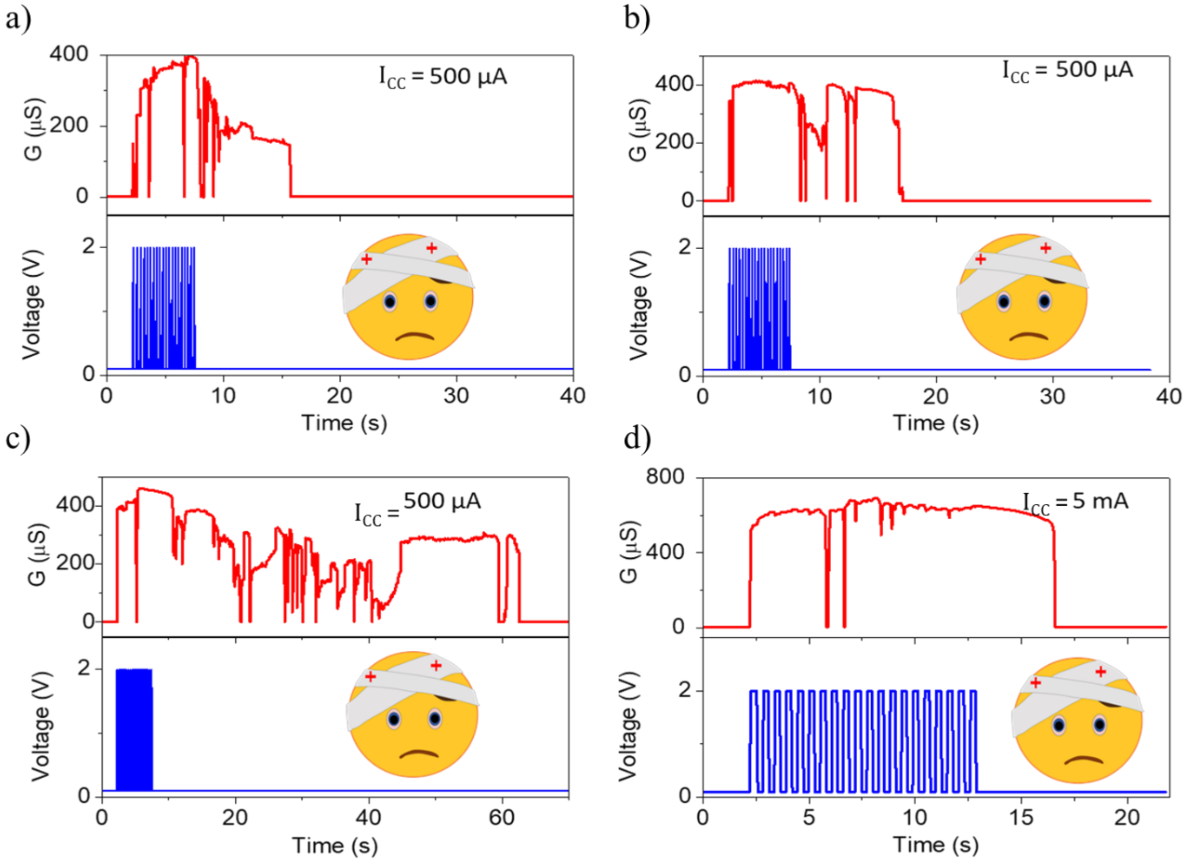

Figure IIIC.8: a) Conductance retention shows that the device fails to emulate LTP behavior even for several cycles (b, c). d) Even after increasing the current compliance to 5 mA did not improve the retention thus indicating the permanent LTP damage. (20 pulses of 2 V, 50 ms width as well as interval, 100 mV reading voltage).

recollection. Amazingly, after a definite time interval (~90 s), the device switched itself to a high conductance state resembling the memory recall. Reproducibility is shown in Figure III.9b. The possible mechanism is illustrated in Figure IIIC.10. During the pulse sequence application, the conductive filament is formed due to the electromigration (Figure IIIC.10a) which later relaxes back due to the short-term dynamics (Figure IIIC.10b). During this relaxation process, if the gap between the filament and the island is sufficiently narrow (~few nm), then the Coulombic attraction can lead to the 'jump to contact' phenomenon thereby reconnecting the filament (Figure IIIC.10c) [19,20]. The probability of occurrence of this behavior in the ASN device was found to be around 10%.

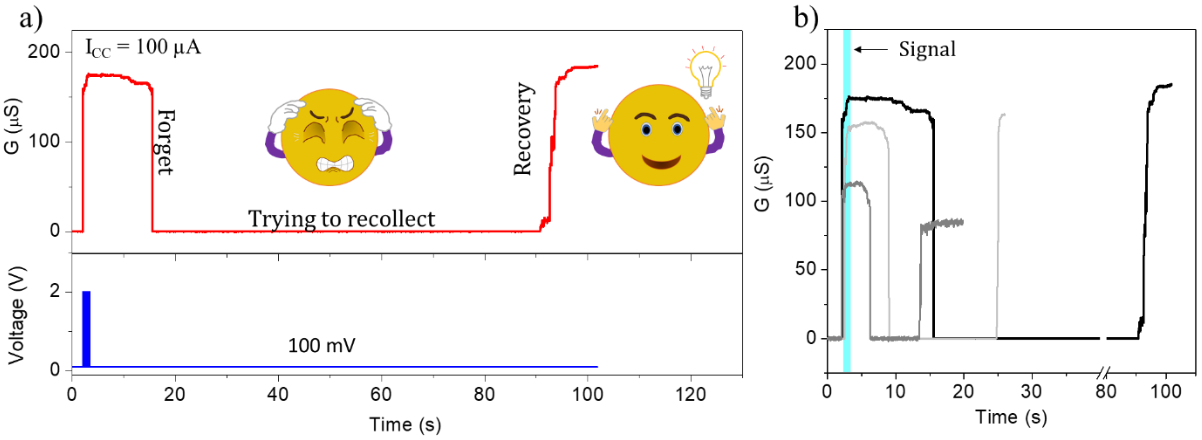

Figure IIIC.9: Tip of the tongue experience. a) Device conductance behavior for usual STP pulse configuration is shown. Typical STP behavior is observed by the conductance drop in 10 s. Reading voltage is continuously applied as a recollection effort and after ~90 s, the conductance jump was observed. b) Behavior observed for different cycles. (20 pulses of 2 V, 50 ms width as well as interval, 100 mV reading voltage, 100 µA current compliance).

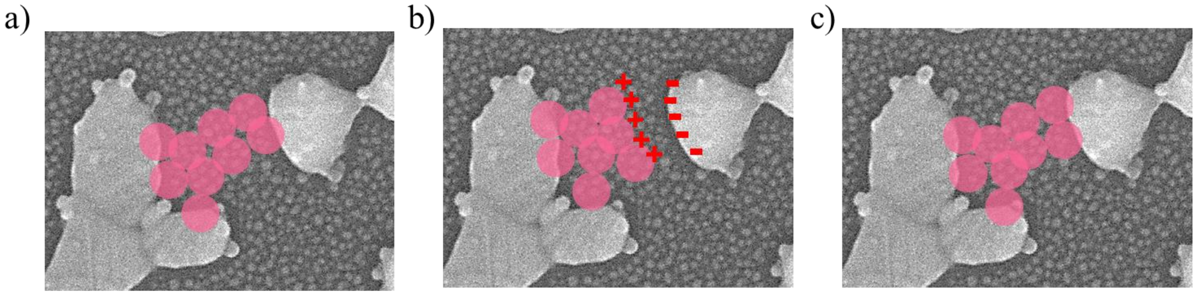

Figure IIIC.10: Schematic illustration of possible mechanism. a) Filament formation during the application of pulse sequence. b) Filament rupture due to short-term dynamics. c) Coulombic attraction may lead to 'jump to contact' phenomena.

IIIC.5 Conclusions

Exotic damage-dependent memory recovery features were emulated in the ASN device. The device experienced fatigue after >10^4 switching cycles analogous to the synaptic fatigue observed in the brain. Recovery of the synapse was achieved by performing I-V sweep for facilitating electromigration. Introducing a physical damage to the system induced a perturbed synaptic activity thus emulating memory impairment and short-term memory loss phenomena as observed in the human brain. A commonly seen feature known as tip of the tongue experience is also observed in the device.

References

[1] S. B. Furber, *Brain-Inspired Computing*, IET Comput. Digit. Tech. **10**, 299 (2016).

[2] D. Marković, A. Mizrahi, D. Querlioz, and J. Grollier, *Physics for Neuromorphic Computing*, Nat. Rev. Phys. **2**, 499 (2020).

[3] T. Wunderlich, A. F. Kungl, E. Müller, A. Hartel, Y. Stradmann, S. A. Aamir, A. Grübl, A. Heimbrecht, K. Schreiber, D. Stöckel, C. Pehle, S. Billaudelle, G. Kiene, C. Mauch, J. Schemmel, K. Meier, and M. A. Petrovici, *Demonstrating Advantages of Neuromorphic Computation: A Pilot Study*, Front. Neurosci. **13**, 260 (2019).

[4] L. D. Pozzo-Miller, W. Gottschalk, L. Zhang, K. McDermott, J. Du, R. Gopalakrishnan, C. Oho, Z. H. Sheng, and B. Lu, *Impairments in High-Frequency Transmission, Synaptic Vesicle Docking, and Synaptic Protein Distribution in the Hippocampus of BDNF Knockout Mice*, J. Neurosci. **19**, 4972 (1999).

[5] K. Blennow, D. L. Brody, P. M. Kochanek, H. Levin, A. McKee, G. M. Ribbers, K. Yaffe, and H. Zetterberg, *Traumatic Brain Injuries*, Nat. Rev. Dis. Prim. **2**, 16084 (2016).

[6] P. Azouvi, A. Arnould, E. Dromer, and C. Vallat-Azouvi, *Neuropsychology of Traumatic Brain Injury: An Expert Overview*, Rev. Neurol. (Paris). **173**, 461 (2017).

[7] D. Man, C. Yip, G. Lee, J. Fleming, and D. Shum, *Self-Report Prospective Memory Problems in People with Stroke*, Brain Inj. **29**, 329 (2015).

[8] M. Leśniak, T. Bak, W. Czepiel, J. Seniów, and A. Członkowska, *Frequency and Prognostic Value of Cognitive Disorders in Stroke Patients*, Dement. Geriatr. Cogn. Disord. **26**, 356 (2008).

[9] F. Kawasaki, M. Hazen, and R. W. Ordway, *Fast Synaptic Fatigue in Shibire Mutants Reveals a Rapid Requirement for Dynamin in Synaptic Vesicle Membrane Trafficking*, Nat. Neurosci. **3**, 859 (2000).

[10] C. Hogan, J. Fleming, P. Cornwell, and D. Shum, *Prospective Memory after Stroke: A Scoping Review*, Brain Impair. **17**, 123 (2016).

[11] L. Palermo, M. C. Cinelli, L. Piccardi, S. De Felice, P. Ciurli, C. Incoccia, L. Zompanti, and C. Guariglia, *Cognitive Functions Underlying Prospective Memory Deficits: A Study on Traumatic Brain Injury*, Appl. Neuropsychol. **27**, 158 (2020).

[12] J. Hur, B. C. Jang, J. Park, D. Il Moon, H. Bae, J. Y. Park, G. H. Kim, S. B. Jeon, M. Seo, S. Kim, S. Y. Choi, and Y. K. Choi, *A Recoverable Synapse Device Using a Three-Dimensional Silicon Transistor*, Adv. Funct. Mater. **28**, 1804844 (2018).

[13] Y. Yan, X. Wu, Q. Chen, X. Wang, E. Li, Y. Liu, H. Chen, and T. Guo, *An Intrinsically Healing Artificial Neuromorphic Device*, J. Mater. Chem. C **8**, 6869 (2020).

[14] R. A. John, N. Tiwari, M. I. Bin Patdillah, M. R. Kulkarni, N. Tiwari, J. Basu, S. K. Bose, Ankit, C. J. Yu, A. Nirmal, S. K. Vishwanath, C. Bartolozzi, A. Basu, and N. Mathews, *Self Healable Neuromorphic Memtransistor Elements for Decentralized Sensory Signal Processing in Robotics*, Nat. Commun. **11**, 4030 (2020).

[15] G. Rudnick and J. Clark, *From Synapse to Vesicle: The Reuptake and Storage of Biogenic Amine Neurotransmitters*, BBA - Bioenerg. **1144**, 249 (1993).

[16] B. I. Kanner and S. Schuldiner, *Mechanism of Transport and Storage of Neurotransmitter*, Crit. Rev. Biochem. Mol. Biol. **22**, 1 (1987).

[17] A. S. Brown, *A Review of the Tip-of-the-Tongue Experience*, Psychol. Bull. **109**, 204 (1991).

[18] C. J. Schmank and L. E. James, *Adults of All Ages Experience Increased Tip-of-the-Tongue States under Ostensible Evaluative Observation*, Aging, Neuropsychol. Cogn. **27**, 517 (2020).

[19] A. Sattar, S. Fostner, and S. A. Brown, *Quantized Conductance and Switching in Percolating Nanoparticle Films*, Phys. Rev. Lett. **111**, 136808 (2013).

[20] C. Untiedt, M. J. Caturla, M. R. Calvo, J. J. Palacios, R. C. Segers, and J. M. Van Ruitenbeek, *Formation of a Metallic Contact: Jump to Contact Revisited*, Phys. Rev. Lett. **98**, 206801 (2007).

Chapter IV

Fabrication of Metal-Organic based Flexible Neuromorphic Device

Summary

A simple solution-based method for fabricating neuromorphic devices has been demonstrated in this chapter. A metal-organic based Palladium hexadecanethiolate (Pd thiolate) precursor was used in device fabrication by optimizing the thermolysis conditions. It was found that device thermalization at various temperatures plays a crucial role in tuning the device's synaptic performance. While the device thermalized at higher temperature showed resistive switching behavior accompanied by potentiation, SNDP and SRDP; a relatively lower thermolysis temperature did not show the anticipated response. Interestingly, the device thermalized at a relatively moderate temperature emulated essential synaptic functions such as STP and LTP. A flexible synaptic device was fabricated using Kapton tape, which demonstrated an excellent stability over 1000 bending cycles and a bending radius up to 1 mm.

IV.1 Introduction

Concerning brain-inspired computing, new circuit elements such as neuromorphic devices, in particular, show highly promising results in mimicking synaptic activities such as STP, LTP, spike-parameter dependent plasticity (SPDP), and other complex cognitions [1,2]. A literature survey shows enormous efforts put into the development of inorganic- and organic-based neuromorphic devices emulating synaptic functions. Inorganic materials such as h-BN, ZnO/TiO_x, Ag:Ta_2O_5, SiO_xN_y:Ag, ZnO/WS_2, and Ag_2S have shown their ability to mimic essential synaptic functions such as STP, LTP to further SPDP [3–12]. However, the fabrication process is intricate, expensive, and often depends on the careful tuning of the material stoichiometry. On the other hand, organic materials are advantageous as they are easily and economically processable and are highly scalable. Materials such as P(VDF-TrFE)/pentacene, FT4-DPP/PEO etc., have shown commendable features with regard to synaptic activities [13–17]. Several neurons undergo bending and stretching during body movements. Thus, along with mimicking synaptic functions, achieving flexibility in neuromorphic devices is imperative for wearable and implantable applications.

Flexible electronics is an essential requirement for accomplishing artificial nervous system and future wearable applications [18]. In most neuromorphic materials, due to the fabrication process parameters, mainly high-temperature, extending them to flexible substrates is challenging. Further, the intrinsic rigid nature of the materials is also a hindrance. Several inorganic and organic systems have been explored towards development of flexible neuromorphic devices [19–24]. Ding et al. showed a flexible amorphous IGZO-based synaptic transistor bendable up to 10 mm bending radius [25]. Zhang et al. showed a room temperature fabricated ZnO/ITO-based flexible device and demonstrated switching behavior in a 10 mm bending radius [26]. In another example, Lu et al. fabricated a poly(vinyl alcohol)-graphene oxide based hybrid neuromorphic device and demonstrated switching behavior at a 10 mm bending radius for 1000 cycles [27]. Li et al. studied polyimide/ethyl viologen diperchlorate based device and found the performance degradation below 10 mm bending radius [28]. While Wan et al. prepared a chitosan-based synaptic transistor with an estimated bending ability of 5 mm [29].

IV.2 Scope of the present investigation

Metallic filament based neuromorphic devices can show stable conductance dynamics mimicking human memory. But due to the rigid nature of inorganic systems, these devices are prone to bending damages. While organic systems have Young's modulus lower than inorganic systems, it makes them highly suitable for flexible electronics [30]. However, devices based on organic materials often rely on trap-assisted synaptic activity, which show decay behavior in the conductance state, typically representing the forgetting curve of the human brain [31–33]. Also, the ambient stability of organic systems is yet another issue for practical applications. A metal-organic system can demonstrate properties from both inorganic and organic systems, such as stable memory dynamics and, simple processing and flexible nature respectively, thus achieving improved device performance. An insulating organic matrix with nucleated metal nanoparticles during thermolysis is explored to fabricate neuromorphic devices in the present invenstigation. The thermolysis temperature was optimized to accomplish a better synaptic performance. Moreover, this solution-based process is endowed with simplicity and scalability. Importantly, demonstrating device properties in the bent state is imperative for future flexible electronics, which is often ignored in the literature. Excitingly, the present device fabrication is extended to a flexible substrate to demonstrate an excellent bending performance.

IV.3 Experimental details

Solution preparation: 0.2 M Palladium hexadecanethiolate, $Pd(SC_{16}H_{35})_2$ was prepared as follows. 45 mg $Pd(OAc)_2$ was dissolved in 1 mL toluene and stirred for 3 hours. Later the stirred solution was added to hexadecanethiol in toluene and stirred for another 3 hours. Post reaction, an orange-yellow colored solution was obtained.

Device fabrication: Glass substrate was sonicated in acetone, IPA, and DI water for 10 min respectively. Au (50 nm thick) gap electrode (gap ~20 μm) was then fabricated using a shadow masking technique and e-beam evaporation. For device fabrication, 100 μL of Pd thiolate solution was drop coated and heated at 200 °C, 230 °C, and 250 °C using a hotplate for different durations. For fabricating a flexible neuromorphic device, Au gap electrodes were fabricated on a Kapton tape (thickness ~50 μm) followed by drop coating Pd thiolate precursor and then annealing at 230 °C.

IV.4 Results and discussion

Figure IV.1a illustrates the schematic of the device fabrication process. Au gap electrodes were fabricated on a clean glass substrate via shadow masking followed by e-beam evaporation. The substrate was then drop coated with Pd-thiol solution and subjected to thermolysis at different temperatures. While annealing, partial decomposition of thiol was facilitated, resulting in Pd nanoparticle nucleation whose size can be tuned by the annealing temperature [34]. Thus, after thermolysis, a nanocomposite film of Pd nanoparticles in the carbon matrix was obtained. Thermolysis was performed in the temperature range of 200 °C to 250 °C. While thermalizing, the device resistance was monitored at constant intervals to make sure to not create excess Pd metal nanoparticles leading to a completely conducting system. While fabricating at 200 °C, the device remained non-conducting even after annealing for 3 hours, suggesting a much lesser possibility of Pd nanoparticle nucleation. A

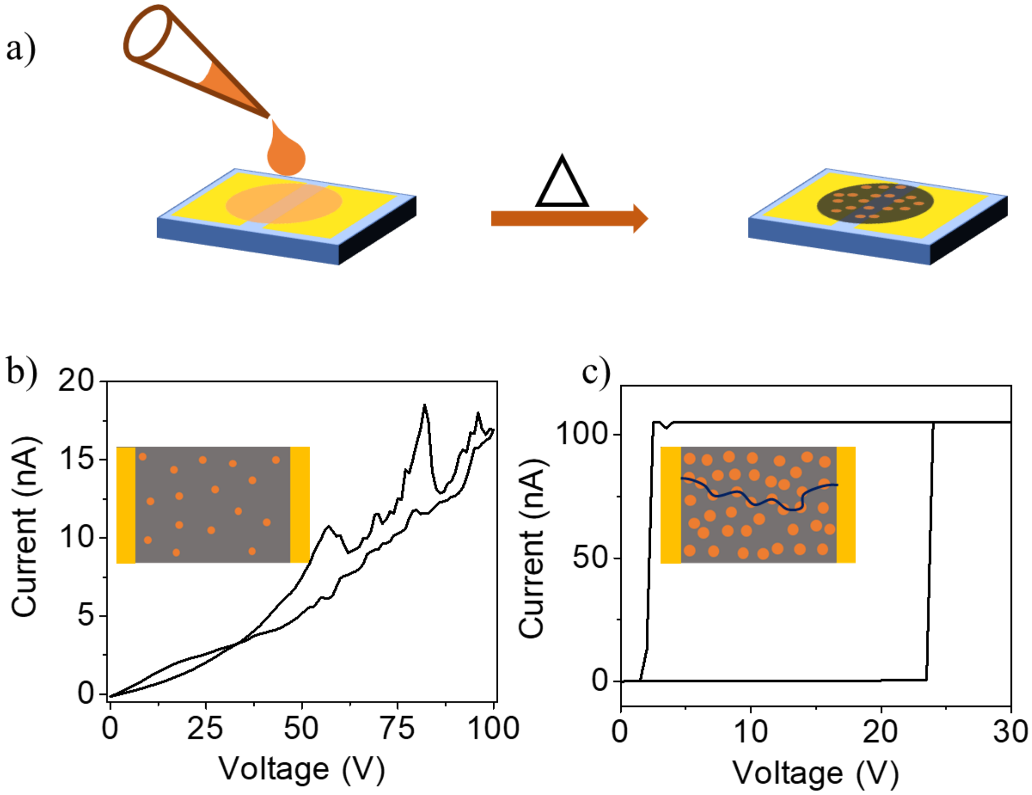

Figure IV.1: Device fabrication. a) Schematic illustration of device fabrication. b) Electrical forming process showing no switching behavior observed in device thermalized at 200 °C. c) Resistance switching observed in the device thermalized at 230 °C. Inset shows the schematic representation of preferential filament path formed during the process.

typical forming process was then performed on this device by sweeping the voltage from 0-100 V with a set current compliance of 100 nA for damage protection. From Figure IV.1b, it can be noted that the device did not show resistance switching behavior even for sweeping till 100 V, suggesting that the thermolysis was unsuccessful in producing sufficient nanoparticle/percolation density required for resistance switching. Another device was fabricated by increasing the thermolysis temperature to 230 °C while monitoring the resistance at intervals. At around 50 mins of annealing, the device showed resistance of ~10 MΩ indicating sufficient nucleation of Pd nanoparticles. The formation of these nanoparticles is further confirmed by the forming process, and Figure IV.1c shows that switching was observed at ~24 V. Also, it can be noted from the forming I-V curve that while sweeping, the device current drops before reaching 0 V, which is an indication of the short-term switching behavior.

To study the potential of the formed device to emulate synaptic actions, it was subjected to further electrical characterisation. Figure IV.2a shows the I-V switching behavior of the device. The forming process facilitates the preferential path for filament formation and thus helps optimize the switching voltage. Observing the I-V sweeps more carefully, a drop in the current value before reaching back to 0 V suggests evidence of short-term conductance retention. To investigate this short-term dynamic, pulsed signals were applied, which are more analogs to the bio-neural signals. Figure IV.2b shows a single pulse of 10 V amplitude, 300 ms width with a 5 μA current compliance, and a background reading voltage of 10 mV applied to the device. The figure shows that the device switches to a high conducting state while applying the pulse and remained in that state even after the pulse was stopped for ~30 s and then dropped back to the initial state, thus emulating STP. In a general psychological

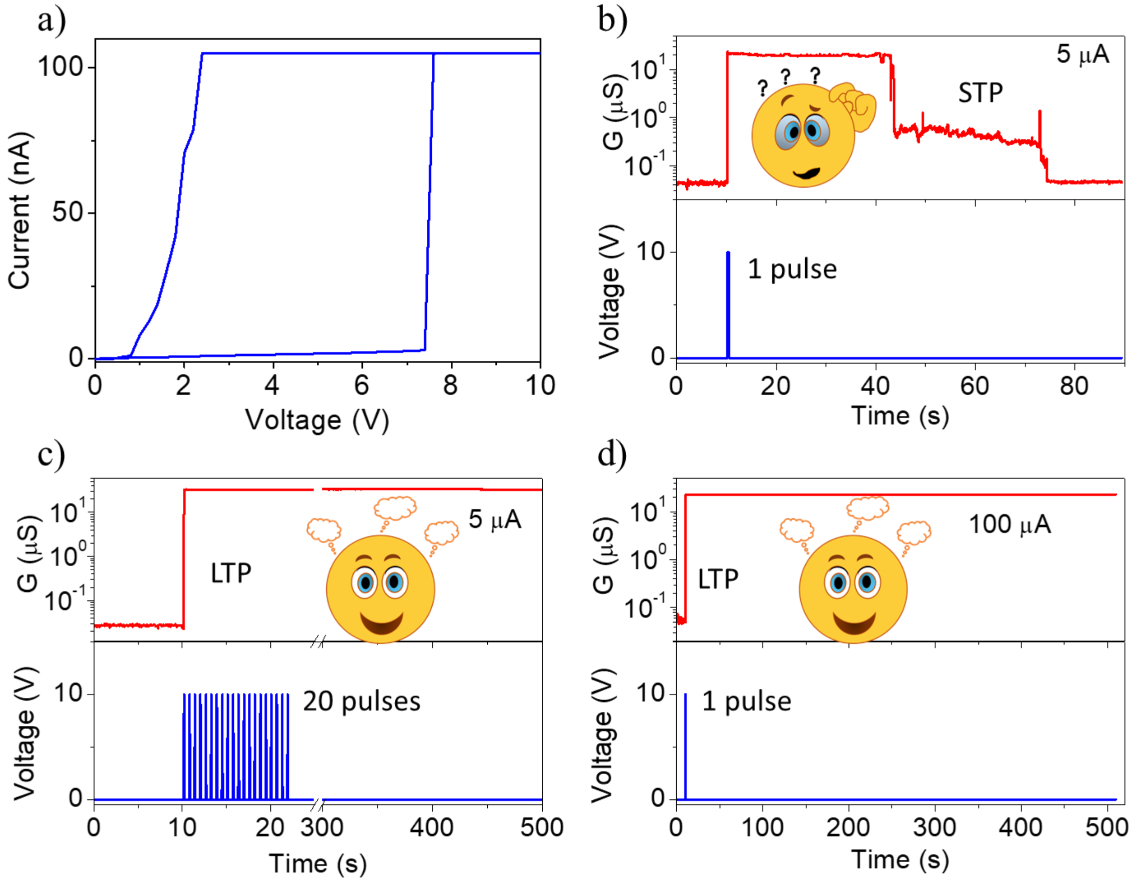

Figure IV.2: Synaptic behavior emulated in device thermalized at 230 °C. a) I-V sweep shows the switching behavior. b) STP is emulated with a single pulse of 10 V, 300 ms width, and 5 μA current compliance, while c) LTP is emulated with 20 pulses showing rehearsal-based learning. d) Increasing the compliance to 100 μA shows LTP behavior for a single pulse signal.

observation, reviving the learning event creates long-lasting and robust memory. This rehearsal event can be electrically stimulated by increasing the number of pulses. Figure IV.2c shows that while increasing the pulse number to 20, as a rehearsal event, the conductance state was retained for more than 500 s, thus emulating LTP. Along with rehearsal, often current compliance is also used to realize STP to LTP transition. Here increasing the compliance to 100 µA resulted in LTP emulation for a single pulse/learning event shown in Figure IV.2d.

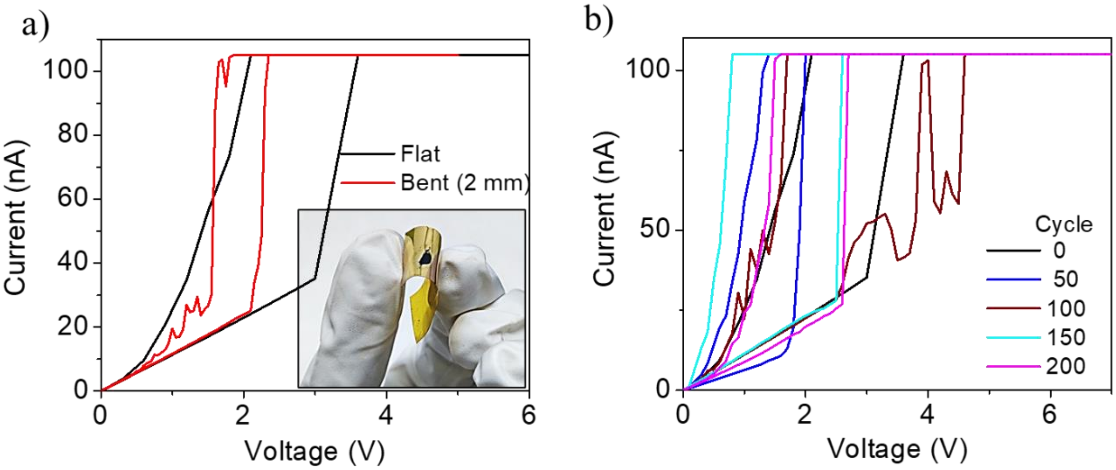

Figure IV.3: Flexible synaptic device. a) I-V characteristics of the device in flat and 2 mm bent state. Inset shows a digital photograph of the flexible device. b) I-V characteristics over 200 cycles show a good bending capability of the device.

With current technology advancing towards flexible electronics, it is highly demanding to fabricate compatible flexible neuromorphic devices. Given the organic matrix and metal nanoparticles filled in them, the Pd thiolate device is more suitable to exhibit flexible nature. The precursor was drop coated on a Kapton tape with prefabricated Au gap electrodes to investigate the device flexibility aspect. Thermolysis at 230 °C was performed as discussed previously, followed by the electrical forming process. A digital photograph of the flexible device is shown in the inset of Figure IV.3a. I-V characteristics of the flexible device in flat and 2 mm (bending radius) bent state is shown in the figure. Remarkably, the switching behavior was observed even in the bent state. Further, to study the device bending stability, over 200 bending cycles were performed, and I-V switching was observed. From Figure IV.3b, device stability while bending was commendable. One of the essential aspects of a flexible device is to maintain an active conductance state while bending. To investigate this,

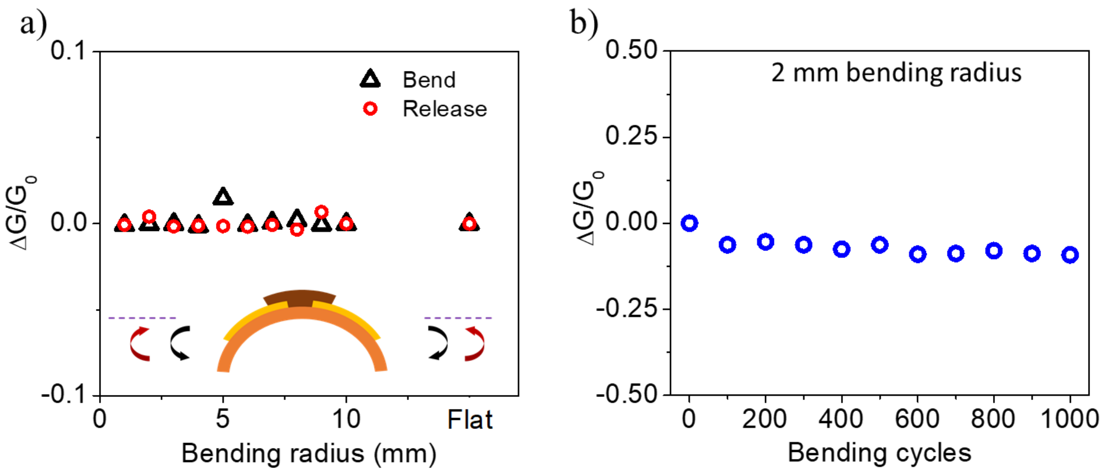

Figure IV.4: Bending test. a) Conductance variation while bending and releasing b) Conductance retention over 1000 bending cycles shows robust bending stability of the device.

the device was switched to a high conductance state via LTP pulse configuration. Later, to inspect the conductance state stability, the device was bent from a flat state to a 1 mm bending radius. Excitingly, there was no significant change in the conductance value during bending, as shown in Figure IV.4a. The device was also returned to the flat position in steps, and a stable conductance was seen throughout. Besides, the device was subjected to over 1000 bending cycles with a 2 mm bending radius, and no significant conductance change was observed, suggesting superior bending stability of the flexible device as shown in Figure IV.4b. The excellent bending stability achieved may be attributed to the strain relaxation to the organic matrix while bending. More importantly, synaptic actions such as STP and LTP

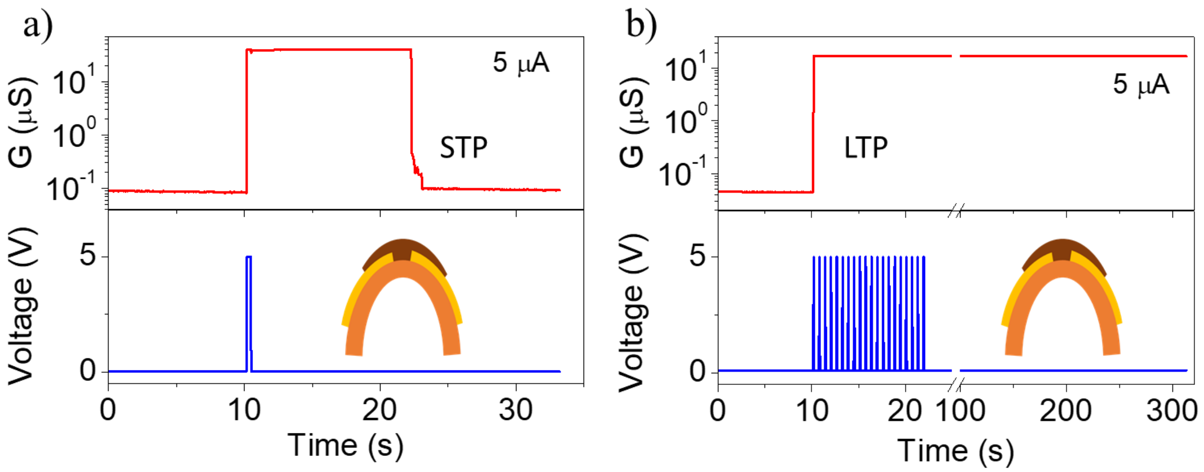

Figure IV.5: Synaptic behavior in a bent position. Rehearsal based STP (1 pulse) to LTP (20 pulses) transition shown in the device in 2 mm bent position. Pulse configuration: 5 V amplitude with 300 ms width and interval and set current compliance of 5 µA.

were also emulated while the device was bent to 2 mm bending radius, as shown in Figure IV.5.

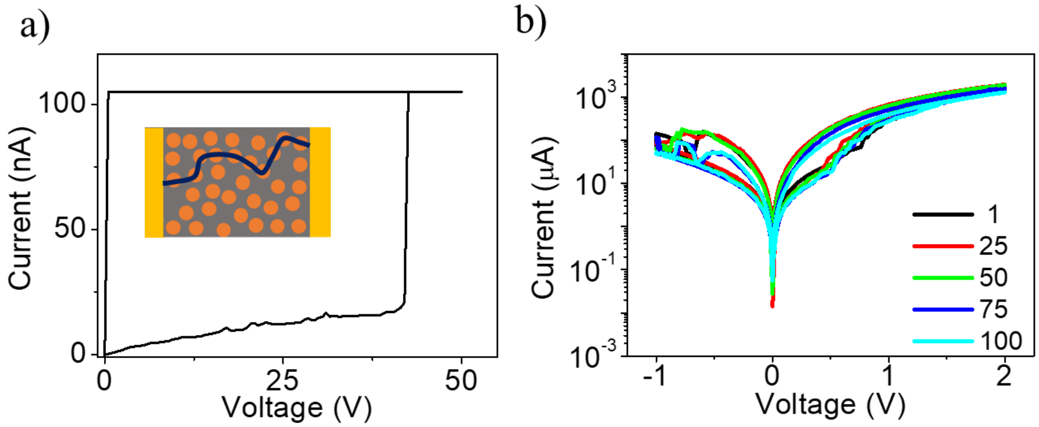

Figure IV.6: Studying the switching behavior of the device thermalized at 250 °C. a) Typical forming process. b) Bipolar I-V dual sweep cycles showing the excellent reproducibility interms of conductance switching.

To study the influence of higher thermolysis temperature, another fresh substrate was coated with Pd thiolate and subjected to thermolysis at 250 °C. While monitoring, a resistance of ~10 MΩ was achieved within 5 min. Later the device was subjected to a typical forming process, as shown in Figure IV.6a. It can be noted that the device switched to a high conducting state and retained the switched state, until it reached back to 0 V, suggesting long-term memory retention. To investigate the device ability in mimicking synaptic actions, this device was subjected to further electrical measurements. Figure IV.6b shows the bipolar I-V sweep characteristics, which displays typical resistive switching behavior that is stable

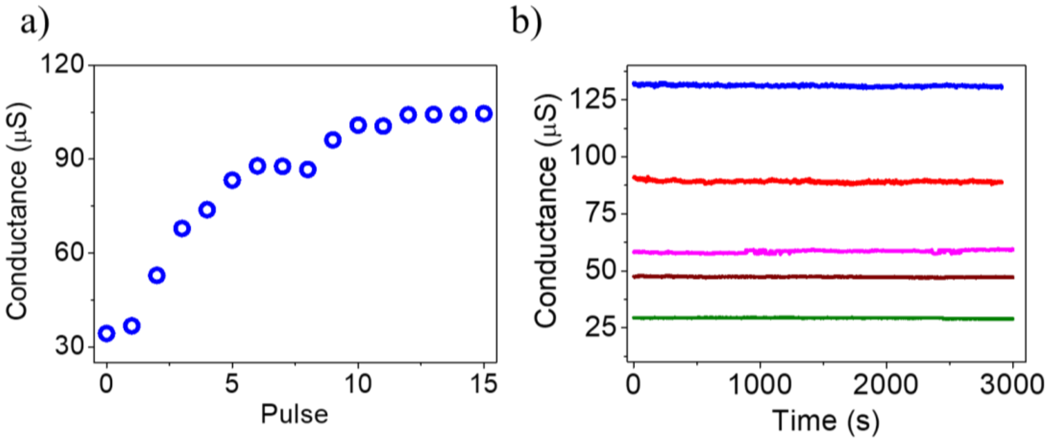

Figure IV.7: a) Spike number dependent plasticity (SNDP). b) Stable multileve conductance states.

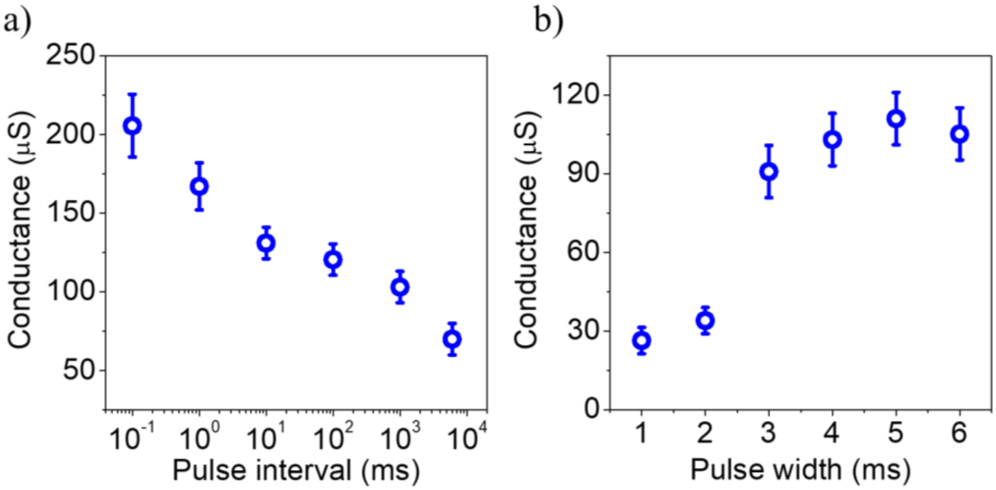

Figure IV.8: a) Spike-frequency dependent plasticity (SFDP) and b) Spike-duration dependent plasticity (SDDP).

over 100 cycles. In biosystems, reviving the information repeatedly will increase the synaptic weight/memory strength known as potentiation. Figure IV.7a shows that with increasing the pulse numbers, device conductance increases resembling synaptic potentiation. Interestingly, these conductance states were stable over 3000 s as shown in Figure IV.7b, displaying the device's multilevel conductance switching ability. Further, SFDP and SDDP were also demonstrated, which is shown in Figure IV.8. Thermolyzing at 250 °C resulted in a more conducting system as observed in low on/off ratio and emulation of only long-term memory in the device.

Retention of the memory state is another essential requirement in any data storage application. From Figure IV.9a, it is found that the conductance was highly stable over 20

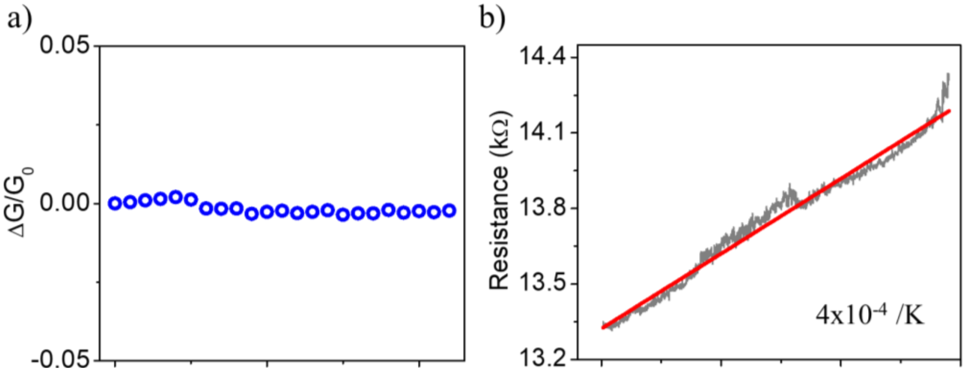

Figure IV.9: a) Conductance retention of the device over 20 days with no significant variation. b) Temperature-dependent resistance measurement of the device in low resistance state (LRS) showing the metallic nature of the conducting filament.

days in ambient. Temperature-dependent resistance measurement in the high conducting state revealed the conducting filament's metallic nature, as shown in Figure IV.9b. The calculated TCR was found to be ~4×10^{-4} K^{-1}, lower than that of the bulk system which is expected for the disordered connection.

IV.5 Conclusions

A simple solution-based fabrication process was developed for fabricating neuromorphic devices. Synaptic behaviors were observed in a device fabricated at 230 °C, and essential synaptic functions such as STP and LTP are demonstrated. In contrast, heating at 250 °C resulted in a resistive switching device, showing different SPDP. Moreover, the device showed multilevel conducting states, which were stable for over 3000 s. The device fabrication was extended to a flexible substrate using a Kapton tape, successfully. The device's excellent bending ability was demonstrated by bending over 1000 cycles and up to 1 mm bending radius.

References

[1] Q. Wan, M. T. Sharbati, J. R. Erickson, Y. Du, and F. Xiong, *Emerging Artificial Synaptic Devices for Neuromorphic Computing*, Adv. Mater. Technol. (2019).

[2] Y. Zhang, Z. Wang, J. Zhu, Y. Yang, M. Rao, W. Song, Y. Zhuo, X. Zhang, M. Cui, L. Shen, R. Huang, and J. Joshua Yang, *Brain-Inspired Computing with Memristors: Challenges in Devices, Circuits, and Systems*, Appl. Phys. Rev. (2020).

[3] Y. Yang, B. Chen, and W. D. Lu, *Memristive Physically Evolving Networks Enabling the Emulation of Heterosynaptic Plasticity*, Adv. Mater. (2015).

[4] T. Ohno, T. Hasegawa, T. Tsuruoka, K. Terabe, J. K. Gimzewski, and M. Aono, *Short-Term Plasticity and Long-Term Potentiation Mimicked in Single Inorganic Synapses*, Nat. Mater. (2011).

[5] C. Zheng, Y. Liao, Z. Xiong, Y. Zhou, and S. T. Han, *Mimicking the Competitive and Cooperative Behaviors with Multi-Terminal Synaptic Memtransistors*, J. Mater. Chem. C (2020).

[6] Z. Wang, S. Joshi, S. E. Savel'ev, H. Jiang, R. Midya, P. Lin, M. Hu, N. Ge, J. P. Strachan, Z. Li, Q. Wu, M. Barnell, G. L. Li, H. L. Xin, R. S. Williams, Q. Xia, and J. J. Yang, *Memristors with Diffusive Dynamics as Synaptic Emulators for Neuromorphic Computing*, Nat. Mater. (2017).

[7] S. G. Hu, Y. Liu, Z. Liu, T. P. Chen, Q. Yu, L. J. Deng, Y. Yin, and S. Hosaka, *Synaptic Long-Term Potentiation Realized in Pavlov's Dog Model Based on a NiOx-Based Memristor*, J.

Appl. Phys. (2014).

[8] M. Zhang, Z. Fan, X. Jiang, H. Zhu, L. Chen, Y. Xia, J. Yin, X. Liu, Q. Sun, and D. W. Zhang, *MoS2-Based Charge-Trapping Synaptic Device with Electrical and Optical Modulated Conductance*, Nanophotonics (2020).

[9] C. Lutz, T. Hasegawa, and T. Chikyow, *Ag_2S Atomic Switch-Based “tug of War” for Decision Making*, Nanoscale (2016).

[10] M. Kumar, D. K. Ban, S. M. Kim, J. Kim, and C. P. Wong, *Vertically Aligned WS2 Layers for High-Performing Memristors and Artificial Synapses*, Adv. Electron. Mater. (2019).

[11] M. Xiao, T. Yeow, V. H. Nguyen, D. Muñoz-Rojas, K. P. Musselman, W. W. Duley, and Y. N. Zhou, *Ultrathin TiOx Interface-Mediated ZnO-Nanowire Memristive Devices Emulating Synaptic Behaviors*, Adv. Electron. Mater. (2019).

[12] Y. Shi, X. Liang, B. Yuan, V. Chen, H. Li, F. Hui, Z. Yu, F. Yuan, E. Pop, H. S. P. Wong, and M. Lanza, *Electronic Synapses Made of Layered Two-Dimensional Materials*, Nat. Electron. (2018).

[13] S. Ham, M. Kang, S. Jang, J. Jang, S. Choi, T. W. Kim, and G. Wang, *One-Dimensional Organic Artificial Multi-Synapses Enabling Electronic Textile Neural Network for Wearable Neuromorphic Applications*, Sci. Adv. (2020).

[14] Y. Lee, J. Y. Oh, W. Xu, O. Kim, T. R. Kim, J. Kang, Y. Kim, D. Son, J. B. H. Tok, M. J. Park, Z. Bao, and T. W. Lee, *Stretchable Organic Optoelectronic Sensorimotor Synapse*, Sci. Adv. (2018).

[15] T. Y. Wang, Z. Y. He, L. Chen, H. Zhu, Q. Q. Sun, S. J. Ding, P. Zhou, and D. W. Zhang, *An Organic Flexible Artificial Bio-Synapses with Long-Term Plasticity for Neuromorphic Computing*, Micromachines (2018).

[16] Y. Van De Burgt, A. Melianas, S. T. Keene, G. Malliaras, and A. Salleo, *Organic Electronics for Neuromorphic Computing*, Nature Electronics (2018).

[17] D. H. Kang, J. H. Kim, S. Oh, H. Y. Park, S. R. Dugasani, B. S. Kang, C. Choi, R. Choi, S. Lee, S. H. Park, K. Heo, and J. H. Park, *A Neuromorphic Device Implemented on a Salmon-DNA Electrolyte and Its Application to Artificial Neural Networks*, Adv. Sci. (2019).

[18] H. L. Park, Y. Lee, N. Kim, D. G. Seo, G. T. Go, and T. W. Lee, *Flexible Neuromorphic Electronics for Computing, Soft Robotics, and Neuroprosthetics*, Adv. Mater. (2020).

[19] G. Zhong, M. Zi, C. Ren, Q. Xiao, M. Tang, L. Wei, F. An, S. Xie, J. Wang, X. Zhong, M. Huang, and J. Li, *Flexible Electronic Synapse Enabled by Ferroelectric Field Effect Transistor for Robust Neuromorphic Computing*, Appl. Phys. Lett. (2020).

[20] L. Q. Zhu, C. J. Wan, P. Q. Gao, Y. H. Liu, H. Xiao, J. C. Ye, and Q. Wan, *Flexible Proton-Gated Oxide Synaptic Transistors on Si Membrane*, ACS Appl. Mater. Interfaces (2016).

[21] J. Zhou, C. Wan, L. Zhu, Y. Shi, and Q. Wan, *Synaptic Behaviors Mimicked in Flexible Oxide-Based Transistors on Plastic Substrates*, IEEE Electron Device Lett. (2013).

[22] Y. Zhao, S. Dai, Y. Chu, X. Wu, and J. Huang, *A Flexible Ionic Synaptic Device and Diode-Based Aqueous Ion Sensor Utilizing Asymmetric Polyelectrolyte Distribution*, Chem. Commun. (2018).

[23] T. Y. Wang, J. L. Meng, M. Y. Rao, Z. Y. He, L. Chen, H. Zhu, Q. Q. Sun, S. J. Ding, W. Z. Bao, P. Zhou, and D. W. Zhang, *Three-Dimensional Nanoscale Flexible Memristor Networks with Ultralow Power for Information Transmission and Processing Application*, Nano Lett. (2020).

[24] H. Wan, Y. Cao, L. W. Lo, J. Zhao, N. Sepúlveda, and C. Wang, *Flexible Carbon Nanotube Synaptic Transistor for Neurological Electronic Skin Applications*, ACS Nano (2020).

[25] L. Li, Y. Shao, X. Wang, X. Wu, W. J. Liu, D. W. Zhang, and S. J. Ding, *Flexible Femtojoule Energy-Consumption In-Ga-Zn-O Synaptic Transistors with Extensively Tunable Memory Time*, IEEE Trans. Electron Devices (2020).

[26] T. Y. Wang, J. L. Meng, Z. Y. He, L. Chen, H. Zhu, Q. Q. Sun, S. J. Ding, P. Zhou, and D. W. Zhang, *Room-Temperature Developed Flexible Biomemristor with Ultralow Switching Voltage for Array Learning*, Nanoscale (2020).

[27] W. Xiong, L. Q. Zhu, C. Ye, Z. Y. Ren, F. Yu, H. Xiao, Z. Xu, Y. Zhou, H. Zhou, and H. L. Lu, *Flexible Poly(Vinyl Alcohol)–Graphene Oxide Hybrid Nanocomposite Based Cognitive Memristor with Pavlovian-Conditioned Reflex Activities*, Adv. Electron. Mater. (2020).

[28] C. Zhang, Y. T. Tai, J. Shang, G. Liu, K. L. Wang, C. Hsu, X. Yi, X. Yang, W. Xue, H. Tan, S. Guo, L. Pan, and R. W. Li, *Synaptic Plasticity and Learning Behaviours in Flexible Artificial Synapse Based on Polymer/Viologen System*, J. Mater. Chem. C (2016).

[29] Y. H. Liu, L. Q. Zhu, P. Feng, Y. Shi, and Q. Wan, *Freestanding Artificial Synapses Based on Laterally Proton-Coupled Transistors on Chitosan Membranes*, Adv. Mater. (2015).

[30] S. E. Root, S. Savagatrup, A. D. Printz, D. Rodriquez, and D. J. Lipomi, *Mechanical Properties of Organic Semiconductors for Stretchable, Highly Flexible, and Mechanically Robust Electronics*, Chemical Reviews (2017).

[31] S. G. Hu, Y. Liu, T. P. Chen, Z. Liu, Q. Yu, L. J. Deng, Y. Yin, and S. Hosaka, *Emulating the Ebbinghaus Forgetting Curve of the Human Brain with a NiO-Based Memristor*, Appl. Phys. Lett. (2013).

[32] T. D. Dongale, P. S. Pawar, R. S. Tikke, N. B. Mullani, V. B. Patil, A. M. Teli, K. V. Khot, S. V. Mohite, A. A. Bagade, V. S. Kumbhar, K. Y. Rajpure, P. N. Bhosale, R. K. Kamat, and P. S. Patil, *Mimicking the Synaptic Weights and Human Forgetting Curve Using Hydrothermally Grown Nanostructured CuO Memristor Device*, J. Nanosci. Nanotechnol. (2018).

[33] Y. Abbas, Y. R. Jeon, A. S. Sokolov, S. Kim, B. Ku, and C. Choi, *Compliance-Free, Digital SET and Analog RESET Synaptic Characteristics of Sub-Tantalum Oxide Based Neuromorphic Device*, Sci. Rep. (2018).

[34] B. Radha, A. A. Sagade, and G. U. Kulkarni, *Metal-Organic Molecular Device for Non-Volatile Memory Storage*, Appl. Phys. Lett. (2014).

Chapter VA

Emulating the Ebbinghaus Forgetting Curve in an Optoelectronic Neuromorphic Device *

Summary

An optoelectronic neuromorphic device has been fabricated using a simple solution-based technique. Essential synaptic plasticity such as STP, LTP, and SPDP was emulated using electrical and optical stimuli. The decaying nature of the device current resembles the famous Ebbinghaus forgetting curve, which describes how information is lost in the human brain over time. The characteristic relaxation constant was tuned with input stimulus parameters similar to biosystems.

VA.1 Introduction

The human brain is gifted with an efficient memory management system. Not all the memories stay in the brain eternally, thus classified into sensory memory (SM), short-term memory (STM), and long-term memory (LTM) [1]. Information received from the external world is processed and stored in the brain, tend to decay with time [2]. The information loss significantly depends on several factors such as the rehearsal, frequency of learning, and other parameters. This information loss was formulated by Hermann Ebbinghaus in 1885 [3]. Quantitatively the information loss is expressed by the following equation [4].

$$P = \Delta EPSC/\Delta EPSC(0) = \exp\,(-t/\tau)^{\beta}$$

Where P is the probability/possibility of recall, t is time, τ is the characteristic relaxation time, and β is a stretch index ranging from 0 to 1.

Brain-inspired neuromorphic devices are the future of hardware-based artificial intelligence. These devices aim to mimic the synaptic functions of the human brain. Different types of materials, starting from metal oxide systems to polymers, have been explored in the literature to fabricate such devices [5–9]. Of them, vacancy- and trap-based neuromorphic devices tend to exhibit the decaying nature of their current/conductance [10–13]. Although

---

*Part of this Chpter is from: ACS Appl. Electron. Mater., **1**, 577 (2019).

they are best suited to emulate the Ebbinghaus forgetting curve, they are less discussed in this context. Earlier Aono et al. demonstrated the forgetting curve in an inorganic system based on Ag_2S atomic switch using STM tip [1]. Later, Hosaka et al. discussed in more detail the Ebbinghaus forgetting curve in a NiO-based device [14]. Similar discussion was then followed in other materials [15–17].

In devices, modulating synaptic plasticity is crucial to emulate several psychological behavioral patterns [18]. To accomplish this emulation, multi-electrode geometry is generally explored [19]. In contrast, an optoelectronic device that responds to both light and electrical signals, comes with advantages such as reducing the multi-electrode fabrication step [20].

VA.2 Scope of the present investigation

About 80% of the information is perceived through vision and is then processed by the human brain. Thus, optoelectronic neuromorphic devices have attracted a wide range of applications, including artificial visual systems. Most of the fabrication process involves complex techniques, and achieving both electrical and optical activation in devices is challenging. In the present investigation, a simple solution-based technique is explored for fabricating an optoelectronic neuromorphic device. Along with essential synaptic plasticity, the famous Ebbinghaus forgetting curve is also emulated. Often in literature, the trap assisted systems are suggested to mimic associative learning. In the present investigation, the issues associated with such measurements are discussed.

VA.3 Experimental details

Device Fabrication: Si (n type, (100), 3-9 Ω-cm) substrate was sonicated in acetone and IPA for 10 min, followed by RCA cleaning and dried under nitrogen. This substrate was immersed in a plating solution of 5 mM $HAuCl_4$ in HF for the desired time. Once the plating was done, the substrate was rinsed in DI water and dried under nitrogen. For electrical measurement, copper wire contacts were taken from the top and bottom sides using Ag paste.

Electrical Measurement: Keithley 2450 was used for electrical pulse measurement.

VA.4 Results and discussion

Schematic of the fabrication process is shown in Figure VA.1a. It is a simple process of electroless plating of Au on Si [21]. A clean n-type Si substrate was immersed in a petri dish containing a stoichiometric ratio of $HAuCl_4$ in HF. Thus, Au film got deposited on the Si surface by galvanic displacement. The FESEM image in Figure VA.1b shows granular nature of the deposited Au film, and the interface is clearly evident in the cross-sectional image (see inset). The deposition process led to the formation of a nanostructured surface and the roughness as measured using AFM was found to be ~12 nm (Figure VA.1c). The core level spectra in the Au 4f region (Figure VA.1d), contains besides Au^0 (83.7 eV), a feature related to gold silicide as well (84.1 eV) [21–23]. The formation of Au silicide at the interface during electroless deposition is well known in literature [22,24,25]. This study exploits the silicide interface as a p-type semiconducting junction (hereafter termed as Au/p-silicide/n-Si).

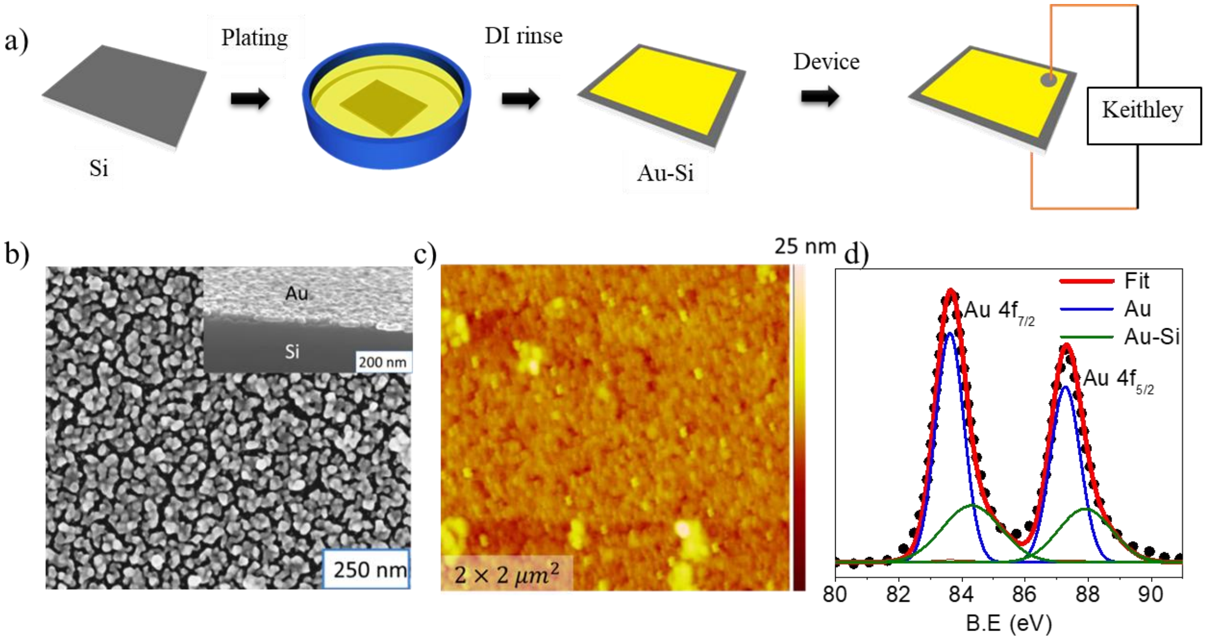

Figure VA.1: a) Schematic of the fabrication process. b) FESEM image of the grown Au film (inset: cross sectional image). c) AFM image of Au plated Si surface showing the granular morphology. d) Core level spectra in Au 4f region.

Since the device was fabricated using a solution-based process, one can expect trap states to be present at the interface. Evidence of these trap states can be observed by performing a simple dual I-V sweep. Figure VA.2a shows the dual sweep I-V characteristics of the fabricated Au-Si device in the dark. Interestingly, the device showed typical diode I-V

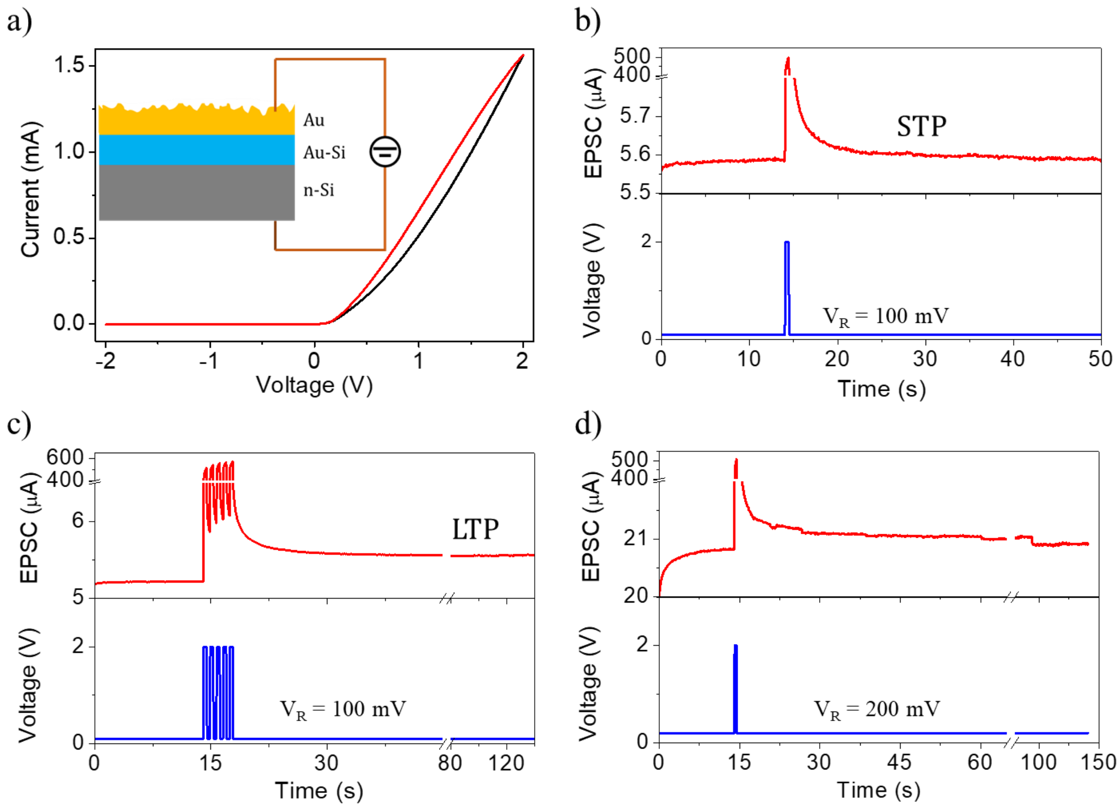

Figure VA.2: Synaptic activity. a) I-V characteristics of the device. Inset showing the schematic of device. b) STP emulated with single electrical pulse signal. c) LTP emulated with 5 electrical pulse signals. d) Increased reading voltage demonstrates the mood-dependent synaptic activity.

characteristics. Also, the presence of hysteresis is an indication of interfacial traps in the system. Using suitable electrical pulse signals, these traps can be explored to emulate different synaptic plasticity such as STP, LTP, SPDP, etc. To mimic pre-synaptic signaling condition, an electrical pulse signal of 2 V amplitude, 300 ms pulse width is applied to the device in the dark with a background reading voltage of 100 mV as shown in Figure VA.2b. It can be observed that during the application of the pulse, the device current increased, and when the pulse was withdrawn, the current slowly decreased to its original state to emulating excitatory post-synaptic current (EPSC) as seen in the biological synapse [26]. The EPSC retention was up to 30 s before returning to its original value after the pulse, thus depicting STP. From the psychological observation, it is known that increased rehearsal will increase memory retention and hence can lead to LTP, where the memory can be retained for several minutes to days. To emulate this, 5 pulses of 2 V amplitude with 300 ms width as well as interval was applied to the device, and the current was measured with time (Figure

VA.2c). As seen from the figure, an increased number of pulses resulted in increased EPSC retention beyond 150 s, thus emulating LTP. Another interesting behavior commonly observed is the mood-based learning/memory activity, where under a good mood, memory retention is longer. Here to emulate mood in the device, background reading voltage is varied while applying the pulse signal. During 100 mV reading voltage, which can be considered as neutral mood, the EPSC retention was around 30 s, as seen in Figure VA.2b. When the reading voltage was increased to 200 mV to represent good mood (Figure VA.2d), memory retention exceeded 90 s, thus emulating mood-based learning.

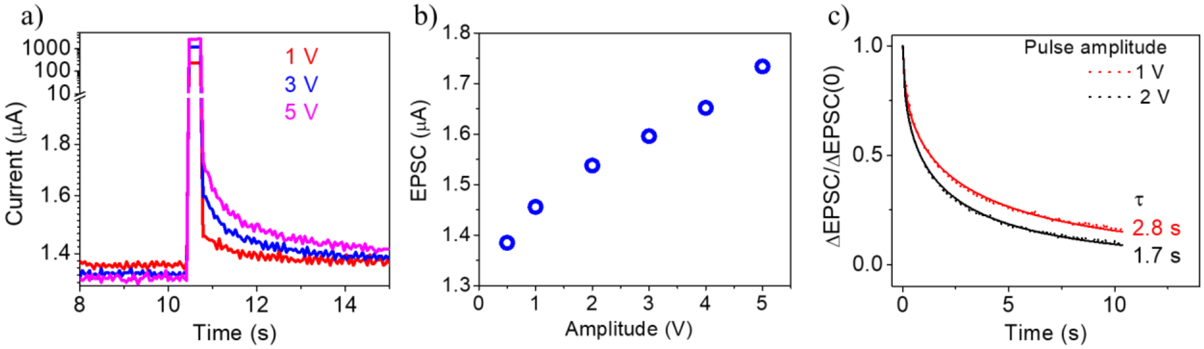

Figure VA.3: Electrical pulse. a) Influence of spike amplitude. b) EPSC variation with amplitude. c) Influence of spike amplitude on the forgetting curve (decay constant, τ is shown).

The EPSC signal showed a decay behavior that closely resembles the forgetting curve of human memory. According to Ebbinghaus, information stored in the brain is lost very quickly in the initial stage of learning, and it can be influenced by several factors involved during learning activity, as discussed earlier [4]. To study these influence, different pulse configurations were applied to the device. Firstly, the pulse amplitude was varied from 1 to 5 V, and the EPSC was measured as shown in Figure VA.3a. As seen from the figure, the EPSC strength increased with increasing signal amplitude, also shown in Figure VA.3b. Fitting the

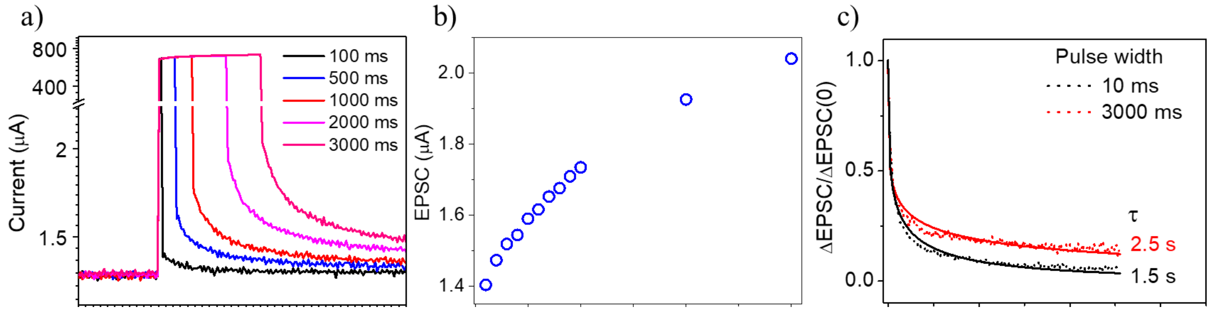

Figure VA.4: a) Influence of spike width. b) EPSC variation with width. c) Influence of spike width on the forgetting curve (decay constant, τ is shown).

decay current with the Ebbinghaus forgetting equation showed that the increased amplitude increased the decay constant, indicating slower decay of the information as shown in Figure VA.3c. The characteristics relaxation constant was in seconds which is similar to the value observed in biosystems [27]. Besides, spike duration and rehearsal-based effects were also studied. In the case of spike duration, a pulse signal of 2 V amplitude was applied with varying width in the range of 100-3000 ms, as shown in Figure VA.4a. EPSC modulation and decay constant in the forgetting curve are shown in Figure VA.4b and Figure VA.4c, respectively. Similarly, the pulse number is varied from 1-100, and corresponding behaviors are shown in Figure VA.5.

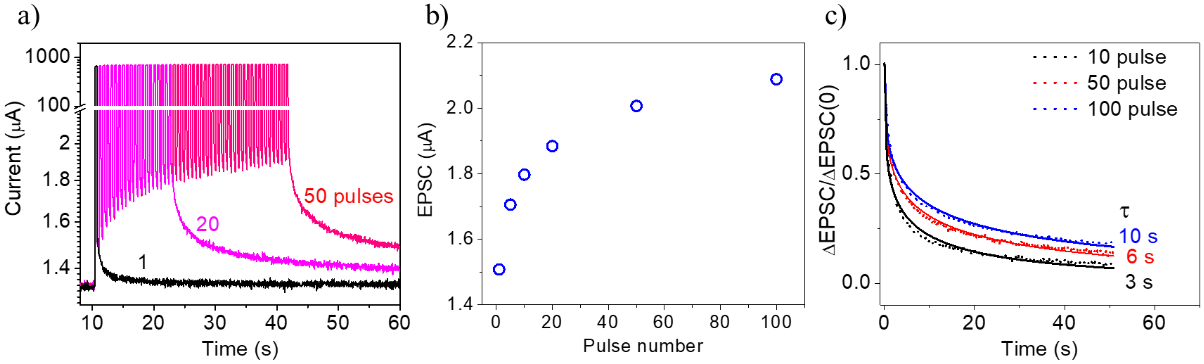

Figure VA.5: a) Influence of spike number. b) EPSC variation with spike number. c) Influence of spike number on the forgetting curve (decay constant, τ is shown).

Interestingly, the junction was responding to optical signal showing photodetection action. Thus, optical signals were also experimented as input stimuli to emulate synaptic functions. At first, optical pulse signals with varying pulse duration (1-30 s) was applied to the device biased at -2 V (photodiode region). Figure VA.6a,b showed that with increasing pulse width, the EPSC magnitude and the retention were increased, thus showing STP and LTP nature. Further, the EPSC decay was analyzed with the Ebbinghaus equation as shown in Figure VA.6c. The decay constant extracted for the fitting curve displayed that when illumination width increased from 5 s to 30 s, the decay constant increased from 3 s to 14 s, showing a strong influence of width on forgetting rate. Further, illumination was done for a longer duration, such as 5 min, and found that the device achieved permanent plasticity where the EPSC stayed above 40% even after 5000 s (Figure VA.6d). Optical pulse numbers varying from 1-10 were applied with 5 s width (ON time) and an interval (OFF time) for emulating rehearsal-based learning. Analogous to general observation, Figure VA.7 shows that EPSC

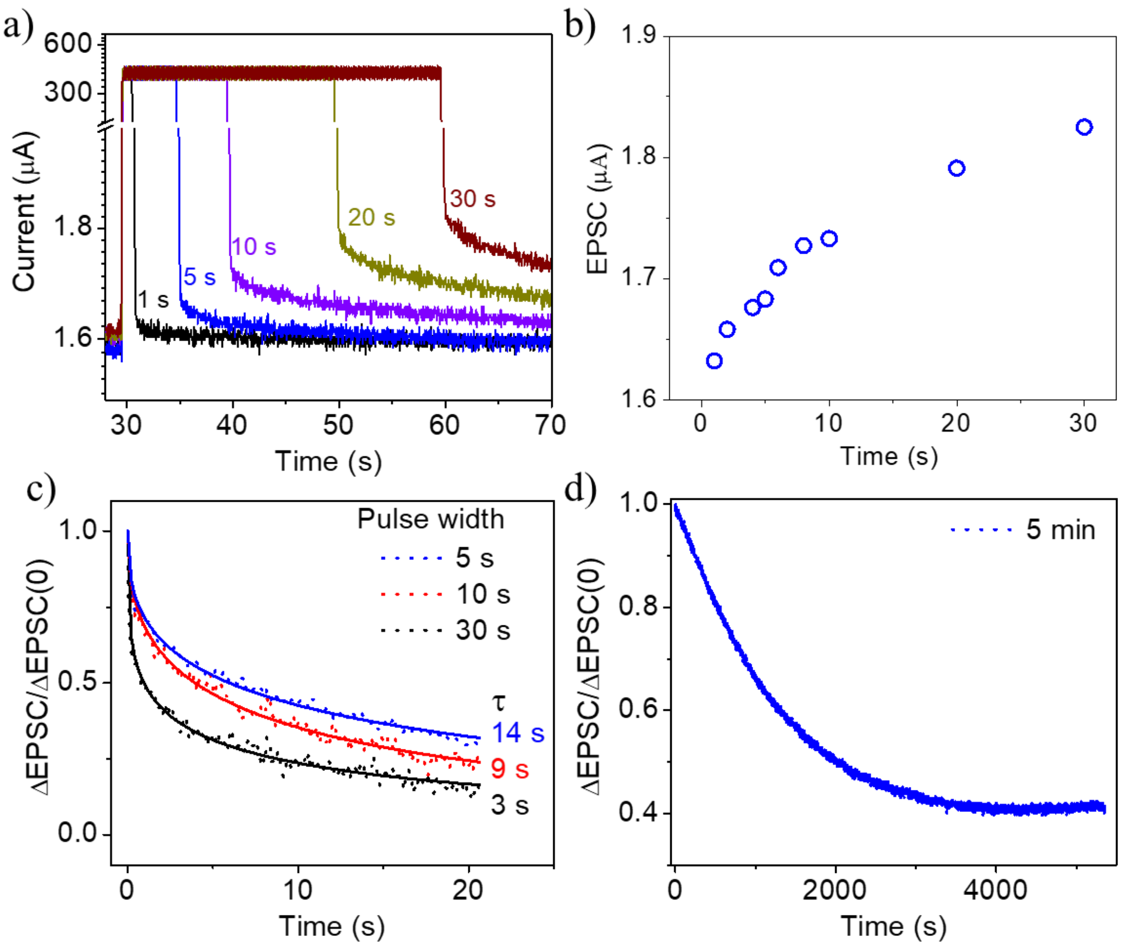

Figure VA.6: Optical pulse signaling. a) Influence of optical spike width. b) EPSC variation with width. c) Influence of spike width on the forgetting curve (decay constant, τ is shown). d) LTP is achieved by illuminating a single optical pulse of 5 min pulse width.

strength increased with increasing number of pulses and the decay constant increased from 0.2 s to 4 s. It is interesting to note that the device did not show any synaptic activity for 60

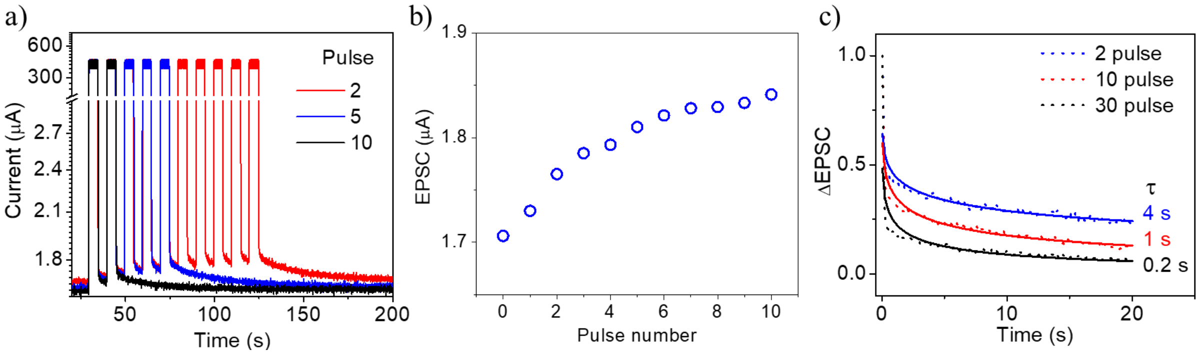

Figure VA.7: a) Influence of spike number. b) EPSC variation with spike number. c) Influence of spike number on the forgetting curve (decay constant, τ is shown).

s of light illumination when biased with 0 V, as shown in Figure VA.8. Thus, the device can still act as a photodetector.

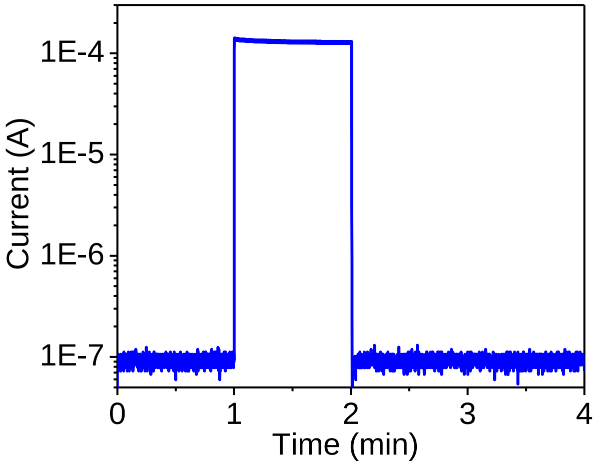

Figure VA.8: No synaptic action observed during the zero bias condition.

Multi-input synaptic devices possess the advantage of modulation of the synaptic plasticity without modifying the pre-synaptic input signal. To demonstrate this, a 20 pulse electrical signal of 2 V amplitude with 300 ms width and interval was applied to the device as a pre-synaptic signal, and EPSC was measured as shown in Figure VA.9a. Now to study the influence of modulatory signal, the light was illuminated along with the new set electrical signal. Interestingly, the EPSC strength was increased significantly, and the decay constant was found to be increased from 9 to 23 s showing a strong influence of the modulatory signal

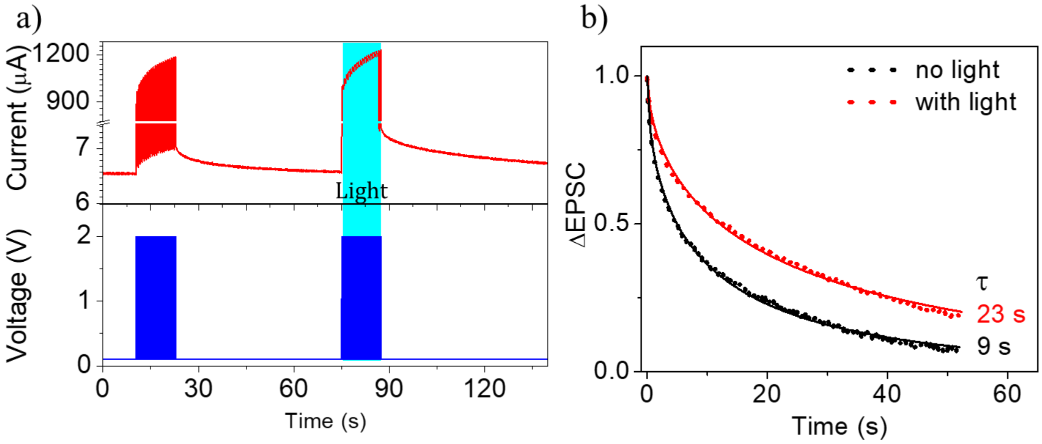

Figure VA.9: a) modulating the synaptic plasticity using both electrical and optical signals. b) Effect of modulating signal on the forgetting curve (decay constant, τ is shown).

(Figure VA.9b). Such modulation is useful in emulating higher-order behavior patterns like environment-dependent learning or memory activity.

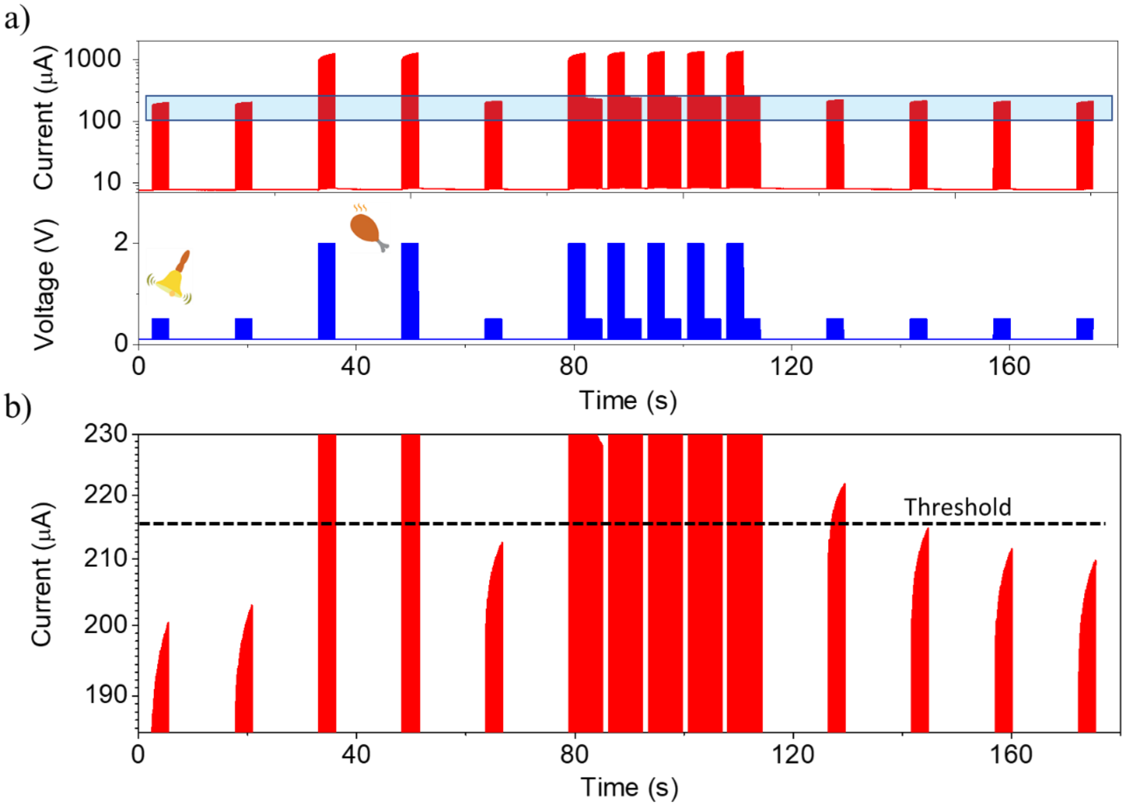

Figure VA.10: Classical conditioning. a) 2 V signal is used as a food signal and 0.5 V signal is used as a bell signal. While training, food and bell pulses were applied in succession. A magnified view of the highlighted region is shown in (b).

Classical conditioning is one of the complex learning activities that occurs in the brain, commonly known by Pavlov's dog experiment as previously discussed. It is highly challenging to emulate this cognition in neuromorphic devices. Several trap-based systems in the literature claim to emulate this classical conditioning with threshold current concept. Often these measurements are not carefully studied to validate the true association nature. Here, with detailed pulse sequences, issues related to mimicking such associations, in trap-based devices are discussed. Here, 2 V, 20 pulses is assigned as a food signal, and 0.5 V, 20 pulses as a bell signal (Figure VA.10a). First, a bell and food pulses are individually applied to the device in the dark to study the EPSC modulation. From this observation, a current threshold of 215 µA as salivation threshold is set since the bell pulse alone could not overcome this value. A training sequence is initiated by applying 5 sets of food and bell pulses together to create an association between these signals as typically done for such devices. Another strategy to define the training signal is to apply the combined food and bell strength as shown in Figure VA.11. In both cases, as expected, the bell pulse response measured post-training was above the salivation threshold, thus showing the association (Figure VA.10b, Figure VA.11b). Over-application of successive bell pulses without the reward system (food), the EPSC reduced below the salivation threshold, which is typically observed dissociation behavior. Here an important aspect to remember is the decaying nature of the device EPSC response. Hence applying a bell pulse on the decay tail leads to the enhanced EPSC overcoming the threshold. This is clarified by applying larger food pulses alone without the bell signal during training, as shown in Figure VA.12. It can be noted that a similar classical conditioning response can be achieved without any conditioning signal. Thus, such a trap assisted system may not be the right candidate for emulating complex associative learning activity. Besides, a detailed pulse sequence needs to be supported to validate the true association nature.

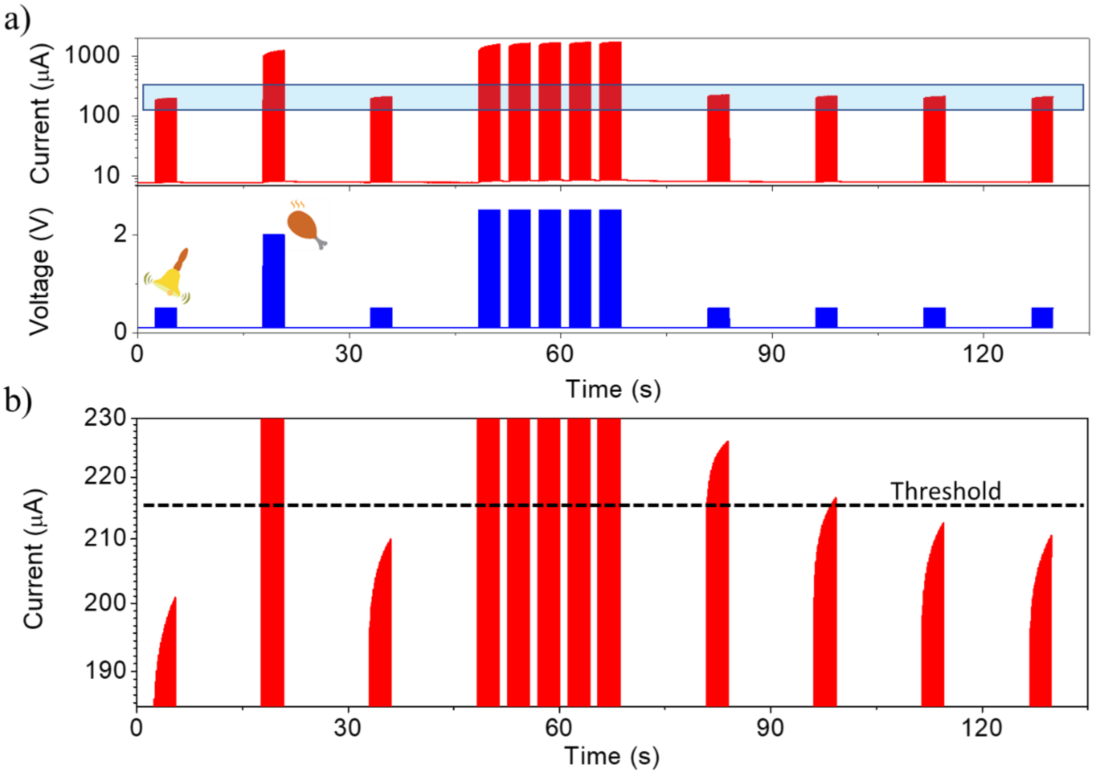

Figure VA.11: Classical conditioning. a) 2 V signal is used as a food signal and 0.5 V signal is used as a bell signal. While training, combined amplitude (2.5 V) of food and bell pulses were applied. A magnified view of the highlighted region is shown in (b).

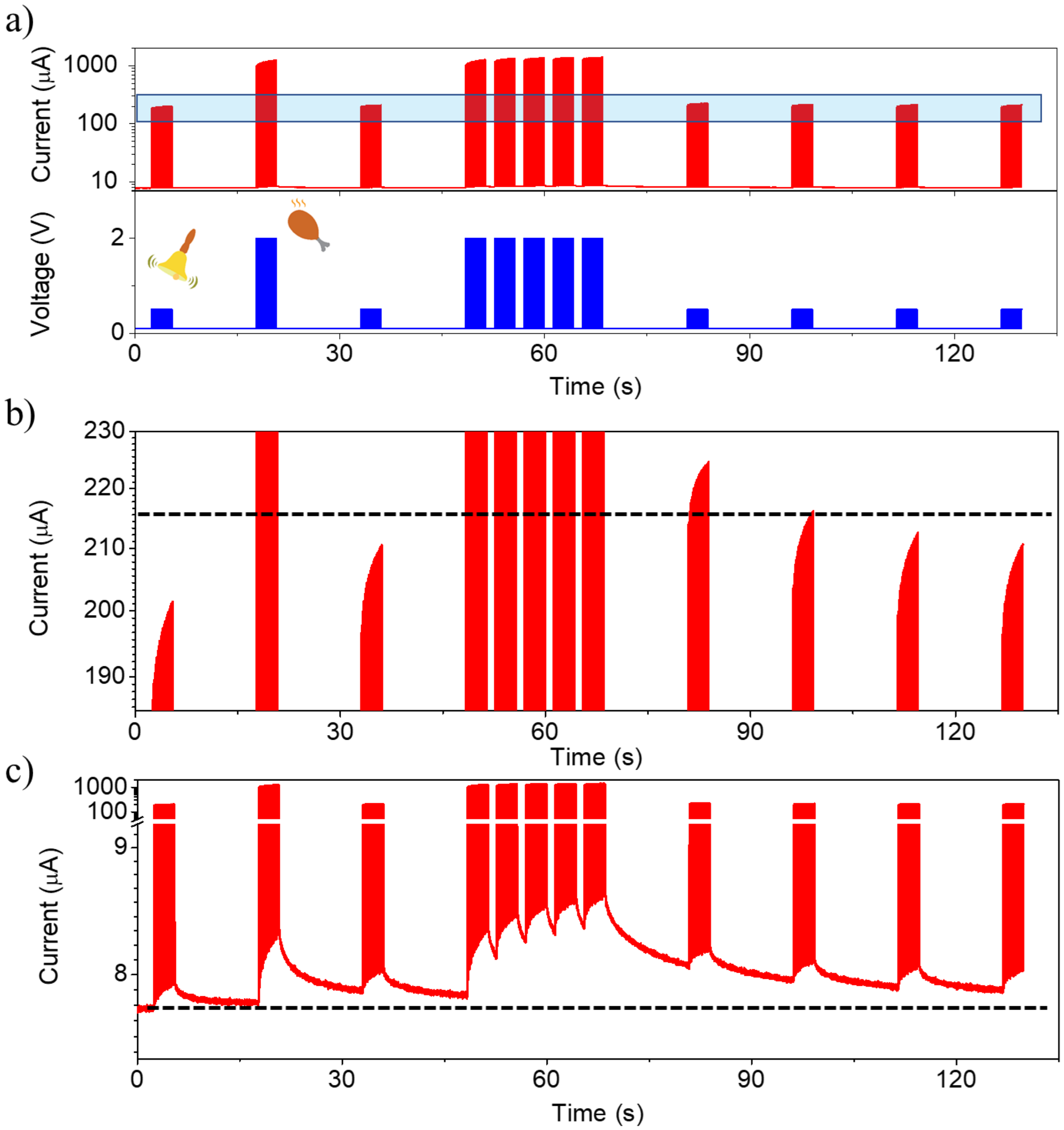

Figure VA.12: To verify the association, only food signals were applied during training (a). A magnified view of the highlighted region is shown in (b). It is observed that a similar classical conditioning response was achieved without a bell pulse during training, which suggests inaccurate associative learning. c) Decay nature of the EPSC during the pulsing.

VA.5 Conclusions

A simple solution-based technique is used to fabricate an optoelectronic neuromorphic device. Electroless deposition of Au on Si resulted in Silicide-Si junction exhibiting diode-like behavior. The presence of interfacial trap states was exploited to emulate synaptic functions using both electrical and optical pulses. Besides, the famous Ebbinghaus forgetting curve is also mimicked. Often overlooked associative learning in trap assisted system is also discussed. Modulation of synaptic plasticity using optical pulse is demonstrated.

References

[1] T. Ohno, T. Hasegawa, T. Tsuruoka, K. Terabe, J. K. Gimzewski, and M. Aono, *Short-Term Plasticity and Long-Term Potentiation Mimicked in Single Inorganic Synapses*, Nat. Mater. **10**, 591 (2011).

[2] J. M. J. Murre and J. Dros, *Replication and Analysis of Ebbinghaus' Forgetting Curve*, PLoS One **10**, e0120644 (2015).

[3] H. Ebbinghaus, *Memory: A Contribution to Experimental Psychology*, Ann. Neurosci. **20**, 155 (2013).

[4] S. G. Hu, Y. Liu, T. P. Chen, Z. Liu, Q. Yu, L. J. Deng, Y. Yin, and S. Hosaka, *Emulating the Ebbinghaus Forgetting Curve of the Human Brain with a NiO-Based Memristor*, Appl. Phys. Lett. **103**, 133701 (2013).

[5] N. K. Upadhyay, H. Jiang, Z. Wang, S. Asapu, Q. Xia, and J. Joshua Yang, *Emerging Memory Devices for Neuromorphic Computing*, Adv. Mater. Technol. **4**, 1800589 (2019).

[6] Q. Wan, M. T. Sharbati, J. R. Erickson, Y. Du, and F. Xiong, *Emerging Artificial Synaptic Devices for Neuromorphic Computing*, Adv. Mater. Technol. **4**, 1900037 (2019).

[7] J. Sun, Y. Fu, and Q. Wan, *Organic Synaptic Devices for Neuromorphic Systems*, J. Phys. D. Appl. Phys. **51**, 314004 (2018).

[8] H. L. Park, Y. Lee, N. Kim, D. G. Seo, G. T. Go, and T. W. Lee, *Flexible Neuromorphic Electronics for Computing, Soft Robotics, and Neuroprosthetics*, Adv. Mater. **32**, 1903558 (2020).

[9] S. H. Sung, D. H. Kim, T. J. Kim, I. S. Kang, and K. J. Lee, *Unconventional Inorganic-Based Memristive Devices for Advanced Intelligent Systems*, Adv. Mater. Technol. **4**, 1900080 (2019).

[10] S. Gao, G. Liu, H. Yang, C. Hu, Q. Chen, G. Gong, W. Xue, X. Yi, J. Shang, and R. W. Li, *An Oxide Schottky Junction Artificial Optoelectronic Synapse*, ACS Nano **13**, 2634 (2019).

[11] D. Li, C. Li, N. Ilyas, X. Jiang, F. Liu, D. Gu, M. Xu, Y. Jiang, and W. Li, *Color-Recognizing Si-Based Photonic Synapse for Artificial Visual System*, Adv. Intell. Syst. **2**, 2000107 (2020).

[12] J. Sun, S. Oh, Y. Choi, S. Seo, M. J. Oh, M. Lee, W. B. Lee, P. J. Yoo, J. H. Cho, and J. H. Park, *Optoelectronic Synapse Based on IGZO-Alkylated Graphene Oxide Hybrid Structure*, Adv. Funct. Mater. **28**, 1804397 (2018).

[13] L. Yin, W. Huang, R. Xiao, W. Peng, Y. Zhu, Y. Zhang, X. Pi, and D. Yang, *Optically Stimulated Synaptic Devices Based on the Hybrid Structure of Silicon Nanomembrane and Perovskite*, Nano Lett. **20**, 3378 (2020).

[14] Y. Abbas, A. S. Sokolov, Y. R. Jeon, S. Kim, B. Ku, and C. Choi, *Structural Engineering of*

Tantalum Oxide Based Memristor and Its Electrical Switching Responses Using Rapid Thermal Annealing, J. Alloys Compd. **759**, 44 (2018).

[15] H. K. Li, T. P. Chen, P. Liu, S. G. Hu, Y. Liu, Q. Zhang, and P. S. Lee, *A Light-Stimulated Synaptic Transistor with Synaptic Plasticity and Memory Functions Based on InGaZnOx-Al2O3 Thin Film Structure*, J. Appl. Phys. **119**, 244505 (2016).

[16] X.-B. Yin, R. Yang, K.-H. Xue, Z.-H. Tan, X.-D. Zhang, X.-S. Miao, and X. Guo, *Mimicking the Brain Functions of Learning, Forgetting and Explicit/Implicit Memories with SrTiO 3 -Based Memristive Devices*, Phys. Chem. Chem. Phys. **18**, 31796 (2016).

[17] Y. Yang, B. Chen, and W. D. Lu, *Memristive Physically Evolving Networks Enabling the Emulation of Heterosynaptic Plasticity*, Adv. Mater. **27**, 7720 (2015).

[18] R. A. John, F. Liu, N. A. Chien, M. R. Kulkarni, C. Zhu, Q. Fu, A. Basu, Z. Liu, and N. Mathews, *Synergistic Gating of Electro-Iono-Photoactive 2D Chalcogenide Neuristors: Coexistence of Hebbian and Homeostatic Synaptic Metaplasticity*, Adv. Mater. **30**, 1800220 (2018).

[19] S. Gao, G. Liu, H. Yang, C. Hu, Q. Chen, G. Gong, W. Xue, X. Yi, J. Shang, and R. W. Li, *An Oxide Schottky Junction Artificial Optoelectronic Synapse*, ACS Nano **13**, 2634 (2019).

[20] Bhuvana and G. U. Kulkarni, *Optimizing Growth Conditions for Electroless Deposition of Au Films On*, Bull. Mater. Sci. **29**, 505 (2006).

[21] L. Zhao, A. C. L. Siu, J. A. Petrus, Z. He, and T. L. Kam, *Interfacial Bonding of Gold Nanoparticles on a H-Terminated Si(100) Substrate Obtained by Electro- and Electroless Deposition*, J. Am. Chem. Soc. **129**, 5730 (2007).

[22] D. . Sarkar, S. Bera, S. Dhara, K. G. . Nair, S. . Narasimhan, and S. Chowdhury, *XPS Studies on Silicide Formation in Ion Beam Irradiated Au/Si System*, Appl. Surf. Sci. **120**, 159 (1997).

[23] L. Magagnin, R. Maboudian, and C. Carraro, *Gold Deposition by Galvanic Displacement on Semiconductor Surfaces: Effect of Substrate on Adhesion*, J. Phys. Chem. B **106**, 401 (2002).

[24] N. Ferralis, R. Maboudian, and C. Carraro, *Structure and Morphology of Annealed Gold Films Galvanically Displaced on the Si(111) Surface*, J. Phys. Chem. C **111**, 7508 (2007).

[25] C. R. Raymond, *LTP Forms 1, 2 and 3: Different Mechanisms for the "long" in Long-Term Potentiation*, Trends Neurosci. **30**, 167 (2007).

[26] D. C. Rubin, S. Hinton, and A. Wenzel, *The Precise Time Course of Retention*, J. Exp. Psychol. Learn. Mem. Cogn. **25**, 1161 (1999).

Chapter VB

A High-Performance Photodetector *

Summary

A simple solution-based method for fabricating high-performance photodetector has been developed. The Au nanostructure formation improves the light harvesting and enhances the device response. This economical method facilitates the fabrication of large-area detectors within a minute. The fabricated device operates in self-powered mode with high on/off ratio, fast response, high detectivity and is able to detect very low light intensities in the range of ~ pW in a broad spectral range. A protective coating provides excellent stability to the device under harsh conditions without compromising its performance. Image sensing capability was also accomplished by the pixelated fabrication. The demonstrated prototypes have revealed the potential of the detector for commercial applications.

VB.1 Introduction

In this era of new materials, an important property that is often explored and exploited is photoconductivity. A whole range of photodetectors using carbon nanotubes [1], semiconductor quantum dots [2], nanorods [3], nanowires [4], nanoribbons [5], spherical nanoshells [6], perovskites [7], and thin films [8] as active elements have been developed with commendable properties. Recently, 2D materials have shown potential as next-generation photoconductors. While graphene based detectors working at 40 GHz have exhibited responsivity in the range of a few mA/W [9–11], transition metal dichalcogenides show responsivity ranging from 10^{-5} to 10^{3} A/W but slow respond in few ms [12–14] Topological insulators such as Sb_2Te_3 show detectivity of 10^{11} Jones with even slower times, ~ few minutes [15]. However, due to their atomically thin dimension, inevitably there will be insufficient light absorption. Individually, all these materials own advantages and constraints. In the context of high performance concerning all figure of merits, the device interface plays a key role. A position-dependent photoresponse measurement demonstrated a relatively stronger photodetection at the metal-channel interface and a high responsivity at p-n junction interface [16–18]. A considerable success has been achieved in the case of hybrids of 2D materials [19–24]. Responsivity as high as 10^{9} A/W was shown in graphene-

---

*Paper based on this study: ACS Appl. Electron. Mater., **1**, 577 (2019).

MoS_2 hybrid [20]. Also, heterojunction architectures of semiconducting materials have demonstrated an enhanced performance relative to pristine systems [25-28]. However, improving all the figure of merits in a single device is still challenging.

With emphasis on interfaces, even the conventional semiconductor structures are being revisited. Si and its interfaces with new materials such as graphene [29,30], TMDs [31,32] and topological insulators [33] are shown to exhibit excellent properties. The plasmonic contribution from metal nanoparticles onto the interface properties has also been emphasized [34–38]. Enhanced responsivity is seen in Au nanoparticle decorated Si [36] and two-fold increased photocurrent in MoS_2-Au plasmonic photodetector [34] has been observed. Although these techniques lead to good performing detectors, they are highly process involved and limited to small areas.

VB.2 Scope of the present investigation

High-performing large-area photodetectors are essential for optoelectronic applications. However, the existing photodetectors are limited to small areas, and at larger areas, the response slows down because of increased device capacitance. Capturing photon flux over a large area is particularly important for low-light conditions. This aspect becomes crucial in security applications and motion detection, in general. Besides, the trade-off between device active area and response speed limits the detector size. In the earlier section (Chapter VA), evidence of photodetection was demonstrated in the Au-Si device. In this work, Au-Si interface was revisited while making use of the silicide interface. The Au-Si interface usually brought about by the galvanic deposition of the metal, is relatively well studied for SERS [39,40], patterned deposition [41], and surface enhanced infrared spectroelectrochemistry [42]. Although the process is commonly known, the photodiode action of the interface is not much exploited. Here, the fabrication of Au-Si photodetector using a simple electroless plating method is demonstrated. Being a solution-based technique, the method enabled large area fabrication without compromising the detector response. The metal nanostructures enhance the performance of the fabricated detector through trapping the incoming photon flux. This self-powered detector displays high figure of merits and long-term environmental stability. The utility of the detector is demonstrated in the form of a power cum lux meter and also in a model security application.

VB.3 Experimental details

Device Fabrication: Si (n type, (100), 3-9 Ω-cm) substrate was sonicated in acetone and IPA for 10 min, followed by RCA cleaning and dried under nitrogen. This substrate was immersed in a plating solution of 5 mM $HAuCl_4$ in HF for different durations. Once the plating was done the substrate was rinsed in DI water and dried under nitrogen. For electrical measurement, copper wire contacts were taken from the top and bottom sides using Ag paste.

Image sensor was fabricated using maskless lithography technique. A clean Si substrate was spin coated with AZ photoresist (1.4 μm thick) and patterned using IMP Xpress 100. Au electrodes were deposited using physical vapor deposition technique. The same patterning technique was repeated to create the photoresist window of 100 μm for electroless deposition. After Au nanostructure growth, the substrate was cleaned with acetone to remove the photoresist mask followed by DI water and dried under nitrogen.

VB.4 Results and discussion

The device fabrication process is discussed in the previous section (Chapter VA). In brief, a clean n-type Si substrate was immersed in a petri dish containing a stoichiometric ratio of

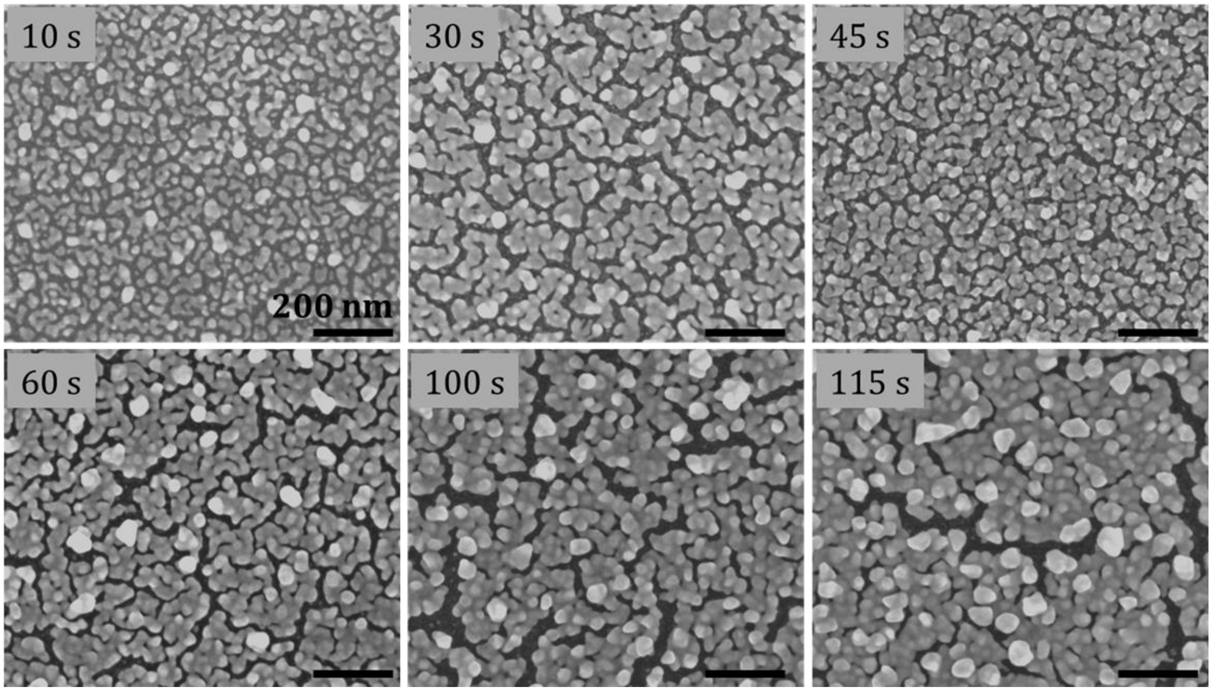

Figure VB.1: FESEM images of the grown Au film for different duration showing the granular connected film.

$HAuCl_4$ in HF for different durations. Thus, Au film got deposited on the Si surface by galvanic displacement. Figure VB.1 shows the SEM images of the film deposited for different durations. For a given concentration of the plating solution, the Au film thickness depends on the plating time (Figure VB.2a). The thickness is seen to increase linearly for the chosen concentration (5 mM) up to 80 s, beyond which it nearly saturates to ~ 73 nm. As the film is granular in nature, mean diameter of the granules and film fill factor were analyzed. The SEM images (Figure VB.1) were loaded to the ImageJ software with 8-bit filter. The analyzed mean diameter of the granules from SEM images is plotted against the thickness in Figure VB.2b, along with the fill factor (see Figure VB.2b). Both variations are linear. The slope of the diameter versus thickness curve (3.32) stands for the aspect ratio of the disk-like granules. At the same time, that associated with the fill factor variation (0.49), represents the sluggish nature of the film growth and limited connectivity among the granules. The latter plays an important role in device performance.

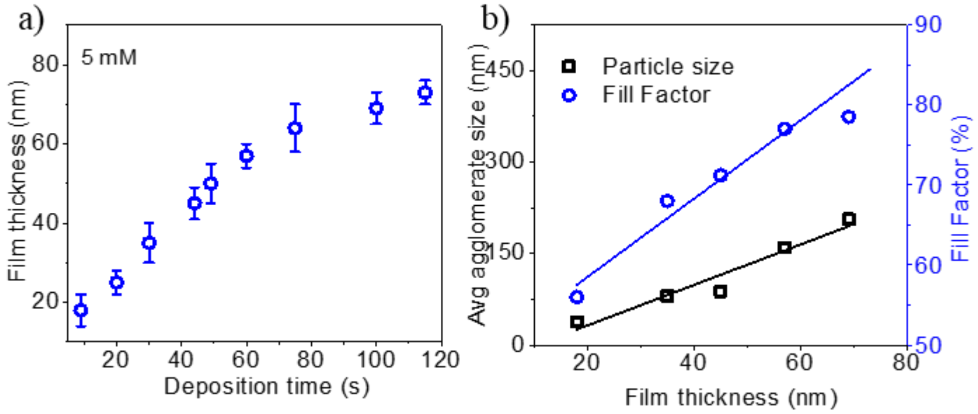

Figure VB.2: a) Variation of Au film thickness with plating time. b) Change in average agglomerate size and fill factor with film thickness.

The reflectance of Au/p-silicide/n-Si was examined over a wide wavelength range, 300-1500 nm (Figure VB.3a) with different thicknesses of the Au film. The control Si substrate, although less reflective (< 1%) in the visible region, reflects well beyond 1100 nm owing to its bandgap, which explains the limited spectral range accessible by the conventional Si detectors. At higher Au silicide thicknesses, the reflectance is dropped to less than 4% in IR region, which may be understood as due to enhanced internal scattering among the nanoparticle aggregates in the Au film. The observed drop in the reflectance at higher wavelengths is attributed to nanostructured surface. Agglomerates with the size range 100-

400 nm (approximately 8-12 nanoparticles) can red shift the absorption beyond 1100 nm via trapping and coupling the incident light into the underlying semiconducting layer. Also, the light harvesting beyond 1100 nm is influenced by the nanoparticle and underlying semiconductor interface [35–38,43–45]. These collective effects strongly reduce the reflectance of Si from 46% to less than 4% in IR region (Figure VB.3b), which is important in the present device.

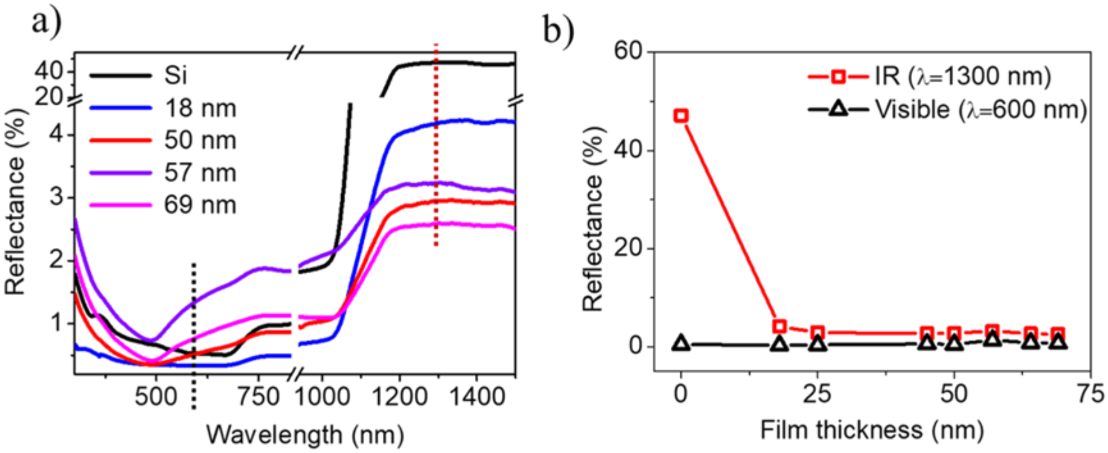

Figure VB.3: a) Reflectance spectra of the bare Si and Au of different thicknesses grown on Si. b) Comparison of reflectance in visible (600 nm) and IR (1300 nm) regions (read out at the vertical dotted lines in (a) for different film thicknesses. Less number of curves are shown in (a) to avoid crowding.

A device was fabricated by taking Ag paste contacts from the bottom n-Si and the top gold film. Figure VB.4a shows the I-V characteristics of the device in dark and illumination conditions. The device displayed a diode behavior with an ideality factor close to one (1.2). The dark current was under μA/cm^2 during the reverse bias. Under the illumination of 1 Sun, the reverse current increased by over three orders. It is noteworthy that the device can also operate at zero bias with a high on/off ratio of 4×10^4. These kind of self-powered devices are required for practical applications since they are energy efficient.

To understand the optimum film thickness for best performance, photoresponse at different film thicknesses was studied as depicted in Figure VB.4b for both dark and illuminated conditions. As seen, there was no observable change in the dark current with the film thickness, while the photocurrent was significantly enhanced. At lower film thicknesses (< 40 nm), although there existed a junction, the performance was low due to a lower fill factor

(Figure VB.2b) and the Au film coverage was not enough to conduct the generated photocurrent. For ~ 45-65 nm, the performance was maximum due to the optimum conducting network grown over the junction. This condition provides efficient light harvesting and charge conduction resulting in better device performance. Above ~ 65 nm, the fill factor was greater than 80% when the shadowing effect dominated, thus diminishing the light reaching the junction and hence the photocurrent. Thus, ~ 55 nm was considered optimal thickness of Au thin film, the same was adopted for further device fabrication.

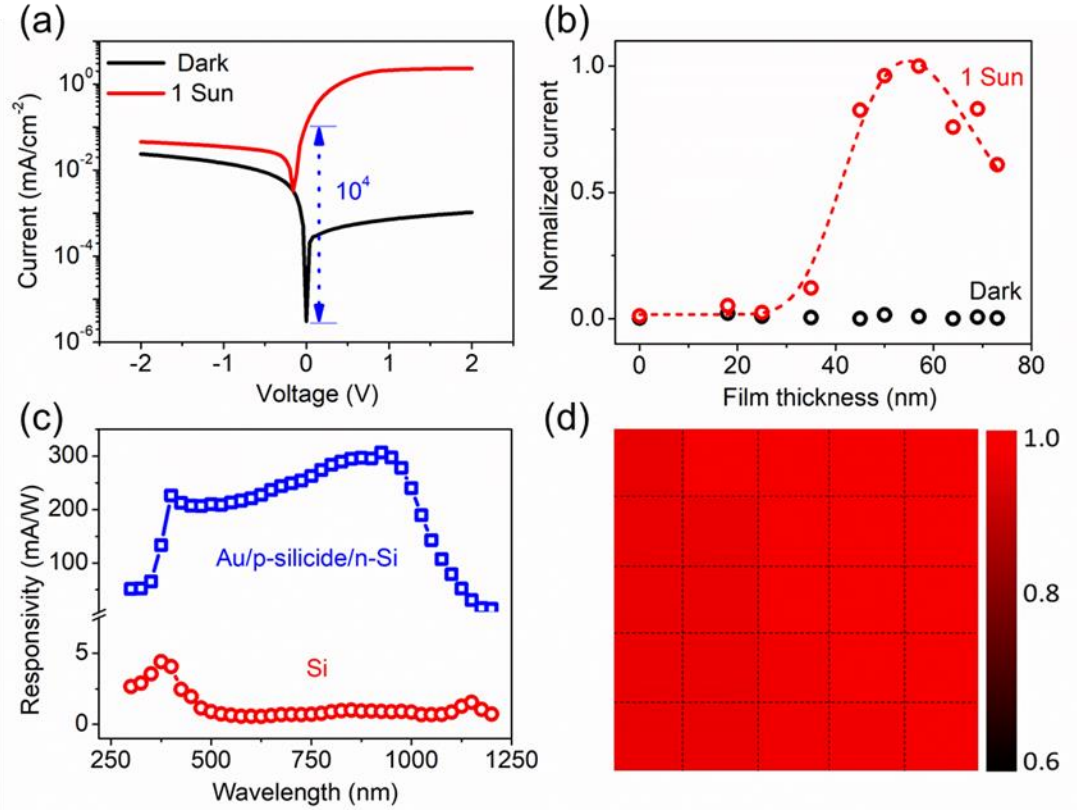

Figure VB.4: a) I-V characteristics of the device in dark and light conditions. b) Variation of the dark and photocurrent for different film thicknesses. c) Broad spectral response of the device compared with bare Si device. d) Uniform photovoltage response of the large area (500 mm^2) device for local illumination.

Figure VB.4c compares the spectral responses of the devices, one with ~ 55 nm Au film thickness and another, bare Si. A weak response of less than 5 mA/W was displayed by bare Si. Interestingly, the responsivity of Si was enhanced by plating the substrate. The device exhibits wide spectral sensitivity from 300-1200 nm and the peak responsivity, 310 mA/W, was observed at 920 nm. This wide spectral range from UV to NIR is highly important for broadband detection.

In addition, uniformity is another important factor deciding the performance of the device. Ideally, the response should be the same over the entire area of the device when illuminated locally. Figure VB.4d shows the photovoltage response of the device at different regions under local illumination. An optical microscope with a 100x objective was used to illuminate the device locally. Only minimal variation (< 5%) was seen over the entire area (500 mm^2) of the device, owing to the well–defined interface. Also, a 4" wafer photodetector was fabricated, amounting to an area of ~ 8000 mm^2 (excluding the edge isolation and contact area). The photoresponse along with the device photograph is shown in Figure VB.5.

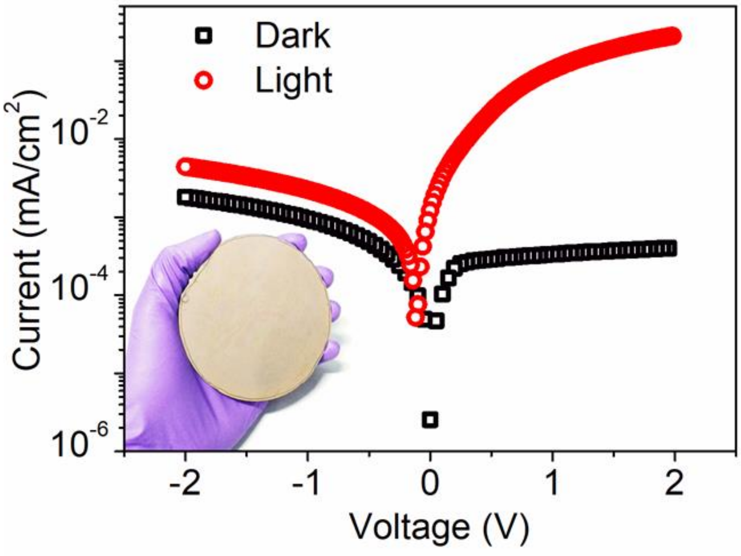

Figure VB.5: I-V behavior of the large area photodetector fabricated on a 4-inch wafer (inset: photograph of the fabricated 4-inch detector).

In order to study the response time of the detector, an optical chopper was used to generate light pulses (see inset, Figure VB.6c) and the photovoltage was monitored using an oscilloscope. The response was noted at zero bias voltage while varying the chopper frequency (Figure VB.6a). It is observed that the output was stable at different frequencies indicating the capability of the device for high frequency applications. Figure VB.6b shows that only 27% drop in the relative balance was observed (which corresponds to the 3dB cutoff value) at high frequency of 3000 Hz which is in agreement with the response of

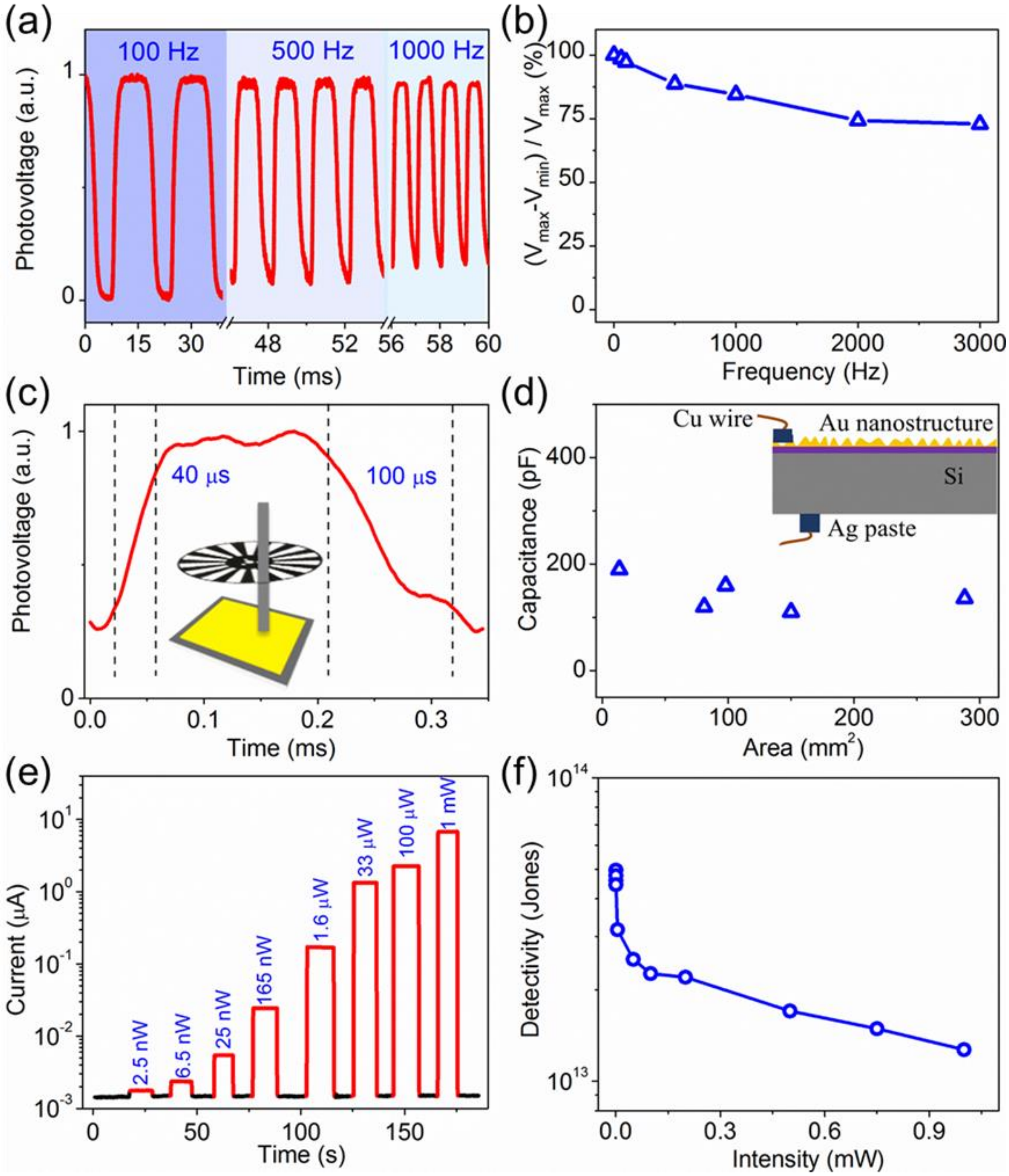

Figure VB.6: a) Response of the device for different chopping frequencies. b) Relative balance of the detector with chopping frequency. c) Rise/fall time of the detector (inset: chopper measurement). d) Capacitance variation with different device areas (inset: device architecture). e) Response of the device for different illumination intensities. f) Detectivity variation with the illumination intensity (red laser, 634 nm).

commercial detector measured under similar conditions (Figure VB.7). The response time is defined as the time taken to rise from 10% to 90% of the maximum value. Figure VB.6c shows

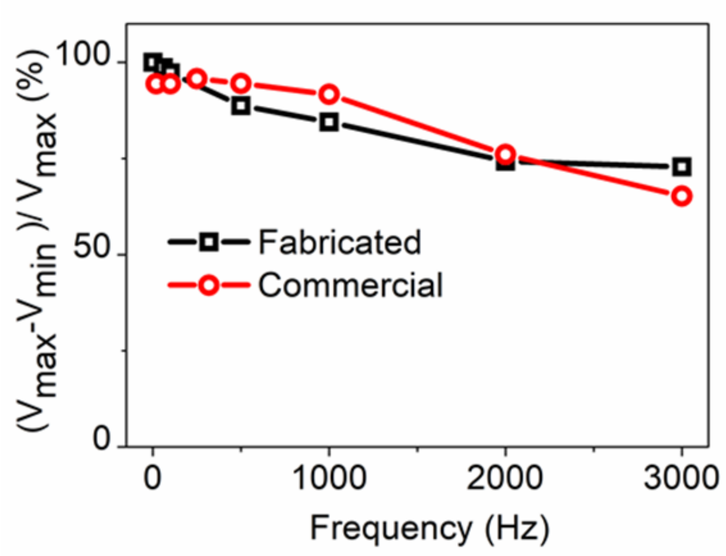

Figure VB.7: Relative balance of commercial and fabricated detectors with chopping frequency. Area of the detectors was to be 1 cm^2 and 1 mm^2 for fabricated and commercial respectively.

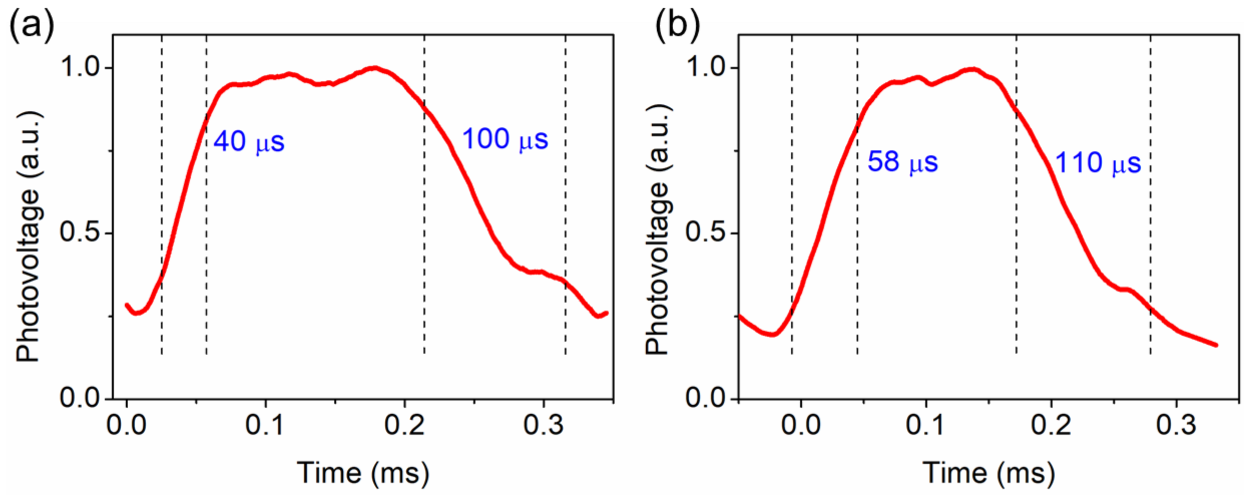

Figure VB.8: Response of the detector with an area a) 10 mm^2 b) 300 mm^2. Despite increasing the device area to a few hundred mm^2, the response degradation is minimal.

the magnified temporal response at 3000 Hz, from which the rise and fall times were measured to be 40 and 100 μs. This value is comparable with most two terminal Si based as well as other organic photodetectors reported in the literature (Table VB.1). Interestingly the response time remained almost similar with increasing device area (Figure VB.8). This is attributed to the device architecture considered in the measurement (inset, Figure VB.6d). The device consists of a sandwiched silicide layer between bottom n-Si (~ 20 kΩ) and top nanostructured gold film (~ 5 kΩ). Point contacts were taken from the top and bottom side using Ag paste where the strong field lines are confined to the local region and fades away from the contact. This results in an invariant capacitance value for different device areas keeping the speed to the μs range (Figure VB.8).

Fabrication of low light response photodetector has become a great challenge and is one of the most active research topics in optoelectronics field. For applications including security systems, night vision cameras, motion sensors etc., the detector should detect very low light intensity. Thus, detectivity is yet another important factor for a photodetector. It expresses how low light a device can detect. Here the device was illuminated with different intensities of light (red, 634 nm) and the response is plotted in Figure VB.6e. As seen, the device is able to respond in the nW range. The detectivity of the device is shown in Figure VB.6f and it is as high as 5 × 10^{13} Jones at 634 nm and expected to be higher at 920 nm due to peak responsivity, ~ 10^{15} Jones (see Figure VB.9). This indicates the potential use of the device in the aforementioned applications.

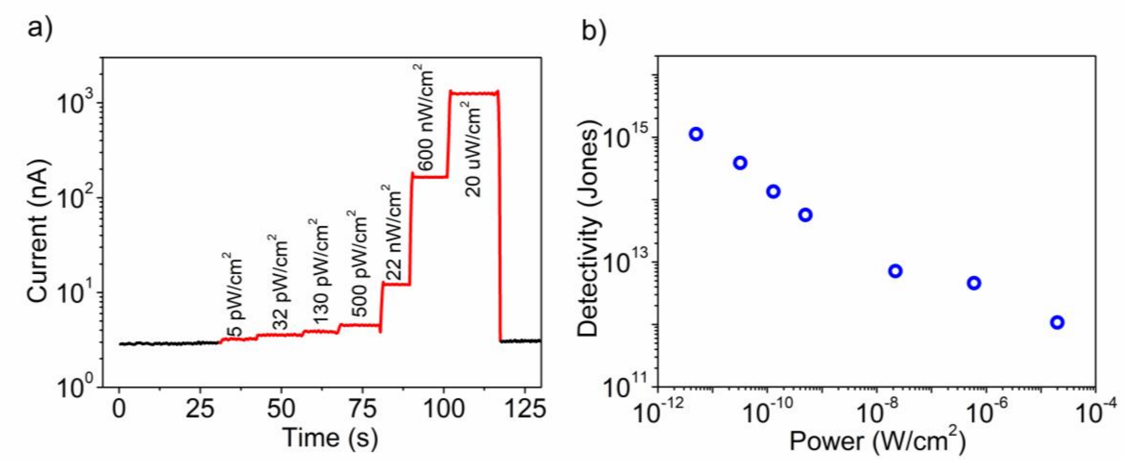

Figure VB.9: Detectivity measurement under red LED used to illuminate the entire active area of the device. a) Photocurrent response for different illumination intensity shows that fabricated detector is able to detect very low light intensities (pW/cm^2). b) Detectivity variation with illuminated intensity.

To exploit the image sensing capability of the device, a 25-pixel image sensor was fabricated using the conventional photolithography process (Figure VB.10a). Au electrodes were fabricated for each pixel followed by an open window using photoresist masking for electroless deposition. Figure VB.10a displays the image sensor array after electroless plating in the form of a 5 × 5 pixel array with a pixel dimension of 100 μm. To study each pixel, the light was illuminated locally to individual pixel and the corresponding

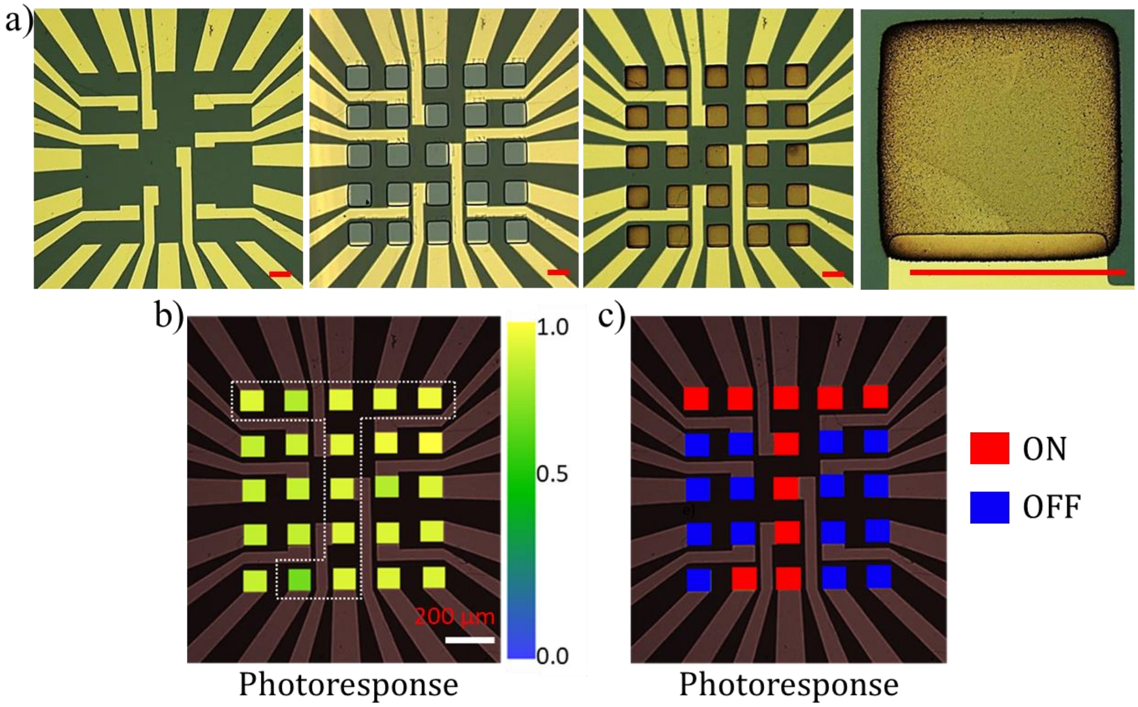

Figure VB.10: a) Optical microscope images of Au electrodes for each pixel, photoresist mask with open windows for pixel fabrication by electroless plating, Au nanostructures grown after electroless plating followed by removal of the photoresist, individual pixel showing active element and contact electrode (scale bar 100 µm). b) Normalized photovoltage response of the pixels when illuminated individually. Selected pixels were then exposed to light; the illuminated pixels are marked with dashed rectangles that form the letter 'J'. c) Response for alphabet 'J' illumination (response is normalized to ON (red) and OFF (blue).

photoresponse was illustrated into a mapping profile in Figure VB.10b. It is noteworthy that there is no dead pixel. All pixels were active and responded well when illuminated individually and the photoresponse has no cross-talk between the pixels. Later, using a maskless lithography system, the alphabet 'J' was illuminated on this image sensor and its response was noted. The highlighted pixels in Figure VB.10b were illuminated and the measured photovoltage response was normalized to ON (red) and OFF (blue) states. Figure VB.10c depicts the normalized photovoltage response of the pixels where 'J' is replicated.

Environmental stability is one of the major requirements in the photodetector technology for practical applications. Here a negative epoxy UV curable resin (SU8) was used as a protective coating for the device. This resin is a well-known transparent photoresist used in

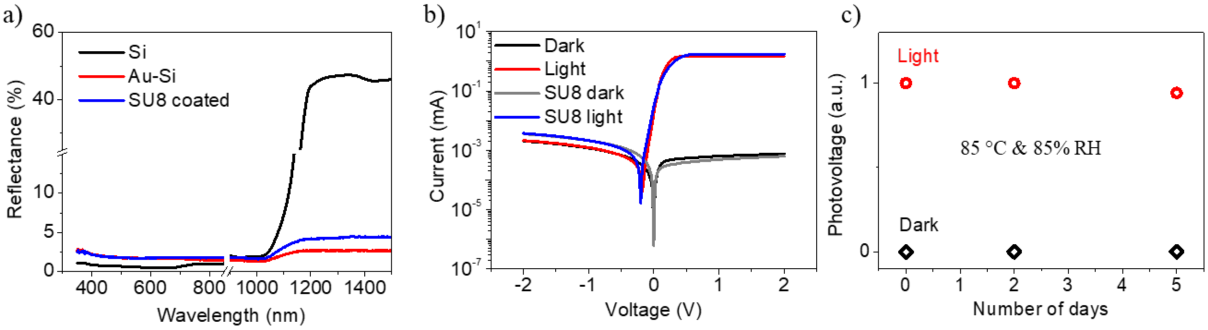

Figure VB.11: a) Comparison of reflectance before and after the SU8 protective coating. b) Response of the device with and without the SU8 protection coating. c) Stability of the device examined under 85% RH at 85 °C for five days.

photolithography, and once hard baked, it is highly stable in harsh conditions [46]. Standard coating process was adopted in this case and it was hard baked at 150 °C for 15 minutes. The reflectance study was carried out on SU8 coated Au/p-silicide/n-Si heterojunction, indicating only 2% rise in reflectance as shown in Figure VB.11a. Further, the I-V characterization (Figure VB.11b) in dark and light conditions before and after the protection coating reveals that there is no significant degradation in light sensitivity, suggesting that the detectivity is intact. In fact, the diode behavior improved with the coating due to lesser dark current and no ambient interaction. To understand the stability of the coating, the device was kept in the environmental test chamber for five days and the response was measured. Under this harsh condition of 85% RH at 85 °C, the device exhibited excellent stability (Figure VB.11c). Using this, a prototype security system, a USB compatible LUX meter and power meter were realized with the help of an Arduino board. In the security system prototype, the fabricated detector was mounted beside a commercial detector inside a toy house for comparison and connected to the same external circuit to trigger warning lights and security buzzer (Figure VB.12b). The door was opened to allow only weak scattered light as a sign of menacing activity. With such low level of lighting the fabricated detector could be activated turning on the buzzer and the warning lights while the commercial detector required intense light to get activated. In addition, prototype LUX and power meters were fabricated by mounting the device inside a 3D printed box along with the Arduino chip. With proper calibration, the devices could display the readings on a connected mobile phone as shown in Figure VB.12a. The range of measurement varies from 0-200000 for LUX meter and 0.5-30 mW/cm^2 for the power meter. The range and resolutions are limited by the reading capacity of the Arduino chip.

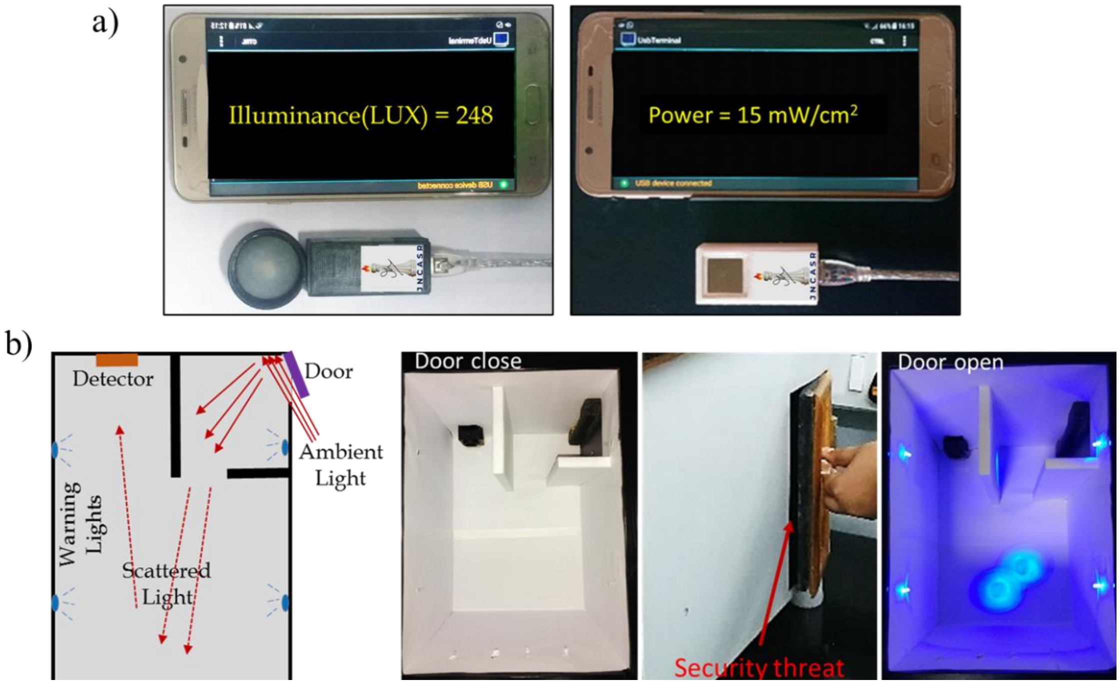

Figure VB.12: a) Prototype LUX and power meter (active area = 14 × 14 mm^2) with values displayed using a mobile phone. b) Detector mounted in a toy house for undesired motion detection. Schematic is on the left. 'Door close' photograph is taken with the 'roof' removed.

VB.5 Conclusions

Here a simple solution method for fabricating a low-cost, large-area photodetector based on light harvesting Au nanostructures grown on a Si substrate leading to a Au silicide (p)−(n) Si active interface is reported. The process is quick, taking only minutes to fabricate a detector of any arbitrary area. This detector exhibits a fast response (∼40 μs) and can detect low light intensities (few pW) with high detectivity (∼10^{15} Jones). The device covers a broad spectral range from 300 to 1200 nm. In addition, it shows excellent uniformity throughout the entire 500 mm^2 area with <5% variation in response. Notably, the detector operates in self-powered mode with a high on/off ratio (10^4), thus making it energy efficient. With a commonly available protective coating, excellent environmental stability is shown for the device under harsh conditions for several days. The photodetector utility is demonstrated as a prototype imaging system, lux and power meter, and also as a tool for security applications.

Table 1. Comparison of the device performance with some of the large area detectors from literature.

Material	Area (mm^2)	Responsivity (A/W)	Detectivity (Jones)	Response time (µs)	Spectral range (nm)	Reference
Au/p-silicide/n-Si	**500**	**0.31**	**5×10^{13}**	**40/100**	**300-1200**	**This work**
Integrated ZnO NWs	260	$\sim 1^{a)}$	-	$\sim 15 \times 10^{6}$	UV	47
ZnO/Au mesh	100	10^{-2}	10^{10}	$3.3 \times 10^{6}/20 \times 10^{6}$	UV	48
ZnO/rGO	50	0.0013	-	6×10^{6}	365	49
Si:GaN/ZnO	50	0.96	4.87×10^{9}	$29 \times 10^{6}/141 \times 10^{6}$	UV	50
Si/Cs-FAPbI$_3$	25	0.844	3.2×10^{11}	4/8	300-1200	51
rGO/GaN	21	$9 \text{ x } 10^{-3}$	8×10^{10}	$60 \times 10^{3}/267 \times 10^{3}$	280-360	52
PCDTBT:PC70BM	20	$\sim 10^{-1\ a)}$	$\sim 10^{13}$	-	300-800	53
MAPbI$_3$	10.32	620	-	100×10^{3}	400-800	54
SWCNTs/MAPbI$_{3-x}$Cl$_x$	10	13.8	-	10×10^{3}	300-800	55
InP p-i-n detector	9	0.12	-	-	533	56
MoS$_2$/Si	9	0.3	$\sim 10^{13}$	3/40	450-1050	31
SnTe/Si	9	2.36	1.54×10^{14}	2.2/3.8	1064	33
α-CsPbI$_3$	9	0.035	1.8×10^{12}	-	400-700	57
MAPbI$_3$	7	0.395	10^{12}	1.2/3.2	400-780	58
MoSe$_2$/Si	7	0.27	7.13×10^{10}	0.27/0.35	365-1310	32
AuNPs@graphene/CH$_3$-SiNWs	5	1.5	2.54×10^{14}	73/96	350-1100	45
AuNPs/SiNM Schottky	$2.25^{a)}$	0.21	-	25×10^{4}	-	36
Graphene/Si	0.25	0.2	6.1×10^{12}	0.004/0.012	200-1100	29

$^{a)}$Calculated

References

[1] M. Freitag, Y. Martin, J. A. Misewich, R. Martel, and P. Avouris, *Photoconductivity of Single Carbon Nanotubes*, Nano Lett. **3**, 1067 (2003).

[2] G. Konstantatos, I. Howard, A. Fischer, S. Hoogland, J. Clifford, E. Klem, L. Levina, and E. H. Sargent, *Ultrasensitive Solution-Cast Quantum Dot Photodetectors*, Nature **442**, 180 (2006).

[3] S. Sarkar and D. Basak, *Self Powered Highly Enhanced Dual Wavelength ZnO@CdS Core–Shell Nanorod Arrays Photodetector: An Intelligent Pair*, ACS Appl. Mater. Interfaces **7**,

16322 (2015).

[4] S.-B. Chen, Y.-C. Chi, Y.-C. Liao, H.-P. Wang, G.-R. Lin, D.-H. Lien, C.-L. Wu, and J.-H. He, *360° Omnidirectional, Printable and Transparent Photodetectors for Flexible Optoelectronics*, Npj Flex. Electron. **2**, (2018).

[5] B. Chitara, L. S. Panchakarla, S. B. Krupanidhi, and C. N. R. Rao, *Infrared Photodetectors Based on Reduced Graphene Oxide and Graphene Nanoribbons*, Adv. Mater. **23**, 5419 (2011).

[6] D. H. Lien, Z. Dong, J. R. D. Retamal, H. P. Wang, T. C. Wei, D. Wang, J. H. He, and Y. Cui, *Resonance-Enhanced Absorption in Hollow Nanoshell Spheres with Omnidirectional Detection and High Responsivity and Speed*, Adv. Mater. (2018).

[7] R. Dong, C. Lan, X. Xu, X. Liang, X. Hu, D. Li, Z. Zhou, L. Shu, S. Yip, C. Li, S. W. Tsang, and J. C. Ho, *Novel Series of Quasi-2D Ruddlesden-Popper Perovskites Based on Short-Chained Spacer Cation for Enhanced Photodetection*, ACS Appl. Mater. Interfaces (2018).

[8] L. Dou, Y. M. Yang, J. You, Z. Hong, W. H. Chang, G. Li, and Y. Yang, *Solution-Processed Hybrid Perovskite Photodetectors with High Detectivity*, Nat. Commun. **5**, 1 (2014).

[9] F. Xia, T. Mueller, Y. M. Lin, A. Valdes-Garcia, and P. Avouris, *Ultrafast Graphene Photodetector*, Nat. Nanotechnol. **4**, 839 (2009).

[10] T. Mueller, F. Xia, and P. Avouris, *Graphene Photodetectors for High-Speed Optical Communications*, Nat. Photonics (2010).

[11] F. Xia, T. Mueller, R. Golizadeh-Mojarad, M. Freitage, Y. M. Lin, J. Tsang, V. Perebeinos, and P. Avouris, *Photocurrent Imaging and Efficient Photon Detection in a Graphene Transistor*, Nano Lett. (2009).

[12] O. Lopez-Sanchez, D. Lembke, M. Kayci, A. Radenovic, and A. Kis, *Ultrasensitive Photodetectors Based on Monolayer MoS 2*, Nat. Nanotechnol. **8**, 497 (2013).

[13] F. Liu, H. Shimotani, H. Shang, T. Kanagasekaran, V. Zólyomi, N. Drummond, V. I. Fal'Ko, and K. Tanigaki, *High-Sensitivity Photodetectors Based on Multilayer GaTe Flakes*, ACS Nano **8**, 752 (2014).

[14] N. Perea-Lõpez, A. L. Elías, A. Berkdemir, A. Castro-Beltran, H. R. Gutiérrez, S. Feng, R. Lv, T. Hayashi, F. Lõpez-Urías, S. Ghosh, B. Muchharla, S. Talapatra, H. Terrones, and M. Terrones, *Photosensor Device Based on Few-Layered WS2films*, Adv. Funct. Mater. **23**, 5511 (2013).

[15] K. Zheng, L.-B. Luo, T.-F. Zhang, Y.-H. Liu, Y.-Q. Yu, R. Lu, H.-L. Qiu, Z.-J. Li, and J. C. Andrew Huang, *Optoelectronic Characteristics of a near Infrared Light Photodetector Based on a Topological Insulator Sb $_2$ Te $_3$ Film*, J. Mater. Chem. C **3**, 9154 (2015).

[16] E. J. H. Lee, K. Balasubramanian, R. T. Weitz, M. Burghard, and K. Kern, *Contact and Edge Effects in Graphene Devices*, Nat. Nanotechnol. **3**, 486 (2008).

[17] J. Park and C. Ruiz-vargas, *Imaging of Photocurrent Generation and Collection in Single-Layer Graphene 2009*, 16 (2009).

[18] M. C. Lemme, F. H. L. Koppens, A. L. Falk, M. S. Rudner, H. Park, L. S. Levitov, and C. M. Marcus, *Gate-Activated Photoresponse in a Graphene p-n Junction*, Nano Lett. **11**, 4134 (2011).

[19] C. H. Liu, Y. C. Chang, T. B. Norris, and Z. Zhong, *Graphene Photodetectors with Ultra-Broadband and High Responsivity at Room Temperature*, Nat. Nanotechnol. **9**, 273 (2014).

[20] K. Roy, T. Ahmed, H. Dubey, T. P. Sai, R. Kashid, S. Maliakal, K. Hsieh, S. Shamim, and A. Ghosh, *Number-Resolved Single-Photon Detection with Ultralow Noise van Der Waals Hybrid*, Adv. Mater. **30**, 1 (2018).

[21] H. Tan, W. Xu, Y. Sheng, C. S. Lau, Y. Fan, Q. Chen, M. Tweedie, X. Wang, Y. Zhou, and J. H. Warner, *Lateral Graphene-Contacted Vertically Stacked WS2/MoS2 Hybrid Photodetectors with Large Gain*, Adv. Mater. **29**, 1 (2017).

[22] J. Yao, Z. Zheng, and G. Yang, *Layered-Material WS_2/Topological Insulator Bi_2Te_3 Heterostructure Photodetector with Ultrahigh Responsivity in the Range from 370 to 1550 nm*, J. Mater. Chem. C **4**, 7831 (2016).

[23] G. Konstantatos, M. Badioli, L. Gaudreau, J. Osmond, M. Bernechea, F. P. G. De Arquer, F. Gatti, and F. H. L. Koppens, *Hybrid Grapheneĝquantum Dot Phototransistors with Ultrahigh Gain*, Nat. Nanotechnol. (2012).

[24] J. Bullock, M. Amani, J. Cho, Y. Z. Chen, G. H. Ahn, V. Adinolfi, V. R. Shrestha, Y. Gao, K. B. Crozier, Y. L. Chueh, and A. Javey, *Polarization-Resolved Black Phosphorus/Molybdenum Disulfide Mid-Wave Infrared Photodiodes with High Detectivity at Room Temperature*, Nat. Photonics (2018).

[25] C. H. Lin, H. C. Fu, D. H. Lien, C. Y. Hsu, and J. H. He, *Self-Powered Nanodevices for Fast UV Detection and Energy Harvesting Using Core-Shell Nanowire Geometry*, Nano Energy

(2018).

[26] M. Sun, Q. Fang, Z. Zhang, D. Xie, Y. Sun, J. Xu, W. Li, T. Ren, and Y. Zhang, *All-Inorganic Perovskite Nanowires-InGaZnO Heterojunction for High-Performance Ultraviolet-Visible Photodetectors*, ACS Appl. Mater. Interfaces (2018).

[27] L. Hu, J. Yan, M. Liao, H. Xiang, X. Gong, L. Zhang, and X. Fang, *An Optimized Ultraviolet-a Light Photodetector with Wide-Range Photoresponse Based on Zns/Zno Biaxial Nanobelt*, Adv. Mater. **24**, 2305 (2012).

[28] W. Yang, Y. Zhang, J. Cai, X. Xu, W. Xu, and X. Fang, *Self-Powered Dual-Color UV-Green Photodetectors Based on SnO_2 Millimeter Wire and Microwires/$CsPbBr_3$ Particles Heterojunctions* , J. Phys. Chem. Lett. (2019).

[29] X. Wan, Y. Xu, H. Guo, K. Shehzad, A. Ali, Y. Liu, J. Yang, D. Dai, C.-T. Lin, L. Liu, H.-C. Cheng, F. Wang, X. Wang, H. Lu, W. Hu, X. Pi, Y. Dan, J. Luo, T. Hasan, X. Duan, X. Li, J. Xu, D. Yang, T. Ren, and B. Yu, *A Self-Powered High-Performance Graphene/Silicon Ultraviolet Photodetector with Ultra-Shallow Junction: Breaking the Limit of Silicon?*, Npj 2D Mater. Appl. **1**, 4 (2017).

[30] J. Shen, X. Liu, X. Song, X. Li, J. Wang, Q. Zhou, S. Luo, W. Feng, X. Wei, S. Lu, S. Feng, C. Du, Y. Wang, H. Shi, and D. Wei, *High-Performance Schottky Heterojunction Photodetector with Directly Grown Graphene Nanowalls as Electrodes*, Nanoscale **9**, 6020 (2017).

[31] L. Wang, J. Jie, Z. Shao, Q. Zhang, X. Zhang, Y. Wang, Z. Sun, and S. T. Lee, *MoS_2/Si Heterojunction with Vertically Standing Layered Structure for Ultrafast, High-Detectivity, Self-Driven Visible-near Infrared Photodetectors*, Adv. Funct. Mater. **25**, 2910 (2015).

[32] J. Mao, Y. Yu, L. Wang, X. Zhang, Y. Wang, Z. Shao, and J. Jie, *Ultrafast, Broadband Photodetector Based on $MoSe_2$/Silicon Heterojunction with Vertically Standing Layered Structure Using Graphene as Transparent Electrode*, Adv. Sci. **3**, 1 (2016).

[33] H. Zhang, B. Man, and Q. Zhang, *Topological Crystalline Insulator SnTe/Si Vertical Heterostructure Photodetectors for High-Performance Near-Infrared Detection*, ACS Appl. Mater. Interfaces **9**, 14067 (2017).

[34] J. Miao, W. Hu, Y. Jing, W. Luo, L. Liao, A. Pan, S. Wu, J. Cheng, X. Chen, and W. Lu, *Surface Plasmon-Enhanced Photodetection in Few Layer MoS_2 Phototransistors with Au*

Nanostructure Arrays, Small **11**, 2392 (2015).

[35] C. F. Guo, T. Sun, F. Cao, Q. Liu, and Z. Ren, *Metallic Nanostructures for Light Trapping in Energy-Harvesting Devices*, Light Sci. Appl. **3**, 1 (2014).

[36] H. J. Ha, B. H. Kang, S. W. Yeom, J. Park, Y. H. Lee, and B. K. Ju, *Localized-Surface-Plasmon-Enhanced Multifunction Silicon Nanomembrane Schottky Diodes Based on Au Nanoparticles*, Nanotechnology **26**, (2015).

[37] H. Tan, R. Santbergen, A. H. M. Smets, and M. Zeman, *Plasmonic Light Trapping in Thin-Film Silicon Solar Cells with Improved Self-Assembled Silver Nanoparticles*, Nano Lett. **12**, 4070 (2012).

[38] F. J. Beck, S. Mokkapati, and K. R. Catchpole, *Plasmonic Light-Trapping for Si Solar Cells Using Self-Assembled, Ag Nanoparticles*, Prog. Photovoltaics Res. Appl. **18**, 500 (2010).

[39] T. Bhuvana, G. V. P. Kumar, G. U. Kulkarni, and C. Narayana, *Carbon Assisted Electroless Gold for Surface Enhanced Raman Scattering Studies*, J. Phys. Chem. C **111**, 6700 (2007).

[40] T. Bhuvana, G. V. Pavan Kumar, C. Narayana, and G. U. Kulkarni, *Nanogranular Au Films Deposited on Carbon Covered Si Substrates for Enhanced Optical Reflectivity and Raman Scattering*, Nanotechnology **18**, 0 (2007).

[41] T. Bhuvana and G. U. Kulkarni, *Polystyrene as a Zwitter Resist in Electron Beam Lithography Based Electroless Patterning of Gold*, Bull. Mater. Sci. **31**, 201 (2008).

[42] H. Miyake, S. Ye, and M. Osawa, *Electroless Deposition of Gold Thin Films on Silicon for Surface-Enhanced Infrared Spectroelectrochemistry*, Electrochem. Commun. **4**, 973 (2002).

[43] K. S. Lee and M. A. El-Sayed, *Gold and Silver Nanoparticles in Sensing and Imaging: Sensitivity of Plasmon Response to Size, Shape, and Metal Composition*, J. Phys. Chem. B **110**, 19220 (2006).

[44] D. M. Schaadt, B. Feng, and E. T. Yu, *Enhanced Semiconductor Optical Absorption via Surface Plasmon Excitation in Metal Nanoparticles*, Appl. Phys. Lett. **86**, 1 (2005).

[45] L. B. Luo, L. H. Zeng, C. Xie, Y. Q. Yu, F. X. Liang, C. Y. Wu, L. Wang, and J. G. Hu, *Light Trapping and Surface Plasmon Enhanced High-Performance NIR Photodetector*, Sci. Rep. **4**, (2014).

[46] C. Zeng, H. Wang, H. Zhou, and T. Lin, *Self-Cleaning, Superhydrophobic Cotton Fabrics with Excellent Washing Durability, Solvent Resistance and Chemical Stability Prepared*

from an SU-8 Derived Surface Coating, RSC Adv. **5**, 61044 (2015).

[47] S. Bai, W. Wu, Y. Qin, N. Cui, D. J. Bayerl, and X. Wang, *High-Performance Integrated ZnO Nanowire UV Sensors on Rigid and Flexible Substrates*, Adv. Funct. Mater. **21**, 4464 (2011).

[48] S. Kiruthika, S. Singh, and G. U. Kulkarni, *Large Area Transparent ZnO Photodetectors with Au Wire Network Electrodes*, RSC Adv. **6**, 44668 (2016).

[49] Z. Wang, X. Zhan, Y. Wang, S. Muhammad, Y. Huang, and J. He, *A Flexible UV Nanosensor Based on Reduced Graphene Oxide Decorated ZnO Nanostructures*, Nanoscale **4**, 2678 (2012).

[50] R. Anitha, R. Ramesh, R. Loganathan, D. S. Vavilapalli, K. Baskar, and S. Singh, *Large Area Ultraviolet Photodetector on Surface Modified Si:GaN Layers*, Appl. Surf. Sci. **435**, 1057 (2018).

[51] J.-Q. Liu, Y. Gao, G.-A. Wu, X.-W. Tong, C. Xie, L.-B. Luo, L. Liang, and Y.-C. Wu, *Silicon/Perovskite Core–Shell Heterojunctions with Light-Trapping Effect for Sensitive Self-Driven Near-Infrared Photodetectors*, ACS Appl. Mater. Interfaces **10**, 27850 (2018).

[52] N. Prakash, M. Singh, G. Kumar, A. Barvat, K. Anand, P. Pal, S. P. Singh, and S. P. Khanna, *Ultrasensitive Self-Powered Large Area Planar GaN UV-Photodetector Using Reduced Graphene Oxide Electrodes*, Appl. Phys. Lett. **109**, (2016).

[53] A. Armin, M. Hambsch, I. K. Kim, P. L. Burn, P. Meredith, and E. B. Namdas, *Thick Junction Broadband Organic Photodiodes*, Laser Photonics Rev. **8**, 924 (2014).

[54] H. W. Chen, N. Sakai, A. K. Jena, Y. Sanehira, M. Ikegami, K. C. Ho, and T. Miyasaka, *A Switchable High-Sensitivity Photodetecting and Photovoltaic Device with Perovskite Absorber*, J. Phys. Chem. Lett. **6**, 1773 (2015).

[55] I. Ka, L. F. Gerlein, R. Nechache, and S. G. Cloutier, *High-Performance Nanotube-Enhanced Perovskite Photodetectors*, Sci. Rep. **7**, 1 (2017).

[56] W. Yang, H. Yang, G. Qin, Z. Ma, J. Berggren, M. Hammar, R. Soref, and W. Zhou, *Large-Area InP-Based Crystalline Nanomembrane Flexible Photodetectors*, Appl. Phys. Lett. **96**, 2008 (2010).

[57] K. M. Sim, A. Swarnkar, A. Nag, and D. S. Chung, *Phase Stabilized α-CsPbI3Perovskite Nanocrystals for Photodiode Applications*, Laser Photonics Rev. **12**, 1 (2018).

[58] B. R. Sutherland, A. K. Johnston, A. H. Ip, J. Xu, V. Adinolfi, P. Kanjanaboos, and E. H. Sargent, *Sensitive, Fast, and Stable Perovskite Photodetectors Exploiting Interface Engineering*, ACS Photonics **2**, 1117 (2015).

Chapter VC

A Primitive Artificial Visual System

Summary

A primitive artificial visual system has been demonstrated using an Au-Si photodetector and an Ag-ASN neuromorphic device. The photodetector reported in Chapter VB was used for converting optical signals into electrical stimuli and is then processed by the neuromorphic device. Essential synaptic activities, such as STP and LTP were emulated. More interestingly, a primitive visual perception concept was also demonstrated in the system. Excitingly, the synaptic functions were emulated with no external bias voltage.

VC.1 Introduction

In the human brain, about 80% of the information is received through vision, and half of the cerebral cortex is involved in processing that information [1,2]. Thus, an artificial visual system plays a crucial role in next-generation hardware-based artificial intelligence. Several optoelectronic neuromorphic devices have been explored in the literature towards fabricating devices responding to optical signal and emulating synaptic plasticity [3–10]. Li et al., proposed an ITO/Nb:$SrTiO_3$ based optoelectronic device for mimicking interest-modulated human visual memories [11]. Yang et al., reported an optoelectronic synaptic device based on the hybrid structure of silicon nanomembrane and perovskite for LTM-based mimicking of visual learning and memory processes under different mood states [12].

VC.2 Scope of the present investigation

In the human visual system, information is perceived by the eye and converted to an electrical signal. This information is then processed by the brain, thus creating different types of memory. Existing literature is mostly focused on fabricating optoelectronic neuromorphic devices where optical signals are used as input stimuli to form the memory in the device itself. However with this arrangement, the photodetection ability of the device may be hindered due to a change in its conducting state during memory formation. Shen et al., combined In_2O_3 UV detector and Ni/Al_2O_3 memory device for mimicking the human visual system architecture [13]. However, the utilization of a non-volatile memory device lacks the processing ability seen in the human brain. These issues are addressed in the present investigation by mimicking the human visual system, utilizing the Au-Si photodetector discussed in Chapter VB, and Ag-ASN neuromorphic device discussed in Chapter III.

VC.3 Experimental details

The photodetector array was fabricated by connecting nine individual detectors (1x1 cm) in series to produce the required photovoltage. The output of the array was fed to the Ag-ASN device via copper wire contacts. Electrical current measurement was performed using Keithley 2450.

VC.4 Results and discussion

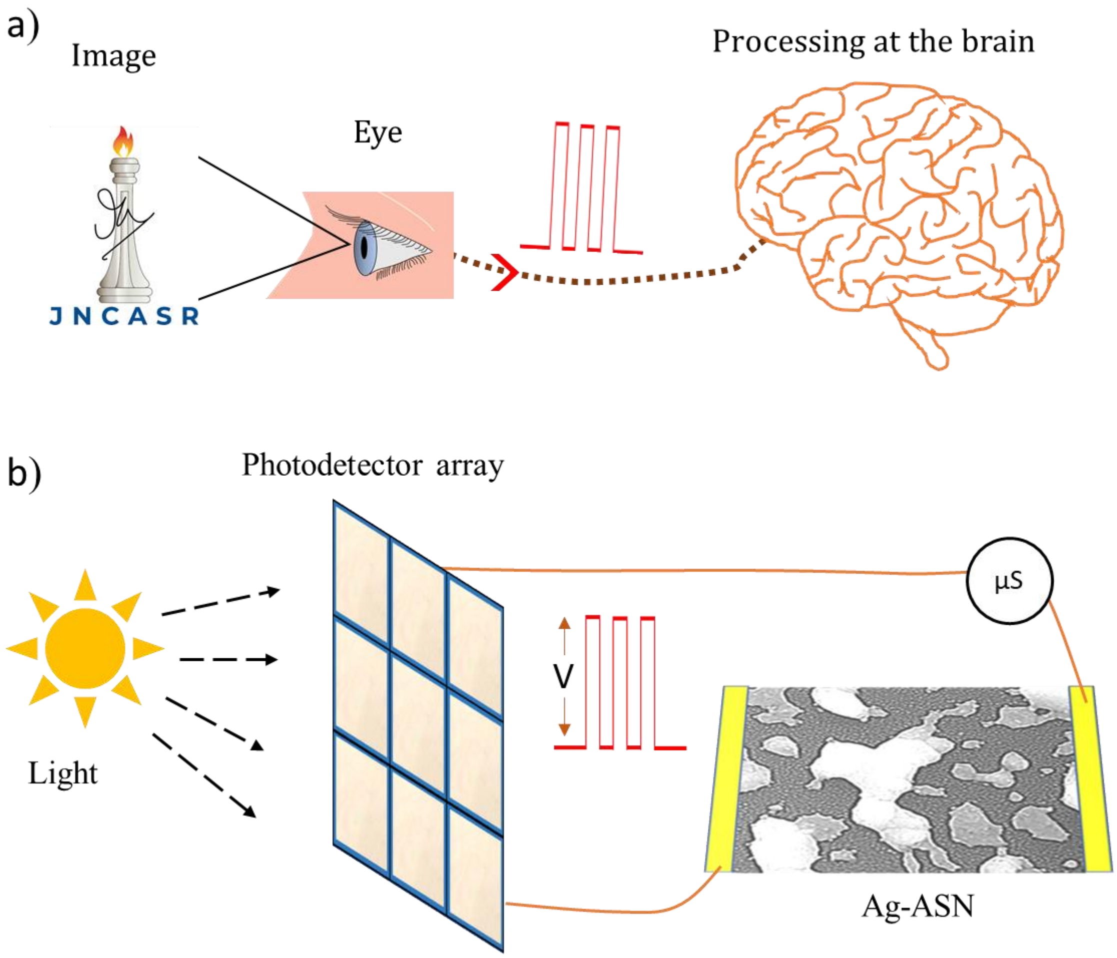

Figure VC.1: a) Schematic illustration of the human visual system. b) Mimicking the visual system architecture using the photodetector array and Ag-ASN neuromorphic device.

The schematic of the human visual system architecture is shown in Figure VC.1a. Information in the form of an optical signal is received by the eye, which converts them into an electrical signal and then processed by the brain for further cognition or storage. This architecture is mimicked using Au-Si photodetector and Ag-ASN neuromorphic device, as shown in the schematic Figure VC.1b. Optical pulse signals were illuminated on to the photodetector gets converted into pulsed electrical signals. A mild illumination was also provided to the photodetector array for generating a constant photovoltage of ~ 100 mV as a background reading voltage. These signals were then received by the Ag-ASN device. Depending on the signal parameters, different visual synaptic plasticities was emulated. To emulate the visual short- and long-term memory, optical signals of 5 and 15 pulses were applied as shown in Figure VC.2. During the application of the 5 optical signals, the photovoltage (~0.92 V) generated from the photodetector is shown in Figure VC.2a. This pulsed stimulus switches the Ag-ASN device to a high conductance state. The conductance retention was found to be around 60 s before dropping to its initial value, thus emulating visual short-term plasticity. While applying 15 pulses, the conductance retention was more than 350 s, thus emulating LTP as shown in Figure VC.2b. Excitingly, no external bias voltage was applied to mimic these features.

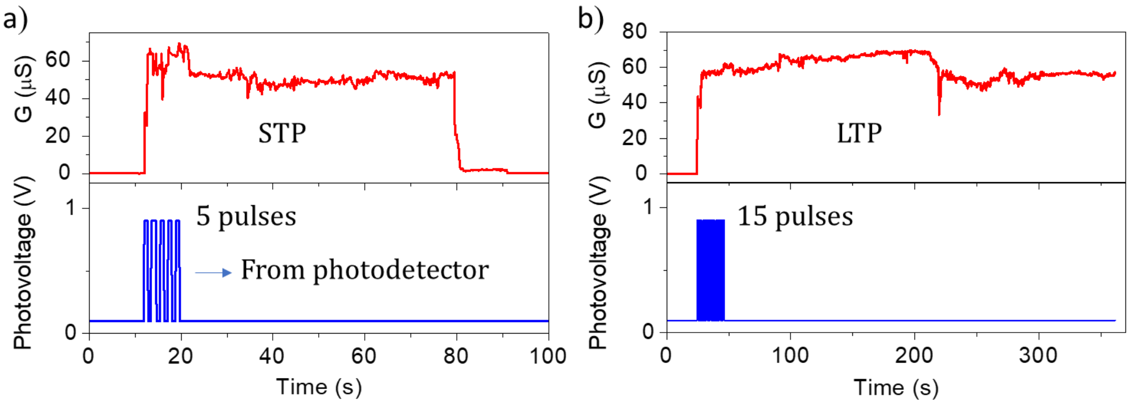

Figure VC.2: Emulating STP with 5 pulses a) and LTP with 15 pulses b). Pulse width and the interval was ~ 700 ms.

Persistence of vision is a phenomenon where an object perceived by the eye does not cease for some time even after the optical signal from the object has stopped [14–16]. This is the reason for experiencing the visual perception of motion [17]. To emulate this, 5 optical pulse signals of 250 ms width were applied to the photodetector with two different pulse intervals as shown in Figure VC.3. In the case of a shorter pulse interval (0.25 s), a continuous conductance state was archived in the Ag-ASN device, thus mimicking the visual perception (Figure VC.3a). For longer pulse interval (10 s), the switched conductance state dropped to its initial value after each pulse as shown in Figure VC.3b, thus mimicking the flickering visual perception.

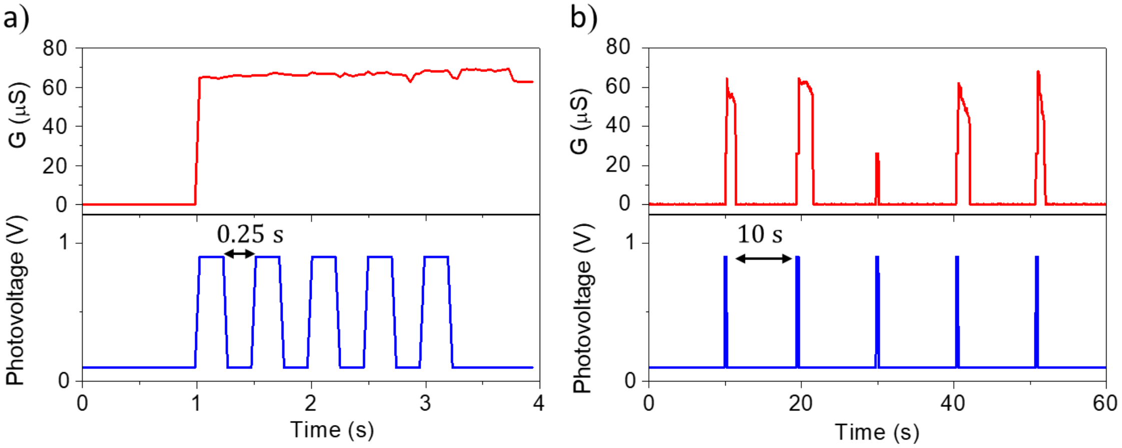

Figure VC.3: Emulating visual perception. a) smaller pulse interval resulted in continuous conductance state while, b) larger pulse interval showed flickering conductance, thus mimicking flickering visual perception. Pulse width was ~250 ms.

VC.5 Conclusions

The human visual system was mimicked using a photodetector array and neuromorphic device. An optical stimulus was converted to an electrical signal by the photodetector and then processed by the Ag-ASN device to emulate different visual memories such as STP and LTP. More interestingly, a primitive visual perception of motion, was also demonstrated. Excitingly, the synaptic functions were emulated with no external bias voltage.

References

[1] *A Vision of the Brain*, Neurology **45**, 206 (1995).

[2] D. Milner and M. Goodale, *The Visual Brain in Action* (Oxford University Press, 2006).

[3] C. Wan, P. Cai, M. Wang, Y. Qian, W. Huang, and X. Chen, *Artificial Sensory Memory*, Adv. Mater. **32**, 1902434 (2020).

[4] D. Li, C. Li, N. Ilyas, X. Jiang, F. Liu, D. Gu, M. Xu, Y. Jiang, and W. Li, *Color-Recognizing Si-Based Photonic Synapse for Artificial Visual System*, Adv. Intell. Syst. **2**, 2000107 (2020).

[5] L. Zhao, Z. Fan, S. Cheng, L. Hong, Y. Li, G. Tian, D. Chen, Z. Hou, M. Qin, M. Zeng, X. Lu, G. Zhou, X. Gao, and J. M. Liu, *An Artificial Optoelectronic Synapse Based on a*

Photoelectric Memcapacitor, Adv. Electron. Mater. **6**, 1900858 (2020).

[6] W. Huang, P. Hang, Y. Wang, K. Wang, S. Han, Z. Chen, W. Peng, Y. Zhu, M. Xu, Y. Zhang, Y. Fang, X. Yu, D. Yang, and X. Pi, *Zero-Power Optoelectronic Synaptic Devices*, Nano Energy **73**, 104790 (2020).

[7] Z. D. Luo, X. Xia, M. M. Yang, N. R. Wilson, A. Gruverman, and M. Alexe, *Artificial Optoelectronic Synapses Based on Ferroelectric Field-Effect Enabled 2D Transition Metal Dichalcogenide Memristive Transistors*, ACS Nano **14**, 746 (2020).

[8] H. L. Park, H. Kim, D. Lim, H. Zhou, Y. H. Kim, Y. Lee, S. Park, and T. W. Lee, *Retina-Inspired Carbon Nitride-Based Photonic Synapses for Selective Detection of UV Light*, Adv. Mater. **32**, 1906899 (2020).

[9] D. Berco, D. S. Ang, and H. Z. Zhang, *An Optoneuronic Device with Realistic Retinal Expressions for Bioinspired Machine Vision*, Adv. Intell. Syst. **2**, 1900115 (2020).

[10] Y. Wang, J. Yang, W. Ye, D. She, J. Chen, Z. Lv, V. A. L. Roy, H. Li, K. Zhou, Q. Yang, Y. Zhou, and S. T. Han, *Near-Infrared-Irradiation-Mediated Synaptic Behavior from Tunable Charge-Trapping Dynamics*, Adv. Electron. Mater. **6**, 1900765 (2020).

[11] S. Gao, G. Liu, H. Yang, C. Hu, Q. Chen, G. Gong, W. Xue, X. Yi, J. Shang, and R. W. Li, *An Oxide Schottky Junction Artificial Optoelectronic Synapse*, ACS Nano **13**, 2634 (2019).

[12] L. Yin, W. Huang, R. Xiao, W. Peng, Y. Zhu, Y. Zhang, X. Pi, and D. Yang, *Optically Stimulated Synaptic Devices Based on the Hybrid Structure of Silicon Nanomembrane and Perovskite*, Nano Lett. **20**, 3378 (2020).

[13] S. Chen, Z. Lou, D. Chen, and G. Shen, *An Artificial Flexible Visual Memory System Based on an UV-Motivated Memristor*, Adv. Mater. **30**, 1705400 (2018).

[14] L. G. Allan, *The Perception of Time*, Percept. Psychophys. **26**, 340 (1979).

[15] E. A. C. Thomas and W. B. Weaver, *Cognitive Processing and Time Perception*, Percept. Psychophys. **17**, 363 (1975).

[16] S. Shioiri and P. Cavanagh, *Visual Persistence of Figures Defined by Relative Motion*, Vision Res. **32**, 943 (1992).

[17] G. Johansson, *Visual Motion Perception.*, Sci. Am. **232**, 76 (1975).

Chapter VI

Summary and Outlook

In this thesis, simple processes for fabricating next-generation neuromorphic devices were demonstrated. A novel structure resembling the biological neural network was realized based on a simple self-forming process. The self-formed Ag-ASN with branched islands resembled a biological neural network with neurons, synaptic junctions and neurotransmitters. This hierarchical structure facilitated various learning activities such as STP, LTP, potentiation, depression and spike-dependent plasticity behaviors (**Chapter IIIA**). With this interesting device architecture and carefully designed voltage pulse configurations, several higher-order synaptic activities were emulated, importantly, without the aid of external CMOS or of equivalent circuitry. Behaviors close to human psychology such as associative learning, supervision, impression of supervision and interest-based learning were realized. Excitingly, second-order associative learning was emulated for the first time in a neuromorphic device. A prototype kit developed to emulate Pavlov's dog behavior clearly demonstrates the potential of the device towards neuromorphic artificial intelligence (**Chapter IIIB**). In addition, damage induced plasticity such as fatigue and recovery, short-term memory loss was also demonstrated. Interestingly, a common phenomenon called "tip of the tongue experience" is also mimicked in the device (**Chapter IIIC**). A flexible neuromorphic device was fabricated using a simple solution-based method that uses a metal-organic based Palladium hexadecanethiolate precursor. Excellent stability over 1000 bending cycles and a bending radius up to 1 mm was demonstrated (**Chapter IV**). An optoelectronic neuromorphic device was fabricated using a simple solution-based technique. Along with STP, LTP, and SPDP the famous Ebbinghaus forgetting curve, was also emulated (**Chapter VA**). Exploiting the optical response of the device high-performance photodetector was developed by optimizing the fabrication process. This device operates in self-powered mode with a high on/off ratio, fast response, high detectivity and is able to detect very low light intensities in the range of ~ pW in a broad spectral range. Image sensing capability was also accomplished by the pixelated fabrication. The demonstrated prototypes have revealed the potential of the detector for commercial applications (**Chapter VB**). A primitive artificial visual system was demonstrated using the Au-Si photodetector and an

Ag-ASN neuromorphic device. Essential synaptic activities such as STP and LTP were emulated. More interestingly, a primitive visual perception concept was also demonstrated in the system. Excitingly, the synaptic functions were emulated with no external bias voltage (**Chapter VC**).

Having demonstrated on-synapse intelligence in an Ag-ASN device, studies can be extended to synapse density dependent learning activity and structural plasticity which are yet to be explored in the literature. The neuromorphic device with an excellent flexibility and an active synaptic plasticity in the bent state can be further explored to emulate motor neuron functions. An artificial visual system which showed visual synaptic plasticity and visual perception can be investigated towards emulating image, pattern and color recognition abilities. By integrating the various features of the aforementioned devices, a system can be developed towards complete neuromorphic artificial intelligence.

List of Publications

From this thesis

1. **Bannur, B.**; Kulkarni, G. U. On Synapse Intelligence Emulated in a Self-Formed Artificial Synaptic Network. *Mater. Horiz.* **2020,** *7*(11), 2970-2977.
2. **Bannur, B.**; K. N. Harish; Rao, K. D. M.; Kulkarni, G. U. Solution-Based Fast Fabrication of a High-Performance Unlimited Area Au Nanostructure/Si Heterojunction Photodetector. *ACS Appl. Electron. Mater.* **2019**, *1* (4), 577−584.
3. **Bannur, B.**; Yadav, B.; Kulkarni, G. U. Higher-Order Associative Learning Emulated in an Artificial Synaptic Network **2021** (Under preparation).
4. **Bannur, B.**; Kulkarni, G. U. Emulating Short-term Memory Loss in an Artificial Synaptic Network **2021** (Under preparation).
5. **Bannur, B.**; Kulkarni, G. U. A Metal-Organic Based Flexible Neuromorphic Device **2021** (Under preparation).
6. **Bannur, B.**; Kulkarni, G. U. Emulating the Ebbinghaus Forgetting Curve in an Optoelectronic Neuromorphic Device **2021** (Under preparation).

Co-authored publications

7. Mogera, U.; Walia, S.; **Bannur, B.**; Gedda, M.; Kulkarni, G. U. Intrinsic Nature of Graphene Revealed in Temperature-Dependent Transport of Twisted Multilayer Graphene. *J. Phys. Chem. C.* **2017,** *121*, 13938−13943.
8. Sreedhara, M.B.; Gopalakrishnan, K.; **Bannur, B.**; Kumar, R.; Kulkarni, G. U.; Rao, C.N.R. Properties of Nanosheets of 2D-Borocarbonitrides Related to Energy Devices, Transistors and Other Areas. *Chem. Phys. Lett.* **2016**, *657*, 124−130.
9. Sreedhara, M.B.; Ghatak, J.; **Bannur, B.**; Rao, C.N.R. Atomic Layer Deposition of Ultrathin Crystalline Epitaxial Films of V_2O_5. *ACS Appl. Mater. Interfaces.* **2017,** *9*, 3178−3185.

Patents filed

1. Kulkarni, G. U.; **Bannur, B.** A Synaptic Device and Method of Fabrication Thereof. Indian, 27th July **2020**, Provisional Patent Application: 202041032038.
2. Kulkarni, G. U.; **Bannur, B.**; Rao, K.D.M.; Harish, K.N. Semiconductor junction for photo-generated electrons and method thereof. Indian, 23th June **2017**, Patent Application No.: IN201741022128.

Book Chapter

1. Mondal, I.; **Bannur, B.**; Kulkarni, G. U. Advances in the chemistry and physics of materials: Self-forming templates and nanofabrication. *World Scientific,* **2019**.